

Department of Advanced Materials Science  
Graduate School of Frontier Sciences  
The University of Tokyo

2010  
Master's thesis

Growth Control of the Electronic Properties of the  
 $\text{LaAlO}_3/\text{SrTiO}_3$  Heterointerface

$\text{LaAlO}_3/\text{SrTiO}_3$  ヘテロ界面の電子物性の  
作製条件による制御

Submitted on January 25, 2011

Advisor: Professor Harold Y. Hwang

47-096027 Hiroki SATO  
佐藤 弘樹



# Contents

Abbreviations	iv
Symbols	v
Chapter 1 Introduction	1
1.1 Low-dimensional electronic systems	1
1.2 Perovskite oxides and their heterostructures	1
1.2.1 Novel properties of oxide heterostructures	1
1.2.2 Fabrication of high-quality oxide heterostructures	2
1.3 Scope and outline of this Thesis	2
Chapter 2 LaAlO <sub>3</sub> /SrTiO <sub>3</sub> Heterointerface	3
2.1 Introduction	3
2.2 Bulk properties of SrTiO <sub>3</sub> and LaAlO <sub>3</sub>	3
2.2.1 SrTiO <sub>3</sub>	3
2.2.2 LaAlO <sub>3</sub>	5
2.3 The LaAlO <sub>3</sub> /SrTiO <sub>3</sub> heterointerface	5
2.3.1 Conducting interface between the insulating oxides	5
2.3.2 The polar discontinuity picture	6
2.3.3 Other possible origins of the conductivity	7
2.3.4 Potential advantage and problems	7
2.4 Tuning interface properties	8
2.4.1 Oxygen pressure during growth and postannealing treatment	8
2.4.2 Film thickness dependence	9
2.4.3 Electric field control	10
2.5 Summary	11
Chapter 3 Equipment and Techniques	12
3.1 Pulsed laser deposition	12
3.1.1 Thermodynamic conditions	13
3.1.2 Laser spot size and fluence	13
3.1.3 Reflection high-energy electron diffraction	14
3.2 X-ray diffraction	15
3.2.1 $\theta$ - $2\theta$ measurement	16
3.2.2 Reciprocal space mapping	17
3.2.3 Rocking curve measurement	18

3.3	Transport measurements . . . . .	18
3.4	Atomic force microscopy . . . . .	19
Chapter 4	Lattice Constants of LaAlO <sub>3</sub> Thin Films Grown on SrTiO <sub>3</sub> (001)	20
4.1	Introduction . . . . .	20
4.2	Evaluation of film stoichiometry using lattice expansion . . . . .	20
4.2.1	SrTiO <sub>3</sub> homoepitaxial films . . . . .	20
4.2.2	LaAlO <sub>3</sub> homoepitaxial films . . . . .	21
4.2.3	LaAlO <sub>3</sub> films on SrTiO <sub>3</sub> substrates . . . . .	22
4.3	Fabrication of bulk-like single crystal LaAlO <sub>3</sub> thin films on SrTiO <sub>3</sub> (001) using “SrAlO <sub>x</sub> ” buffer layers . . . . .	22
4.3.1	Original motivation to use SrAlO <sub>x</sub> . . . . .	22
4.3.2	Fabrication and analysis of the SrAlO <sub>x</sub> target . . . . .	23
4.3.3	Details of film growth . . . . .	24
4.3.4	Characterization of film crystallinity by XRD and AFM . . . . .	25
4.3.5	Microstructural details by STEM . . . . .	27
4.4	Laser parameter dependence of the lattice expansion of LaAlO <sub>3</sub> films . . . . .	28
4.5	Summary . . . . .	29
Chapter 5	Laser Parameter Dependence of the Interface Properties	30
5.1	Introduction . . . . .	30
5.2	Laser parameter dependence of LaAlO <sub>3</sub> film stoichiometry . . . . .	30
5.2.1	Evaluation methods of LaAlO <sub>3</sub> film stoichiometry . . . . .	30
5.2.2	Details of film growth . . . . .	31
5.2.3	Comparison of XRD and ICP results . . . . .	31
5.2.4	Discussion . . . . .	33
5.3	Laser parameter dependence of the electronic properties . . . . .	33
5.3.1	Laser parameter dependence of the resistance . . . . .	33
5.3.2	Carrier density scaling . . . . .	34
5.3.3	Discussion . . . . .	36
5.4	Possibility of step anisotropy . . . . .	38
5.4.1	Step and terrace structure at the interface . . . . .	38
5.4.2	Details of patterning process . . . . .	39
5.4.3	Angular dependence of the resistance . . . . .	41
5.4.4	Discussion . . . . .	42
5.5	Summary . . . . .	43
Chapter 6	Growth Temperature Dependence of the Interface Properties	44
6.1	Introduction . . . . .	44
6.2	Growth temperature dependence of the film crystallinity . . . . .	44
6.2.1	Details of film growth . . . . .	44
6.2.2	AFM and XRD analysis . . . . .	45
6.2.3	Discussion . . . . .	46
6.3	Growth temperature dependence of the transport properties . . . . .	47

6.3.1	Hall carrier density and mobility . . . . .	47
6.3.2	Analysis of the Shubnikov-de Haas oscillations . . . . .	49
6.3.3	Discussion . . . . .	50
6.4	Summary . . . . .	51
Chapter 7	Conclusions	52
Appendix A	Simulation of XRD $\theta$ - $2\theta$ Patterns	54
Appendix B	Data Treatment for Hall Effect and Magnetoresistance Measurements	57
Appendix C	Control of LaAlO <sub>3</sub> /SrTiO <sub>3</sub> (001) Interfaces Using “SrAlO <sub>x</sub> ”	59
References		61
Acknowledgments		69

# Abbreviations

AFM	atomic force microscopy
FFT	fast Fourier transform
FWHM	full width at half maximum
ICP	inductively coupled plasma
PLD	pulsed laser deposition
PPMS	physical property measurement system
RHEED	reflection high-energy electron diffraction
STEM	scanning transmission electron microscopy
uc	unit cell(s)
XRD	x-ray diffraction

# Symbols

$a$	(pseudo-)cubic lattice constant
$\mathbf{a}, \mathbf{b}, \mathbf{c}$	translation vectors
$A$	area of the laser spot
$B, \mathbf{B}$	magnetic flux density
$c$	out-of-plane lattice constant
$E$	laser energy
$F$	crystal structure factor
$f$	laser fluence
$ G ^2$	Laue function
$H, \mathbf{H}$	magnetic field
$I$	current
$I_e$	prefactor of the intensity of diffracted x-rays
$\mathbf{k}$	wavevector of diffracted x-ray
$\mathbf{k}_0$	wavevector of incident x-ray
$L, M, N$	number of unit cells
$n_s$	sheet carrier density
$T$	temperature
$T_g$	substrate temperature during growth
$T_{\text{sub}}$	substrate temperature
$P_{\text{O}_2}$	oxygen partial pressure
$r$	cation ratio
$\mathbf{r}$	position vector
$R_{\text{H}}$	Hall coefficient
$R_{xx}$	longitudinal resistance
$R_{xy}$	Hall resistance
$V$	voltage
$\lambda$	wavelength of x-ray
$\mu_0$	vacuum permeability
$\mu_{\text{H}}$	Hall mobility
$\phi$	angle between the current and the step edges
$\rho$	electron density
$\rho_s$	sheet resistance
$\omega$	incident angle of x-ray
$2\theta$	diffraction angle of x-ray

# Chapter 1

## Introduction

### 1.1 Low-dimensional electronic systems

Modern technologies are greatly supported by semiconductor-based electronics. Band theory, one of the most important theories in solid state physics, has been successfully applied to conventional semiconductors, leading to the development of the current electronic devices [1, 2]. Semiconductors also provide platforms for studying novel electron physics. Particularly, high-mobility, low-density electrons in reduced dimensions, realized in semiconductor heterostructures, have been attracting great interest [3–6]. One of the most striking examples is the observation of the quantum Hall effect [3, 4], where a macroscopic physical quantity, namely the Hall conductivity, is *exactly* quantized to a precision exceeding one part in  $10^9$ . This discovery has provided a precise method for the determination of the fine structure constant and a standard for electrical resistance.

### 1.2 Perovskite oxides and their heterostructures

#### 1.2.1 Novel properties of oxide heterostructures

Recently, transition metal oxides with the perovskite structure [Fig. 1.1(a)] have been attracting increasing interest, because of the rich variety of physical properties displayed by them, that are absent in conventional semiconductors [7]. Perhaps the most famous example is the discovery of high-temperature superconductivity in the cuprates [8]. Colossal magnetoresistance in the manganites [9] is another, which may enable the design of novel devices magnetically operated.

Notably, perovskite oxides share the same crystal structure with a small difference in lattice constants. This enables the fabrication of epitaxial heterostructures consisting of materials that have different physical properties. Such perovskite oxide heterostructures show novel physical properties that are different from those of the constituent materials, both in thin films [10, 11] and at interfaces [12, 13]. A high-mobility electron gas at the interface between the insulating perovskite oxides  $\text{LaAlO}_3$  and  $\text{SrTiO}_3$  [14] is one of the most representative examples. This example shows a possibility that the layered structure of perovskites [Fig. 1.1(b)] and the ionicity and the multi-valency of transition metal oxides can induce a nontrivial charge rearrangement at oxide heterointerfaces [15].

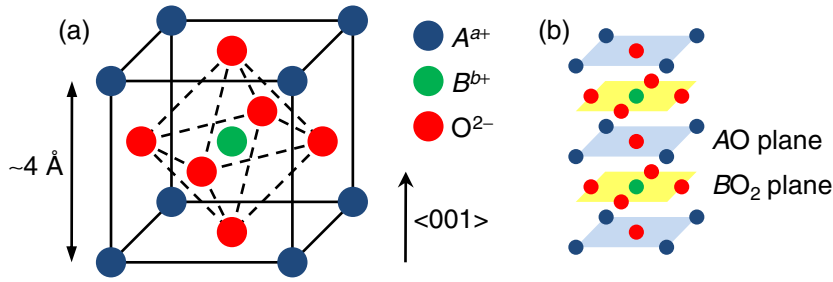


Fig. 1.1 (a) Cubic perovskite structure of  $ABO_3$  and (b) its description as a stacking of alternating layers in the  $\langle 001 \rangle$  direction.

## 1.2.2 Fabrication of high-quality oxide heterostructures

As a natural analogue of conventional semiconductor heterostructures, there has been considerable effort to realize high-mobility, low-density electron systems in reduced dimensions in oxide heterostructures, to explore novel physical properties potentially displayed by them. A central issue in realizing such electron systems is growth optimization to improve the film quality, which directly leads to an enhancement of the mobility.

Indeed, by optimizing the growth conditions with great care [16, 17], high-mobility two-dimensional electron systems have recently been realized in ZnO [18] and also in the perovskite  $SrTiO_3$  [19]. Such electron systems may show unexpected phenomena, which may enable the design of novel devices operated based on conceptually new mechanisms, analogous to the standard for electrical resistance defined using the quantum Hall effect.

## 1.3 Scope and outline of this Thesis

In this Thesis, we investigate the impact of growth parameters on the electronic properties of the  $LaAlO_3/SrTiO_3$  heterointerface, to exploit the possibility of realizing a two-dimensional, high-mobility, low-density electron system at this interface. This system has a potential advantage over the other  $SrTiO_3$ -based heterostructures: namely, the presence of modulation doping, with which the mobility can further be enhanced [20]. Details of this potential advantage, as well as the physical properties of bulk  $SrTiO_3$  and  $LaAlO_3$ , and the  $LaAlO_3/SrTiO_3$  heterointerface are explained in Chap. 2. Chapter 3 describes the fabrication and the characterization techniques for oxide heterostructures used in this study. In Chap. 4, we present the fabrication of single crystal strain-relaxed  $LaAlO_3$  thin films on  $SrTiO_3$  (001) using very thin “ $SrAlO_x$ ” buffer layers. Chapters 5 and 6 describe the effects of the film growth parameters on the properties of the  $LaAlO_3/SrTiO_3$  heterointerface. In Chap. 5, a strong modulation of the film stoichiometry and the carrier density at the interface is presented. In Chap. 6, an enhancement of the mobility and quantum oscillations at the interface are presented. These results enable the control of the electronic properties of this system over a wide range, which may give access to two-dimensional electron physics in an entirely unexplored regime, as summarized in Chap. 7.

# Chapter 2

## LaAlO<sub>3</sub>/SrTiO<sub>3</sub> Heterointerface

### 2.1 Introduction

Since its discovery in 2004, a high mobility electron gas at the interface between the band insulators LaAlO<sub>3</sub> and SrTiO<sub>3</sub> [14] has led to extensive research on this system. Seven years has past from the discovery, and extraordinary properties of this system have been revealed. Two-dimensional superconductivity [21], metal-insulator transition with the film thickness [22] or external electric field [23] are just examples. However, in spite of an enormous amount of effort, the origin of the conductivity and the precise properties of this system are currently unclear.

In this Chapter, a brief review on the bulk properties of SrTiO<sub>3</sub> and LaAlO<sub>3</sub> is first presented, the constituent materials of this heterostructure. Possible origins of the conductivity at the interface are also reviewed, and we point out a potential advantage of this system for realizing a high-mobility, two-dimensional electron system at the interface. Following is a discussion on the control of the electronic properties of this system.

### 2.2 Bulk properties of SrTiO<sub>3</sub> and LaAlO<sub>3</sub>

#### 2.2.1 SrTiO<sub>3</sub>

The perovskite SrTiO<sub>3</sub> is one of the most actively studied oxides. It has a cubic perovskite structure with a cubic lattice constant of  $a = 3.905 \text{ \AA}$  at room temperature, and undergoes a cubic-tetragonal phase transition around 110 K [24, 25]. Stoichiometric SrTiO<sub>3</sub> is a band insulator with a wide bandgap of  $\approx 3.2 \text{ eV}$  [26–28]. The transport properties of SrTiO<sub>3</sub>, however, can easily be modified with a small compositional change. The substitution of La at the Sr site, Nb at the Ti site, or the introduction of oxygen vacancies induces electronic conduction in bulk SrTiO<sub>3</sub>. As shown in Fig. 2.1(a), SrTiO<sub>3</sub> even becomes superconducting at  $\lesssim 300 \text{ mK}$  over a carrier density range of  $\sim 10^{19} - 10^{20} \text{ cm}^{-3}$ , the lowest carrier density known [29–32]. When the carrier density is even lower, the Hall mobility ( $\mu_{\text{H}}$ ) can exceed  $10^4 \text{ cm}^2 \text{ V}^{-1} \text{ s}^{-1}$  at low temperatures [33–35], as shown in Fig. 2.1(b).

Another remarkable property of SrTiO<sub>3</sub> is its large and temperature dependent permittivity [36, 37]. As shown in Fig. 2.1(c), the relative permittivity of SrTiO<sub>3</sub> is  $\approx 300$  at room temper-

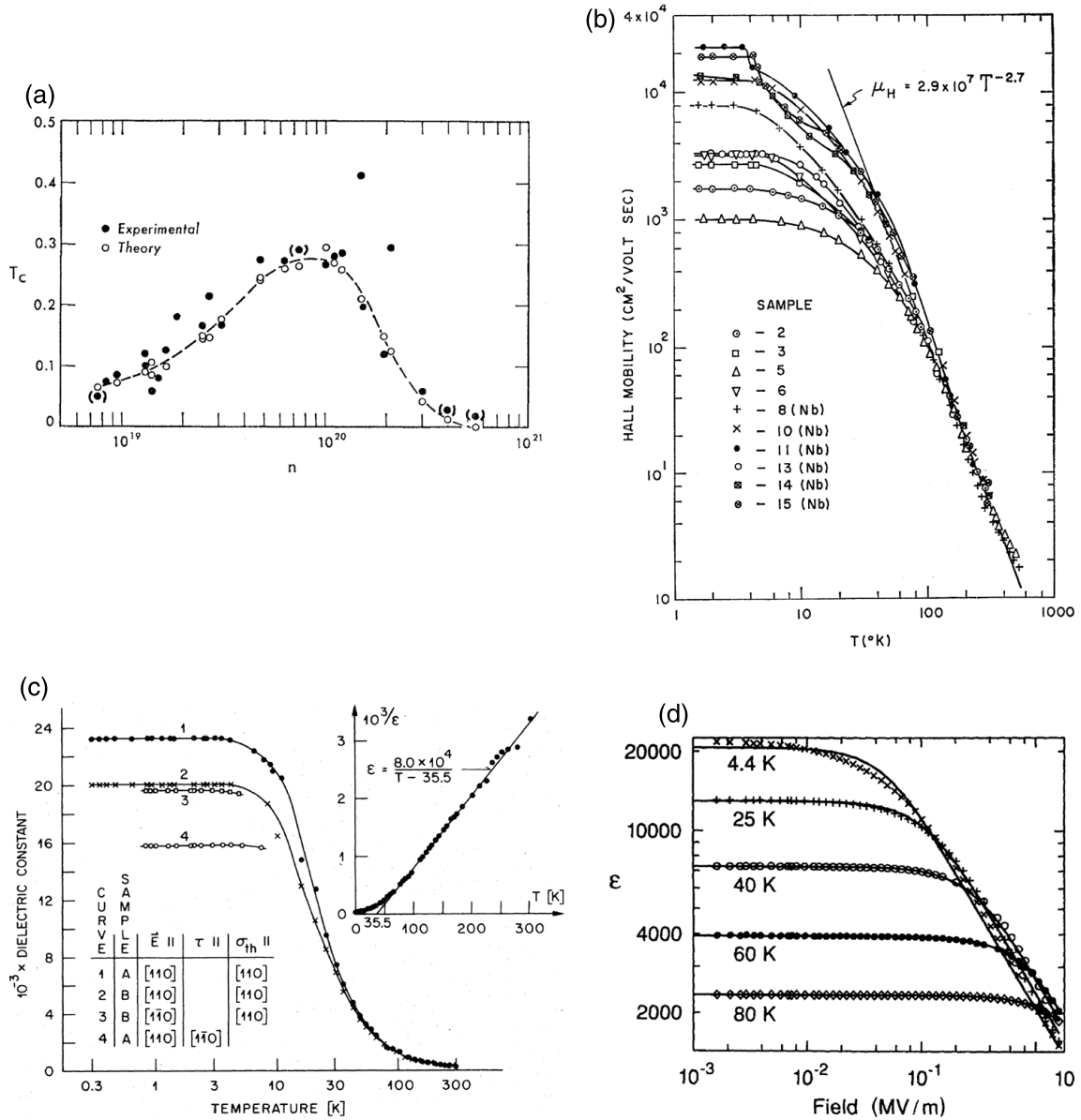


Fig. 2.1 Physical properties of bulk SrTiO $_3$ . (a) Superconducting transition temperature as a function of carrier concentration. From Koonce *et al.* [32]. (b) Temperature dependence of the Hall mobility, doped by Nb or oxygen vacancies with various carrier concentrations. From Tufte and Chapman [34]. (c) Temperature dependence of the relative permittivity. From Müller and Burkard [37]. (d) Electric field dependence of the relative permittivity at various temperatures. From Christen *et al.* [38].

ature and becomes as large as  $\approx 20000$  at low temperatures. This unusually large permittivity at low temperatures has been found to be suppressed by applying large electric fields [38], as shown in Fig. 2.1(d). SrTiO $_3$  is known as a quantum paraelectric material [37], and by chemical substitution [39, 40] or by applying stress [41, 42], a ferroelectric transition can be induced in SrTiO $_3$ .

## 2.2.2 LaAlO<sub>3</sub>

LaAlO<sub>3</sub> is the second building block of the heterostructure studied. LaAlO<sub>3</sub> has a trigonal perovskite structure with a pseudo-cubic lattice constant of  $a = 3.790 \text{ \AA}$  and interior angles of  $\alpha = \beta = \gamma = 90.5^\circ$  at room temperature, and undergoes a cubic-trigonal phase transition at  $\approx 500 \text{ }^\circ\text{C}$  [24, 43, 44]. Thus LaAlO<sub>3</sub> is reasonably well lattice-matched to SrTiO<sub>3</sub>, which enables the fabrication of the LaAlO<sub>3</sub>/SrTiO<sub>3</sub> heterostructure. Because of its distorted unit cell, LaAlO<sub>3</sub> has two different directions of crystal domains, creating a “twin structure” [45]. Throughout this Thesis, all the Miller indices and the lattice constants of LaAlO<sub>3</sub> are based on the pseudo-cubic perovskite unit.

LaAlO<sub>3</sub> is also a band insulator with a wider bandgap of  $\approx 5.6 \text{ eV}$  [46]. Unlike transition metal oxides, the valence state of each cation in LaAlO<sub>3</sub> is fixed as La<sup>3+</sup> and Al<sup>3+</sup>, respectively. Because of the wide bandgap and the fixed valence, electronic conduction can hardly be induced in LaAlO<sub>3</sub>. The relative permittivity of LaAlO<sub>3</sub> is about 25 for temperatures between 300–4 K [47].

## 2.3 The LaAlO<sub>3</sub>/SrTiO<sub>3</sub> heterointerface

### 2.3.1 Conducting interface between the insulating oxides

Ohtomo and Hwang [14] have shown that a high mobility electron gas is formed at the interface between the band insulators LaAlO<sub>3</sub> and SrTiO<sub>3</sub>. They have demonstrated that, when LaAlO<sub>3</sub> is grown directly onto a TiO<sub>2</sub>-terminated SrTiO<sub>3</sub> (001) substrate, the interface shows electronic conduction. The transport properties of the interface are shown in Fig. 2.2.

It is also remarkable that inserting only one monolayer of SrO between the LaAlO<sub>3</sub> film and the SrTiO<sub>3</sub> (001) substrate makes the system insulating [14, 48]. These unexpected results motivated many researchers to investigate the possibility of novel two-dimensional electron physics in this system as well as to search the origin of the conductivity, as briefly reviewed in the following sections.

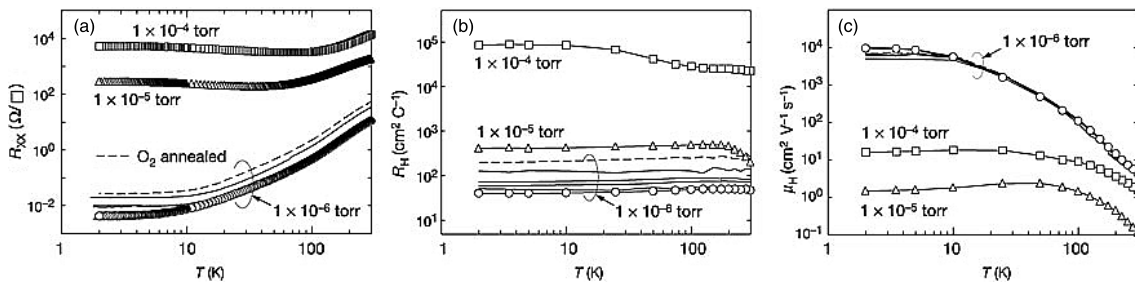


Fig. 2.2 Temperature dependence of (a) the sheet resistance, (b) the Hall coefficient and (c) the Hall mobility of LaAlO<sub>3</sub> (60 Å)/SrTiO<sub>3</sub> (001) heterostructures grown in various oxygen pressures. From Ohtomo and Hwang [14], modified.

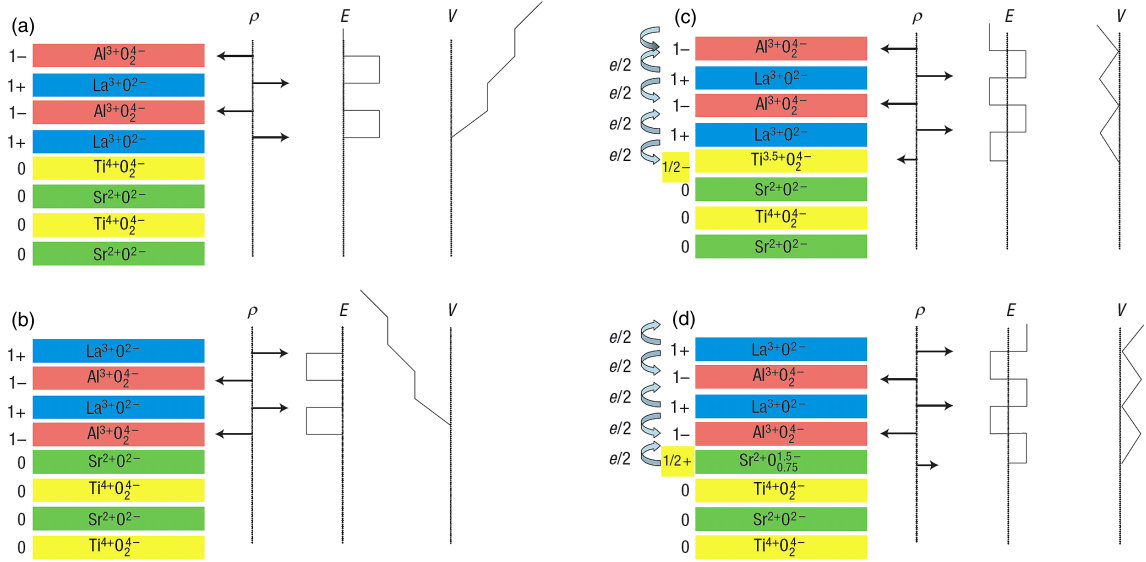


Fig. 2.3 Schematic structure, charge density  $\rho$ , electric field  $E$  and electrostatic potential  $V$  of the  $\text{LaAlO}_3/\text{SrTiO}_3$  heterostructure. (a) The unreconstructed  $\text{AlO}_2/\text{LaO}/\text{TiO}_2$  interface. (b) The unreconstructed  $\text{AlO}_2/\text{SrO}/\text{TiO}_2$  interface. (c) The reconstructed  $\text{AlO}_2/\text{LaO}/\text{TiO}_2$  interface via charge transfer. (d) The reconstructed  $\text{AlO}_2/\text{SrO}/\text{TiO}_2$  interface by the formation of oxygen vacancies. From Nakagawa *et al.* [15].

### 2.3.2 The polar discontinuity picture

To explain the origin of the conductivity and the strong impact of the one monolayer of SrO on it, the *polar discontinuity picture* has been suggested [15]. The perovskite structure  $\text{ABO}_3$  can be described as a stacking of alternating layers of  $\text{AO}$  and  $\text{BO}_2$  in the  $[001]$  direction. If we consider atomically-abrupt  $\text{LaAlO}_3/\text{SrTiO}_3$  (001) interfaces with perfect stoichiometry, they can be distinguished into two different types by the interface termination. One type is  $\text{AlO}_2/\text{LaO}/\text{TiO}_2$ , the other is  $\text{AlO}_2/\text{SrO}/\text{TiO}_2$ . Hereafter these two interfaces are referred to as the  $n$ -type and the  $p$ -type interfaces, respectively, as often used in the literature.<sup>\*1</sup> The  $n$ -type interface can be fabricated by depositing  $\text{LaAlO}_3$  directly on a  $\text{TiO}_2$ -terminated  $\text{SrTiO}_3$  (001) substrate, and the  $p$ -type interface can be fabricated by inserting one monolayer of SrO in between.

In the ionic limit,  $\text{SrTiO}_3$  can be described as a sequence of charge-neutral sheets of  $(\text{SrO})^0$  and  $(\text{TiO}_2)^0$ , whereas  $\text{LaAlO}_3$  can be described as a sequence of  $\pm e$ -charged<sup>\*2</sup> sheets of  $(\text{LaO})^+$  and  $(\text{AlO}_2)^-$ , as schematically shown in Figs. 2.3(a) and (b). Such a stacking of alternating charges creates a diverging electrostatic potential with the  $\text{LaAlO}_3$  film thickness, if there is no charge rearrangement. The interface termination determines the sign of the divergence.

This polar problem must be resolved by some reconstruction, as already discussed for conventional semiconductor heterojunctions [49, 50]. However, the system response to the polar problem can be unconventional at the  $\text{LaAlO}_3/\text{SrTiO}_3$  interface. Another degree of freedom

<sup>\*1</sup> This notation is based on the type of the carriers at these interfaces expected from the polar discontinuity picture.

<sup>\*2</sup> Here  $e$  is the elementary electric charge.

that is absent in conventional semiconductors, namely the multi-valency of transition metal oxides, can play an important role for this.

At the  $n$ -type  $\text{LaAlO}_3/\text{SrTiO}_3$  interface, a possible charge rearrangement to resolve this polar problem is that half an electron per two-dimensional unit cell is introduced to  $\text{SrTiO}_3$ , to make the Ti ion at the interface to be  $\text{Ti}^{3.5+}$ , as shown in Fig. 2.3(c). These extra electrons at the  $n$ -type interfaces can be the origin of the conductivity. Analogous to this, the divergence at the  $p$ -type interface can be avoided if half an hole per two-dimensional unit cell is introduced to  $\text{SrTiO}_3$ . However, since there is no available mixed-valence state to accept the holes, atomic reconstructions are preferred, as in conventional semiconductor heterojunctions [49, 50]. The introduction of oxygen non-stoichiometry was observed experimentally, preventing the divergence but not contributing to the electrical conduction, as shown in Fig. 2.3(d).

### 2.3.3 Other possible origins of the conductivity

While the polar discontinuity picture has been supported by some studies, other studies have revealed many results that cannot easily be explained purely within the polar discontinuity picture. One representative example is the carrier density modulation by the oxygen pressure during growth, as already observed by Ohtomo and Hwang [14]. Especially, the sheet carrier density ( $n_s$ ) at the  $n$ -type interfaces can be as high as  $\sim 10^{17} \text{ cm}^{-2}$  when the  $\text{LaAlO}_3$  film is grown in relatively low oxygen pressures. This value is much larger than half an electron per unit cell ( $n_s \approx 3.28 \times 10^{14} \text{ cm}^{-2}$ ), the expected value from the polar discontinuity picture. These results can be explained more simply by oxygen vacancies introduced into the  $\text{SrTiO}_3$  substrate during growth [51–53].

Several studies have point out that there is a significant interdiffusion at the  $\text{LaAlO}_3/\text{SrTiO}_3$  interface [54–57]. It has also been suggested that the interdiffusion at the  $n$ -type interface is thermodynamically favorable [56, 57]. As explained in Sec. 2.2.1, the substitution of La at the Sr site can induce electronic conduction in  $\text{SrTiO}_3$ , and therefore the interdiffusion can also be the origin of the interfacial conductivity. To date, the origin of the electronic conduction in this system is still under debate.

### 2.3.4 Potential advantage and problems

As mentioned in Chap. 1, a potential advantage of the  $\text{LaAlO}_3/\text{SrTiO}_3$  heterointerface is the presence of modulation doping. Within the polar discontinuity picture one expects that the electrons are electrostatically doped, which may enhance the mobility compared to chemical doping, since there is no scattering by ionized impurities. However, as explained, the doping mechanism at the  $\text{LaAlO}_3/\text{SrTiO}_3$  interface is still controversial, and therefore it is currently unclear whether this potential advantage can be exploited or not.

Since the doping mechanism is not well understood, it is also not clear how to control the carrier density in this system. Control of the carrier density is essential, however, since the electronic properties of  $\text{SrTiO}_3$  are strongly sensitive to such changes [58]. Some control parameters have been found experimentally, as briefly reviewed in the following sections. Problems with those control parameters are also discussed.

## 2.4 Tuning interface properties

### 2.4.1 Oxygen pressure during growth and postannealing treatment

As already seen in the first report [14], the electronic properties of the  $\text{LaAlO}_3/\text{SrTiO}_3$  heterointerface can be modulated by the oxygen pressure during growth. Brinkman *et al.* [59] have investigated this modulation in more detail, by growing  $\text{LaAlO}_3/\text{SrTiO}_3$  samples with a film thickness of 26 unit cells (uc) in various oxygen pressures. Their observation shows that the low temperature conductivity of the as-grown samples can be modulated by several orders of magnitude, as shown in Fig. 2.4(a). Their results indicate a significant contribution of oxygen vacancies to the electronic properties of the as-grown samples. They also found that the sample grown at the highest oxygen pressure shows a remarkable response to the magnetic field at low temperatures, which might originate from magnetism at the interface.

In principle, the oxygen vacancies introduced during growth can be refilled afterwards by annealing the sample in oxidizing conditions. Cancellieri *et al.* [60] have investigated the effect of postannealing treatment on the electronic properties of 5 uc  $\text{LaAlO}_3/\text{SrTiO}_3$  samples grown in various oxygen pressures. They found that the postannealed samples have much less variation in the transport properties, as shown in Figs. 2.4(b-1)–(b-4), compared to the as-grown ones.

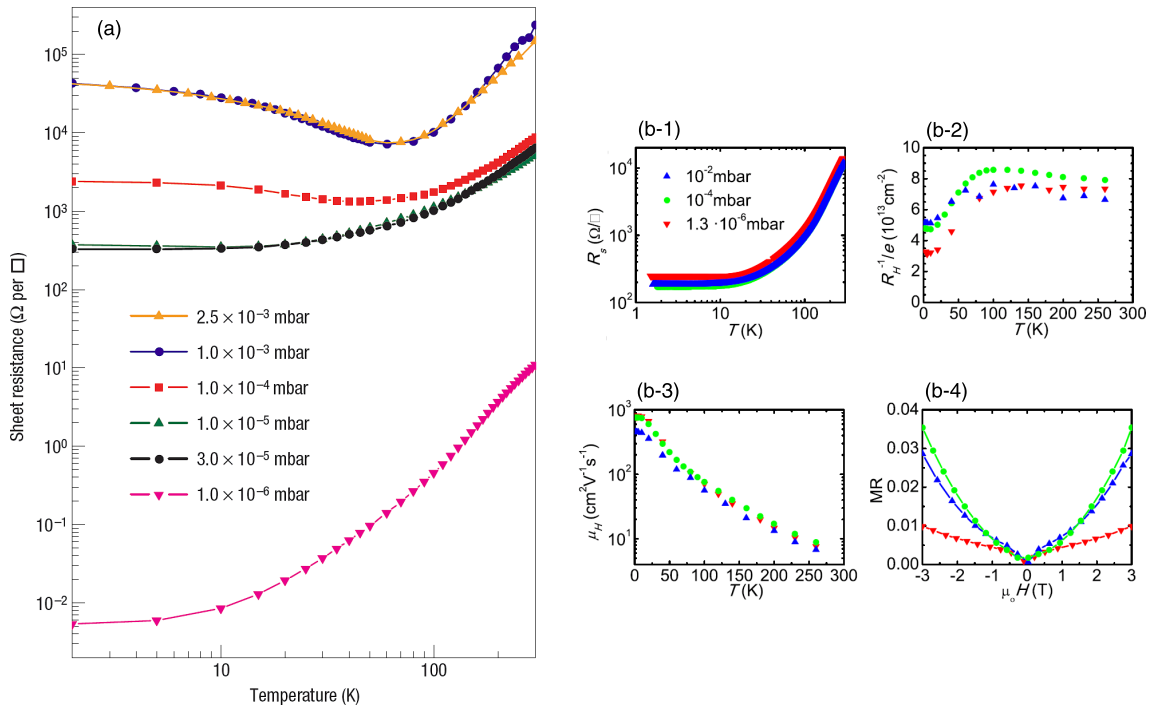


Fig. 2.4 (a) Temperature dependence of the sheet resistance of as-grown 26 uc  $\text{LaAlO}_3/\text{SrTiO}_3$  samples grown in various oxygen pressures. From Brinkman *et al.* [59]. (b) Temperature dependence of (b-1) the sheet resistance, (b-2) the inverse of the Hall coefficient and (b-3) the Hall mobility of postannealed 5 uc  $\text{LaAlO}_3/\text{SrTiO}_3$  samples grown in various oxygen pressures. (b-4) Magnetoresistance at 1.5 K. From Cancellieri *et al.* [60].

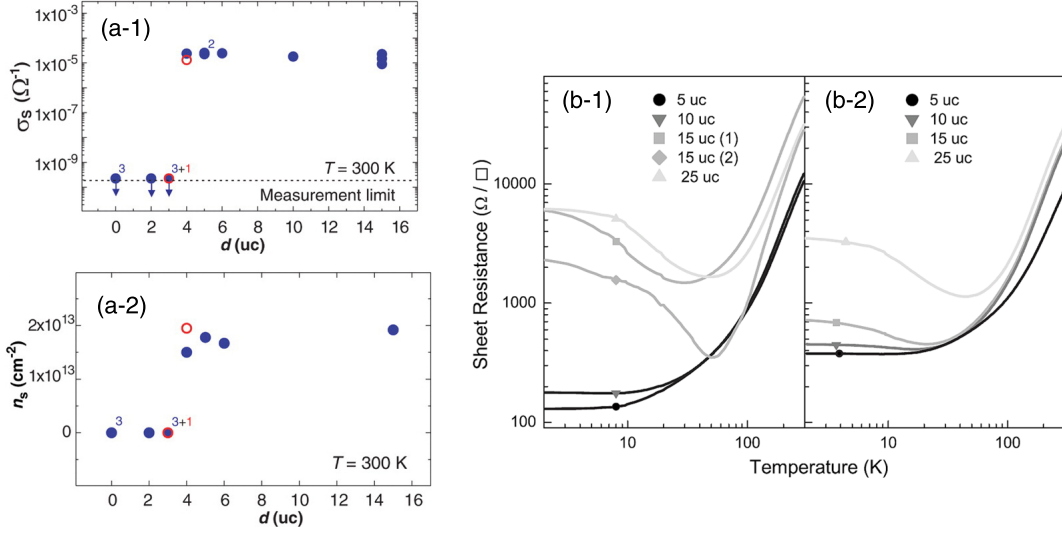


Fig. 2.5 (a) Film thickness dependence of (a-1) the sheet conductance and (a-2) the sheet carrier density of  $\text{LaAlO}_3/\text{SrTiO}_3$  samples grown at  $770^\circ\text{C}$  (blue solid) and  $815^\circ\text{C}$  (red open), respectively. Numbers next to the data points indicate the number of samples with values that are indistinguishable in this plot. From Thiel *et al.* [22]. (b) Temperature dependence of the sheet resistance of  $\text{LaAlO}_3/\text{SrTiO}_3$  samples with various film thicknesses, grown in oxygen pressures of (b-1) 1.33 mPa and (b-2) 13.3 mPa. From Bell *et al.* [66].

Their results indicate that the effect of the growth pressure can be suppressed by postannealing treatment. Similar postannealed samples have been found to become superconducting below  $\approx 200$  mK [21].

The as-grown samples grown in relatively low oxygen pressures, characterized by the distinct low resistivity ( $\sim 10^{-2} \Omega/\text{sq}$  at 2 K) and the high carrier density ( $n_s \gg 10^{14} \text{ cm}^{-2}$ ), have been found to have three-dimensional characteristics [53, 61]. In contrast, the thickness of the electron gas in the postannealed samples is reported to be  $\sim 10$  nm [62–65], and the superconducting properties have been found to be two-dimensional [21, 63].

In this Thesis, the effect of the oxygen pressure during growth is *not* examined. As explained, the effect is more significant in the as-grown samples, but this tuning does not seem to be useful for the motivation of this study, since it induces three-dimensional characteristics (low pressure) or high resistivity at low temperatures (high pressure). The tuning range becomes much smaller when postannealed, and therefore other parameters are explored in this study.

## 2.4.2 Film thickness dependence

The  $\text{LaAlO}_3$  film thickness has also shown to be another crucial control parameter. Thiel *et al.* [22] have demonstrated that the  $\text{LaAlO}_3/\text{SrTiO}_3$  samples are unmeasurably insulating when the  $\text{LaAlO}_3$  thickness is below a critical thickness of 4 uc. At 4 uc the conductivity shows an abrupt change, and the interface becomes conducting above that thickness, as shown in Figs. 2.5(a-1) and (a-2). This result can be interpreted to support the polar discontinuity picture, since the transition can be understood by considering the competition between the electrostatic potential in the  $\text{LaAlO}_3$  film and the energy required for the electronic reconstruction.

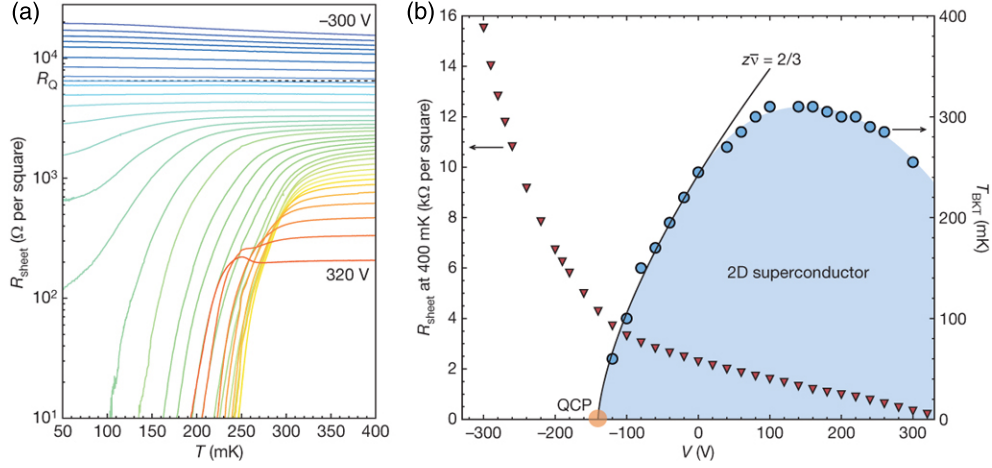


Fig. 2.6 (a) Temperature dependence of the sheet resistance for gate voltages varying in 10-V steps between  $-300$  V and  $-260$  V, 20-V steps between  $-260$  V and  $320$  V, and for  $-190$  V. Dashed line indicates the quantum of resistance. (b) Normal-state sheet resistance measured at  $400$  mK (left axis, red triangles) and the critical temperature  $T_{\text{BKT}}$  (right axis, blue dots) as a function of gate voltage. The solid line describes the approach to the quantum critical point (QCP) using the scaling relation  $T_{\text{BKT}} \propto (V - V_c)^{z\nu}$ , with  $z\nu = 2/3$ . From Caviglia *et al.* [23].

Within this interpretation one expects no thickness dependence above the critical thickness, consistent with the observation by Thiel *et al.* at  $300$  K. By contrast, Bell *et al.* [66] have shown that the interfacial conductivity is strongly thickness dependent far above the critical thickness, especially at low temperatures. As shown in Figs. 2.5(b-1) and (b-2), they observed a progressive change from metallic to almost insulating behavior at low temperatures with increasing the film thickness from  $5$  uc to  $25$  uc.

### 2.4.3 Electric field control

Thiel *et al.* [22] have demonstrated that the conductivity of the  $3$  uc  $\text{LaAlO}_3/\text{SrTiO}_3$  sample, sitting just below the critical thickness, can be modulated by applying a gate voltage to the interface. They observed a memory-like behavior of the interfacial conductivity to the applied back gate voltage. This behavior has also been utilized for “writing and erasing” nanostructures on the  $\text{LaAlO}_3/\text{SrTiO}_3$  sample, by applying a top gate voltage using an conducting atomic force microscope tip [67, 68].

Electric field control has also been utilized for modulating the electronic properties of thicker  $\text{LaAlO}_3/\text{SrTiO}_3$  samples. Caviglia *et al.* [23] have demonstrated the  $\text{LaAlO}_3/\text{SrTiO}_3$  interface ground state control by applying various back gate voltages. As shown in Figs. 2.6(a) and (b), a systematic change from superconducting, metallic to insulating states was observed by varying the gate voltage. Afterwards, it has been suggested that the spin-orbit interaction is also tuned by the electric field [69, 70].

These results clearly demonstrate that the electric field control is a powerful method. However, one disadvantage of this method is the mobility modulation: as pointed out by Bell *et al.* [71], the negative back gate voltage, which decreases the electrons at the interface, causes a

strong reduction of the mobility. Therefore, it may be difficult to realize a high mobility and a low carrier density at the same time by the electric field control, at least using a back gate geometry.

## 2.5 Summary

The physical properties of the  $\text{LaAlO}_3/\text{SrTiO}_3$  heterointerface, as well as those of the bulk  $\text{SrTiO}_3$  and  $\text{LaAlO}_3$  were briefly reviewed. We also pointed out a potential advantage of this system and problems to realize a high-mobility, low-density electron system at this interface.

As mentioned in Chap. 1, growth optimization is crucial to for realizing such a system. In Chaps. 5 and 6, we investigate how to realize a high mobility and a low carrier density at the same time in this system, mainly focusing on another growth parameters that are often not discussed in the literature.

## Chapter 3

# Equipment and Techniques

### 3.1 Pulsed laser deposition

In this study, samples were fabricated using the pulsed laser deposition (PLD) method. PLD is a versatile method with which a wide variety of nanostructures have been fabricated, including oxide thin films with atomic-length scale precision [72, 73]. A schematic illustration of our PLD system is shown in Fig. 3.1. The main components of the system are the vacuum chamber, the sample holder, the target holders, the KrF excimer laser, and the reflection high-energy electron diffraction (RHEED) monitoring system.

The principle of PLD is as follows (also schematically shown in Fig. 3.1). Intense laser pulses are introduced into the growth chamber and focused onto the surface of the target. Absorbing the energy from the laser pulses, the ablated target material is transformed into a plasma (also known as the “plume”), and the material from the plume is then allowed to recondense on the surface of the substrate, forming thin films.

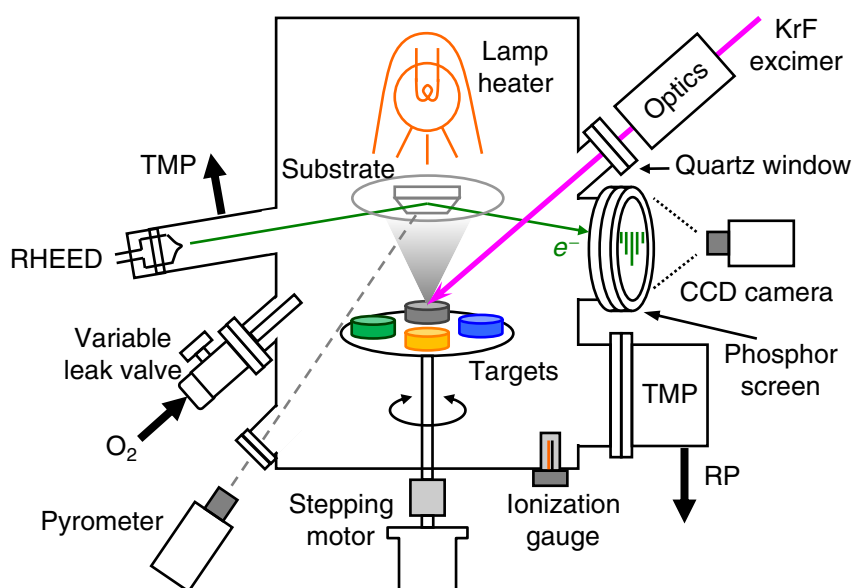


Fig. 3.1 Schematic illustration of the PLD system. TMP: turbo molecular pump, RP: rotary pump, respectively. (Courtesy of Y. Hotta, modified.)

As partly reviewed in Sec. 2.4, there are many growth parameters that are highly influential over the sample properties. In the following sections, the importance of those parameters and their control methods are briefly explained.

### 3.1.1 Thermodynamic conditions

One possible origin of the conductivity at the  $\text{LaAlO}_3/\text{SrTiO}_3$  interface is the oxygen vacancy doping, and consequently the oxygen partial pressure ( $P_{\text{O}_2}$ ) during growth is of great importance, since the oxygen stoichiometry of the sample can strongly be modulated. The oxygen partial pressure was tuned by introducing high purity oxygen gas (G1 grade, 99.9995% purity) into the chamber through a variable leak valve, varied over the range  $10^{-6}$ – $10^{-4}$  Torr. In order to improve the precision of the control and suppress the effects of other gases which might contaminate the sample, the background pressure in the chamber was kept as low as  $\sim 10^{-8}$  Torr, achieved by the combination of the turbo molecular pump and the rotary pump. The pressure was measured by an ionization gauge in the chamber.

To fill the possible oxygen vacancies introduced during growth, the samples were often postannealed *in situ* in a relatively high oxygen partial pressure (300 Torr). Since the turbo molecular pump and the ionization gauge could not work in high pressures, they were turned off and the chamber was sealed during the postannealing. The pressure was monitored using another high pressure gauge.

Another important parameter is the substrate temperature ( $T_{\text{sub}}$ ), which can modulate the thermodynamics and the kinetic processes of growth. To control the substrate temperature, the Inconel sample holders, on which the substrates were glued with Pt paste and Inconel clamps, were heated by a lamp heater from the backside. The highest temperature available in our system was  $\approx 1000$  °C. The temperature of the attached substrates was monitored by an external infrared pyrometer (CHINO IR-AP), assuming the emissivity of the  $\text{SrTiO}_3$  substrates was 0.8 (as used by Ohtomo and Hwang [14]). The low measurement limit of the pyrometer was 390 °C.

### 3.1.2 Laser spot size and fluence

Effects of laser parameters on the sample properties are the main issue in Chap. 5, in which the importance of them are explained in detail. The control of the laser spot size and fluence were achieved using the optical system described below. The pulsed KrF excimer laser (wavelength = 248 nm, pulse duration time  $\sim 25$  ns) was introduced into the chamber through a variable attenuator, an aperture, the “zoom stage,” and the laser entrance window, as schematically shown in Fig. 3.2.

The laser energy ( $E$ ) was controlled by rotating the variable attenuator, instead of changing the voltage of the laser source (fixed at 26 kV), in order to avoid changing the divergence of the beam [74]. The aperture ( $5 \times 15 \text{ mm}^2$ ) cut the fringes of the Gaussian beam and defined the shape of the pulsed laser. The zoom stage consisted of four lenses (focal lengths  $f_1 = 360$  mm,  $f_2 = -26$  mm,  $f_3 = 206$  mm, and  $f_4 = 360$  mm), which were aligned to image the laser on the target. This four-lens imaging was far less sensitive to the divergence characteristics of the laser than just using a single lens. The area of the imaged laser spot ( $A$ ) was controlled by moving the

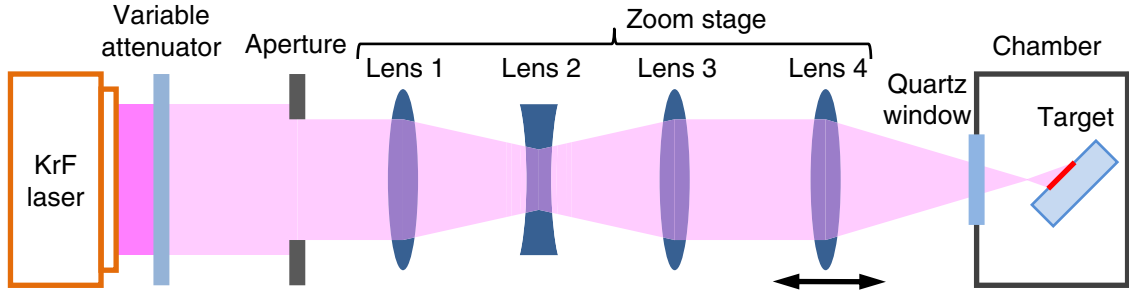


Fig. 3.2 Schematic illustration of the optical path of the excimer laser. Several additional mirrors used to guide the beam are not shown for clarity.

final lens position. The spot size was measured by “ablating” a thermosensitive paper placed at the position of the target surface. The laser energy was measured using a power meter just before the quartz window (*outside* the chamber), and the fluence ( $f = E/A$ ) was calculated. The transparency of the window was taken into the calculation, since the contamination of the window due to the deposited material significantly lowered the laser intensity [74]. The transparency was measured just before conducting experiments.

### 3.1.3 Reflection high-energy electron diffraction

The  $\text{LaAlO}_3$  thickness has been found to be a crucial parameter for the  $\text{LaAlO}_3/\text{SrTiO}_3$  interface properties [22, 66], and therefore the precise control of the film thickness is vital for investigating this system in detail. For this purpose, we employed RHEED, which enables us to monitor the growth process *in situ* [75]. Using this RHEED system, the samples were irradiated by electrons which were emitted from a 25 keV electron gun and focused by electromagnetic lenses. The diffraction patterns of the electrons at the phosphor screen were measured with a high sensitivity CCD camera (see Fig. 3.1).

Due to the very small incident angle of the electrons ( $\sim 1^\circ$ ) as well as the strong scattering potential for electrons in solids, almost all of the electrons are diffracted by the topmost atoms at the surface of the sample. Therefore, the diffracted pattern is very surface-sensitive, reflecting the crystal structure and the morphology of the surface [76]. During deposition, the intensity of the RHEED patterns shows oscillatory behavior. This can be understood by considering the change of the surface roughness during layer-by-layer growth of the film, as schematically shown in Fig. 3.3. Accordingly, RHEED oscillations can be used as a thickness monitor in this growth mode, since ideally each oscillation peak corresponds to the deposition of each monolayer.

In reality, there are many growth modes other than the layer-by-layer one, and the corresponding RHEED oscillations are more complicated [76]. Moreover, it has been pointed out that RHEED oscillations show phase shifts and frequency doubling, depending on the incident angle of the electron beam [77]. Due to these effects, the precise calibration of the film thickness cannot always be achieved only by RHEED. Nevertheless, RHEED still contains much information about the growth mode, and once the relationship between the thickness of the film and each oscillation is confirmed using other methods, such as x-ray diffraction (see the next

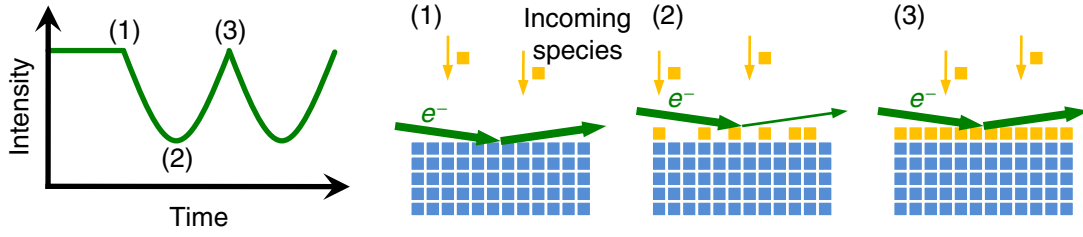


Fig. 3.3 Schematic illustration of the RHEED oscillations during layer-by-layer growth (left) and the corresponding surface structures (right).

Section), transmission electron microscopy, etc., it can be used to determine the film thickness *in situ*.

As seen in Sec. 4.3.4, it was confirmed that each RHEED oscillation during  $\text{LaAlO}_3$  growth corresponded to the deposition of each unit cell, using x-ray diffraction and a relatively thick  $\text{LaAlO}_3$  film. Based on this, the thickness of very thin films, which could not be precisely calibrated by x-ray diffraction, was determined only by RHEED.

## 3.2 X-ray diffraction

X-ray diffraction (XRD) is a very widely used method for characterizing crystal structures. In this study, we employed a high resolution XRD system (D8 Discover: Brucker AXS Inc.), where the samples were irradiated by the  $\text{Cu } K\alpha_1$  line (wavelength  $\lambda = 1.54056 \text{ \AA}$ ) which was screened by a  $\text{Ge } (220)$  monochromator. Crystal structures were characterized by three different measurement geometries, as described in the following sections. Before that, let us review the basics of XRD in more detail [78].

Mathematically, the intensity profile of diffracted x-rays is related to the Fourier transform of the electron density:

$$I(\mathbf{k}) = I_e \left| \int_{\text{matter}} \rho(\mathbf{r}) e^{i(\mathbf{k}-\mathbf{k}_0)\cdot\mathbf{r}} d^3\mathbf{r} \right|^2 \equiv I_e |A(\Delta\mathbf{k})|^2, \quad (3.1)$$

where  $I(\mathbf{k})$  is the intensity of the diffracted x-ray with wavevector  $\mathbf{k}$ ,  $I_e$  is a prefactor,  $\rho(\mathbf{r})$  is the electron density of the matter at position  $\mathbf{r}$ ,  $\mathbf{k}_0$  is the wavevector of the incident x-ray, and  $\Delta\mathbf{k} = \mathbf{k} - \mathbf{k}_0$ . For crystals, where the atoms are periodically arranged and correspondingly  $\rho(\mathbf{r})$  has a periodicity,  $A(\Delta\mathbf{k})$  can be described as

$$\begin{aligned} A(\Delta\mathbf{k}) &= \sum_{l,m,n} e^{i\Delta\mathbf{k}\cdot(l\mathbf{a}+m\mathbf{b}+n\mathbf{c})} \int_{\text{unit cell}} \rho(\mathbf{r}') e^{i\Delta\mathbf{k}\cdot\mathbf{r}'} d^3\mathbf{r}' \\ &= G(\mathbf{k})F(\mathbf{k}), \end{aligned} \quad (3.2)$$

where  $\mathbf{a}$ ,  $\mathbf{b}$  and  $\mathbf{c}$  are the translation vectors of the crystal,

$$F(\mathbf{k}) \equiv \int_{\text{unit cell}} \rho(\mathbf{r}') e^{i\Delta\mathbf{k}\cdot\mathbf{r}'} d^3\mathbf{r}' \quad (3.3)$$

is the crystal structure factor, and

$$G(\mathbf{k}) \equiv \sum_{l,m,n} e^{i\Delta\mathbf{k}\cdot(l\mathbf{a}+m\mathbf{b}+n\mathbf{c})}. \quad (3.4)$$

Let  $L$ ,  $M$  and  $N$  be the number of unit cells along the  $\mathbf{a}$ ,  $\mathbf{b}$  and  $\mathbf{c}$  directions, respectively. Then  $G(\mathbf{k})$  can be described as

$$\begin{aligned} G(\mathbf{k}) &= \sum_{l=0}^L e^{il\Delta\mathbf{k}\cdot\mathbf{a}} \sum_{m=0}^M e^{im\Delta\mathbf{k}\cdot\mathbf{b}} \sum_{n=0}^N e^{in\Delta\mathbf{k}\cdot\mathbf{c}} \\ &= \frac{1 - e^{iL\Delta\mathbf{k}\cdot\mathbf{a}}}{1 - e^{i\Delta\mathbf{k}\cdot\mathbf{a}}} \frac{1 - e^{iM\Delta\mathbf{k}\cdot\mathbf{b}}}{1 - e^{i\Delta\mathbf{k}\cdot\mathbf{b}}} \frac{1 - e^{iN\Delta\mathbf{k}\cdot\mathbf{c}}}{1 - e^{i\Delta\mathbf{k}\cdot\mathbf{c}}}, \end{aligned} \quad (3.5)$$

$$|G(\mathbf{k})|^2 = \frac{\sin^2(L\Delta\mathbf{k}\cdot\mathbf{a}/2)}{\sin^2(\Delta\mathbf{k}\cdot\mathbf{a}/2)} \cdot \frac{\sin^2(M\Delta\mathbf{k}\cdot\mathbf{b}/2)}{\sin^2(\Delta\mathbf{k}\cdot\mathbf{b}/2)} \cdot \frac{\sin^2(N\Delta\mathbf{k}\cdot\mathbf{c}/2)}{\sin^2(\Delta\mathbf{k}\cdot\mathbf{c}/2)}. \quad (3.6)$$

$|G(\mathbf{k})|^2$  is called Laue function. It can be proven that

$$\lim_{L,M,N \rightarrow \infty} |G(\mathbf{k})|^2 = \delta^3(\Delta\mathbf{k} - \mathbf{Q}), \quad (3.7)$$

where  $\mathbf{Q}$  is the reciprocal lattice of the crystal. Therefore, if the crystal is much larger than the penetration depth of the x-ray, the XRD intensity  $I(\mathbf{k}) = I_e |F(\mathbf{k})|^2 |G(\mathbf{k})|^2$  has finite values only when  $\Delta\mathbf{k} = \mathbf{k} - \mathbf{k}_0$  is equal to the reciprocal lattice.\*<sup>1</sup>

### 3.2.1 $\theta$ - $2\theta$ measurement

Figure 3.4(a) shows the geometry of a XRD  $\theta$ - $2\theta$  measurement. The diffraction profile was measured using a zero-dimensional detector (scintillation counter with a variable slit), which was rotated around the sample while maintaining the relationship  $\omega = \theta$  ( $\omega$ : incident angle of the x-ray to the sample surface,\*<sup>2</sup>  $2\theta$ : diffraction angle of the x-ray). As seen in the figure,  $\Delta\mathbf{k}$  is always along the normal of the sample surface, and correspondingly the Laue function is written as

$$|G|^2 = \frac{\sin^2 [(\pi/\lambda) \cdot 2Nc \sin \theta]}{\sin^2 [(\pi/\lambda) \cdot 2c \sin \theta]}, \quad (3.8)$$

where  $c$  is the out-of-plane lattice constant of the sample.  $|G|^2$  has maximum values when Bragg's condition is satisfied:

$$2c \sin \theta = n\lambda \quad (n: \text{integer}). \quad (3.9)$$

If the film (thickness  $\sim 10$  nm) is deposited on the substrate (thickness  $\sim 0.5$  mm) maintaining the crystalline orientation, we can observe peaks other than those from the substrate,

\*<sup>1</sup> In general,  $|F|^2$  may become zero at certain reciprocal points and the corresponding reflections are "extinguished" (known as the "extinction rule"). For the perovskites investigated, however, this does not occur.

\*<sup>2</sup> *Crystallographic* surface, which was determined using the substrate reflection in the scan area. The *macroscopic* surface is not perfectly parallel to the crystallographic plane due to the inevitable miscut.

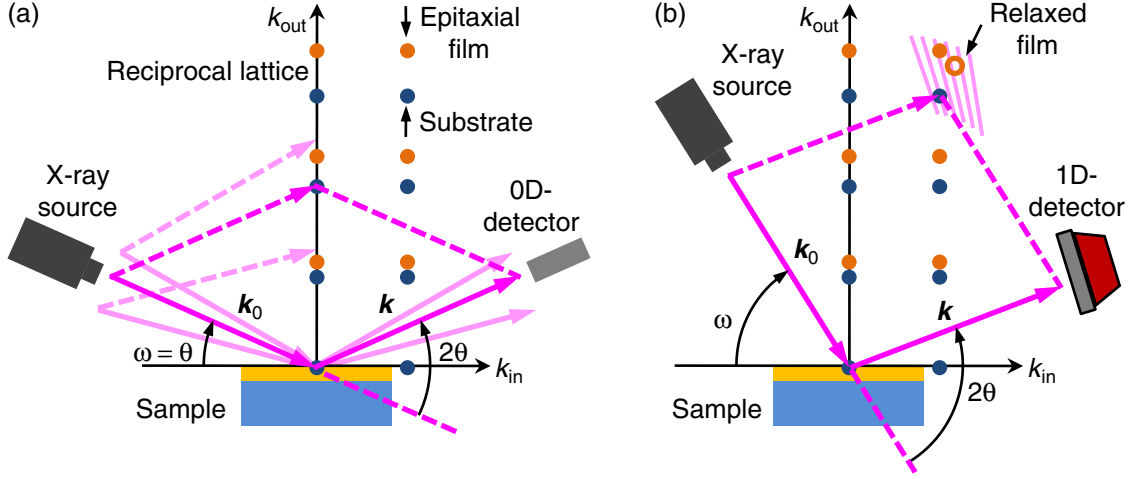


Fig. 3.4 Schematic illustration of the geometry of XRD for (a)  $\theta$ - $2\theta$  measurement and (b) reciprocal space mapping.

because of the difference in the out-of-plane lattice constants between the film and the substrate. Therefore, the  $\theta$ - $2\theta$  measurement can tell us that single-crystalline oriented growth of the films has occurred, as well as the out-of-plane lattice constant of the films.

Moreover, the film peaks have an intrinsic broadening and satellite peaks (Laue fringes) because of the finite thickness ( $N \leq 100$  in this study), which can be used for the thickness estimation. The zero points of  $|G|^2$  are given by

$$2t \sin \theta = m\lambda \quad (m: \text{integer}). \quad (3.10)$$

Here  $t = Nc$  is the film thickness, which therefore can be determined by

$$t = \frac{\lambda}{2(\sin \theta_m - \sin \theta_{m-1})}, \quad (3.11)$$

where  $\theta_m$  and  $\theta_{m-1}$  are the position of the  $m^{\text{th}}$  and  $(m-1)^{\text{th}}$  zero points, respectively. We can also use the local maxima positions instead of the zero points. Also, by approximating the Laue function by a Gaussian function, we can deduce Scherrer's formula:

$$\text{FWHM}(2\theta) = \frac{2[(\ln 2)/\pi]^{1/2}\lambda}{t \cos \theta} = \frac{0.94\lambda}{t \cos \theta}, \quad (3.12)$$

where FWHM denotes the full width at half maximum of the peak.

Actually, the discussions above are not exact, since the diffraction spots from the film and the substrate are not completely independent. The effects of the interference between the film and the substrate are discussed in App. A.

### 3.2.2 Reciprocal space mapping

While  $\theta$ - $2\theta$  measurement scans only the on-axis peaks, off-axis peaks are also important to characterize the crystal structures, especially the strain state of the film. For off-axis measurement we employed a one-dimensional detector (VANTEC), which can simultaneously detect

the diffracted x-ray over a range of  $2\theta$  of  $\approx 10^\circ$  with a resolution better than  $0.01^\circ$ . The reciprocal space was mapped using the detector by stepping  $\omega$  with  $2\theta$  range fixed, as schematically shown in Fig. 3.4(b). The reciprocal space coordinates  $k_{\text{in}}$  and  $k_{\text{out}}$  are calculated by

$$k_{\text{in}} = \frac{2\pi}{\lambda} [\cos(2\theta - \omega) - \cos(\omega)], \quad (3.13)$$

$$k_{\text{out}} = \frac{2\pi}{\lambda} [\sin(2\theta - \omega) + \sin(\omega)]. \quad (3.14)$$

### 3.2.3 Rocking curve measurement

If the crystal structure of the sample is not perfect, the XRD peaks are broadened, which can therefore be used as a parameter of the crystalline quality. However, as explained in Sec. 3.2.1, the peaks from thin films have an intrinsic broadening along the out-of-plane direction. Therefore, the broadening along the in-plane direction is more useful for the evaluation of the film crystallinity. For on-axis peaks, the diffraction profile along the in-plane direction can be measured by rocking  $\omega$  with  $2\theta$  locked. This profile is called the rocking curve.<sup>\*3</sup> In this study, rocking curves were measured using the same arrangement as for the  $\theta$ - $2\theta$  measurement. The film peak position was determined by the  $\theta$ - $2\theta$  measurement.

## 3.3 Transport measurements

In this study, transport measurements were carried out in a Physical Property Measurement System (PPMS; Quantum Design Inc.), where the range of temperature ( $T$ ) from 2 K to 400 K and the range of magnetic field ( $\mu_0 H$ ;  $\mu_0$  is the vacuum permeability) from 0 T to  $\pm 14$  T were available. The precision of the temperature was better than 0.5%, that of the magnetic field better than  $\pm 10^{-3}$  T.

The longitudinal and the Hall resistances ( $R_{xx}$  and  $R_{xy}$ ) were measured with a standard Hall bar geometry using the four-probe method, which is widely used to exclude the contact resistance, as schematically shown in Fig. 3.5. The resistance bridge of the PPMS was employed for these measurements, where the current direction was switched with a repetition rate of 7.5 Hz to exclude the effect of the possible DC offsets of voltage. Unless otherwise indicated,

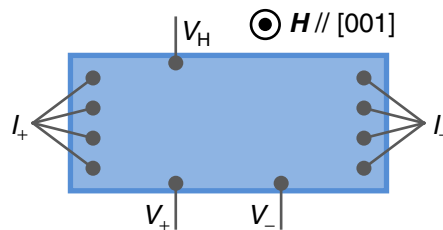


Fig. 3.5 Schematic illustration of the normal geometry of transport measurements.

<sup>\*3</sup> In general, rocking curve measurement is not only for the on-axis peaks. For off-axis peaks, however, the scan direction is not along the in-plane direction.

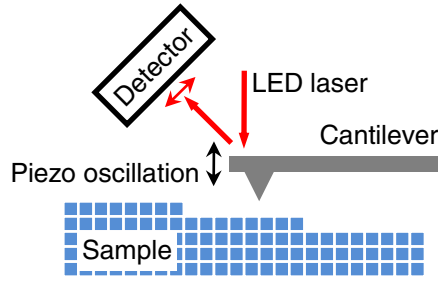


Fig. 3.6 Schematic illustration of AFM.

the electrodes were created by bonding Al wire with an ultrasonic wirebonder (Model 7476D: West Bond Inc.). To confirm Ohmic contacts, two-point current–voltage characteristics were also measured using a semiconductor parameter analyzer (Agilent 4155C).

Since the samples were not patterned, there was a practical problem with deriving  $R_{xx}$  and  $R_{xy}$ . Details of the problem and the data treatment to solve it are explained in App. B.

### 3.4 Atomic force microscopy

Atomic force microscopy (AFM) is a powerful method to investigate the surfaces of various materials [79]. In this study, topographical images of the surfaces of the samples were taken with an AFM (Veeco, Digital Instruments Dimension™) *ex situ*, at room temperature in air, using the “tapping-mode.”

As shown in Fig. 3.6, the probe of the AFM is a cantilever with a resonance frequency of  $\sim 300$  kHz. It is oscillated vertically by a piezoelectric device at a frequency  $\approx 5\%$  away from the resonance frequency. A sharp (length  $\lesssim 5$   $\mu\text{m}$ , end curvature  $\lesssim 10$  nm) tip located at the end of the cantilever moves over the surface of the sample. When the tip is close to the sample, the oscillation of the cantilever is modified by the change of the atomic force between the tip and the sample, which can be detected using a laser reflected from the top of the cantilever. Thus this modification can be converted into a height, resulting a topographical image of the surface of the sample with the two-dimensional rastering of the cantilever.

## Chapter 4

# Lattice Constants of LaAlO<sub>3</sub> Thin Films Grown on SrTiO<sub>3</sub> (001)

### 4.1 Introduction

The measurement of the lattice constants of thin films is a very fundamental method to characterize them. For example, lattice constants of heteroepitaxial thin films are different from those in bulk, due to the strain resulting from the inevitable lattice mismatch between the film and the substrate. The residual strain in the films can have a significant effect on the film properties [80]. Moreover, it has been pointed out that film lattice constants can be used as a parameter to measure the net cation off-stoichiometry in the film, as reviewed in Sec. 4.2.

In this Chapter, we present the fabrication of single crystal strain-relaxed LaAlO<sub>3</sub> thin films on SrTiO<sub>3</sub> (001) using very thin “SrAlO<sub>x</sub>” buffer layers, which enables the evaluation of the LaAlO<sub>3</sub> film stoichiometry using the lattice expansion. A series of LaAlO<sub>3</sub>/SrAlO<sub>x</sub>/SrTiO<sub>3</sub> heterostructures were grown with increasing interlayer thickness. At a critical thickness of 3 uc of SrAlO<sub>x</sub>, the interlayer acts as a sliding buffer layer, and abruptly relieves the lattice mismatch between the LaAlO<sub>3</sub> film and the SrTiO<sub>3</sub> substrate, while maintaining a well-defined crystalline orientation, as explained in Sec. 4.3. We have utilized this method to the evaluation of LaAlO<sub>3</sub> film lattice constants grown in various conditions, as explained in Sec. 4.4.

### 4.2 Evaluation of film stoichiometry using lattice expansion

#### 4.2.1 SrTiO<sub>3</sub> homoepitaxial films

It has been reported by Ohnishi *et al.* that the cation stoichiometry of complex oxide films grown by PLD is strongly affected by the laser parameters [81, 82]. They grew SrTiO<sub>3</sub> homoepitaxial films in various laser conditions controlling the spot size and the fluence, with other growth parameters fixed. Their observation shows that the lattice constant of the homoepitaxial films can be tuned widely by changing the laser conditions, as shown in Fig. 4.1.

They argue that *cation* non-stoichiometry in the film expands the lattice, by the formation of Ruddlesden-Popper defects [83] or Coulomb repulsion near the cation vacancies. They, as well as another previous report [84], have pointed out that highly-reduced SrTiO<sub>3</sub> bulk single

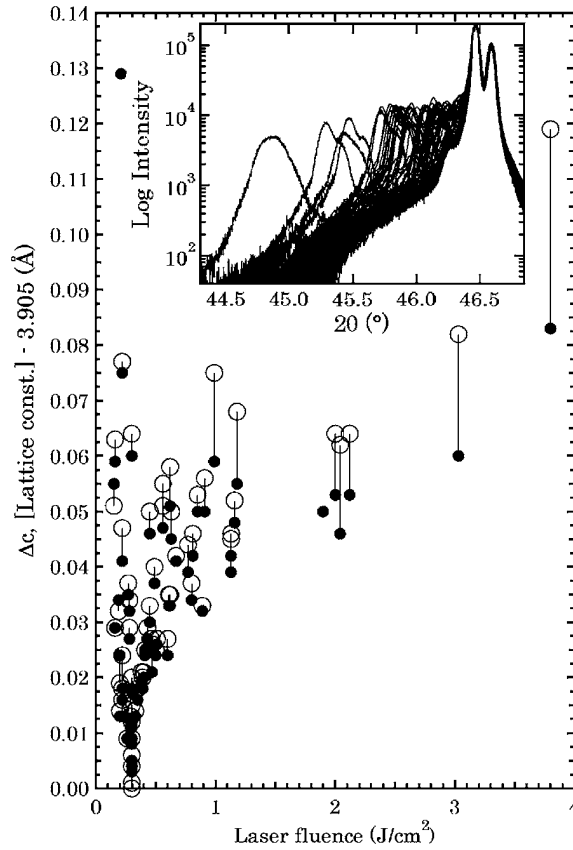


Fig. 4.1 Expansion of the lattice constant of SrTiO<sub>3</sub> homoepitaxial films as a function of laser fluence. Filled and open circles correspond to the as-grown and air-annealed films, respectively. The top inset shows XRD  $\theta$ - $2\theta$  patterns recorded after deposition. From Ohnishi *et al.* [81], modified.

crystals show no detectable change of the lattice constant, indicating that the oxygen vacancies (*anion non-stoichiometry*) are not the cause of the lattice expansion.

Cation non-stoichiometry of complex oxide films can strongly modulate the film properties. For example, in the case of Nb-doped SrTiO<sub>3</sub> [82], the cation vacancies can trap and scatter the electrons, resulting in high resistivity in the films.

#### 4.2.2 LaAlO<sub>3</sub> homoepitaxial films

Analogous to the SrTiO<sub>3</sub> homoepitaxial growth study [81, 82], LaAlO<sub>3</sub> film stoichiometry might be evaluated using the lattice expansion of LaAlO<sub>3</sub> homoepitaxial films. It is not easy, however, to correctly measure the lattice constant of LaAlO<sub>3</sub> homoepitaxial films: since LaAlO<sub>3</sub> has a twin structure [45], caused by the cubic-trigonal transition at  $\approx 500$  °C, the substrate reference of the XRD pattern is often not clear, as shown in Fig. 4.2. To utilize the lattice expansion, it is to be desired that the LaAlO<sub>3</sub> film is grown on a substrate whose XRD peaks are sufficiently clear to be used as a reference. A candidate is SrTiO<sub>3</sub>, as also shown in Fig. 4.2.

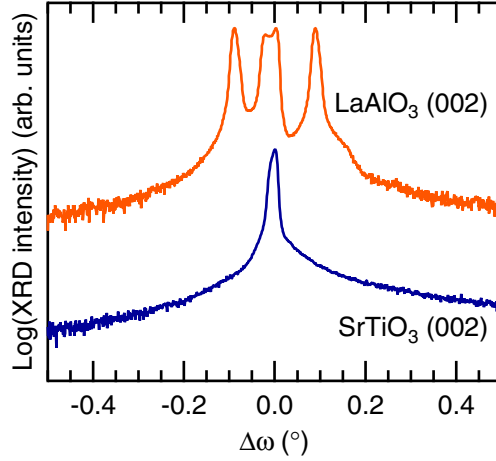


Fig. 4.2 Typical XRD rocking curves of as-received  $\text{LaAlO}_3$  (001) and  $\text{SrTiO}_3$  (001) substrates.

### 4.2.3 $\text{LaAlO}_3$ films on $\text{SrTiO}_3$ substrates

One problem for evaluating the lattice expansion of  $\text{LaAlO}_3$  films on  $\text{SrTiO}_3$  substrates is the epitaxial strain. Since there is a significant lattice mismatch of  $\approx 3\%$  between  $\text{LaAlO}_3$  ( $a = 0.379$  nm) and  $\text{SrTiO}_3$  ( $a = 0.3905$  nm), the epitaxial  $\text{LaAlO}_3$  film on  $\text{SrTiO}_3$  (001) is subjected to a tensile strain in the plane by the  $\text{SrTiO}_3$  substrate. This reduces the out-of-plane lattice constant of the  $\text{LaAlO}_3$  film, which therefore cannot be directly compared to the bulk value. One possibility is to calculate the strain effect using the Poisson's ratio of  $\text{LaAlO}_3$ , which is reported to be  $\approx 0.25$  [85]. This may cause a nontrivial error, however, because of the limited accuracy of this elastic constant and the probable crystalline-quality dependence of it.

Another possible approach is to relieve the lattice mismatch between the  $\text{LaAlO}_3$  film and the  $\text{SrTiO}_3$  substrate, which enables a direct comparison of the film lattice constant to that of bulk  $\text{LaAlO}_3$ . A common strategy to relieve the lattice mismatch is to insert buffer layers between the film and the substrate, as reported for conventional semiconductors [86, 87] and also for some oxides [88–93]. In the following sections, we present the successful relief of the lattice mismatch between the  $\text{LaAlO}_3$  film and the  $\text{SrTiO}_3$  substrate using a “ $\text{SrAlO}_x$ ” buffer layer.

## 4.3 Fabrication of bulk-like single crystal $\text{LaAlO}_3$ thin films on $\text{SrTiO}_3$ (001) using “ $\text{SrAlO}_x$ ” buffer layers

### 4.3.1 Original motivation to use $\text{SrAlO}_x$

An original motivation to use  $\text{SrAlO}_x$  is to have an analogue of  $\text{LaTiO}_3$  to control  $\text{LaAlO}_3/\text{SrTiO}_3$  (001) interfaces in *superlattices*, without losing the repeated perovskite unit [15]. It has been shown that this interface becomes conducting when  $\text{LaAlO}_3$  is deposited directly on a  $\text{TiO}_2$ -terminated  $\text{SrTiO}_3$  surface, whereas one monolayer of  $\text{SrO}$  inserted before the  $\text{LaAlO}_3$  makes the interface insulating [14, 48]. In an ideal picture, the structures of these two interfaces are  $\text{AlO}_2/\text{LaO}/\text{TiO}_2$ , and  $\text{AlO}_2/\text{SrO}/\text{TiO}_2$  respectively. As explained in Sec. 2.3.2,

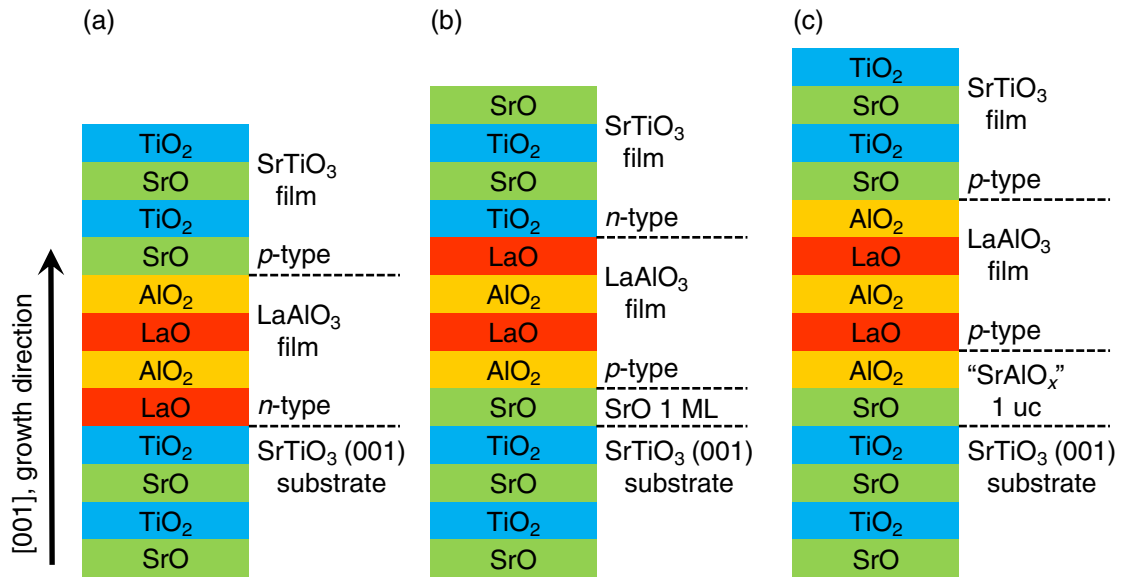


Fig. 4.3 Schematic illustration of the fabrication of LaAlO<sub>3</sub>/SrTiO<sub>3</sub> (001) multilayers. (a) Fabrication with only LaAlO<sub>3</sub>. (b) Fabrication using SrO insertion. ML: monolayer. (c) Fabrication using SrAlO<sub>x</sub> insertion.

these two are often named as *n*-type and *p*-type interfaces, respectively.

However, in the context of superlattice fabrication, SrO is unsuitable since it does not maintain the repeated perovskite unit: as shown in Fig. 4.3(b), further deposition of SrTiO<sub>3</sub> on the LaAlO<sub>3</sub> film creates an *n*-type interface, and SrO cannot be used for changing the termination of this *n*-type interface.<sup>\*1</sup> In contrast, 1 uc of SrAlO<sub>x</sub> can change the interface termination without losing the perovskite structure, as shown in Fig. 4.3(c). In this case, further deposition of SrTiO<sub>3</sub> on the LaAlO<sub>3</sub> film creates a *p*-type interface, the same interface as that without SrAlO<sub>x</sub> [Fig. 4.3(a)].

While this original motivation is not directly linked to the main focus of this Chapter, we have also examined this possible advantage of SrAlO<sub>x</sub>. Details are summarized in App. C.

### 4.3.2 Fabrication and analysis of the SrAlO<sub>x</sub> target

One problem in using SrAlO<sub>x</sub> is that it is not a perovskite, nor stable as a single phase in bulk. Naively it might be expected that  $x = 3$ , but this composition cannot maintain charge neutrality due to the fixed valence of the Sr and Al ions (Sr<sup>2+</sup> and Al<sup>3+</sup>, respectively). The charge-neutral composition is  $x = 2.5$ , or Sr<sub>2</sub>Al<sub>2</sub>O<sub>5</sub>, but there is no bulk compound having this ratio.

Thus in this study, a mixture of Sr<sub>3</sub>Al<sub>2</sub>O<sub>6</sub> and SrAl<sub>2</sub>O<sub>4</sub> was used as the SrAlO<sub>x</sub> target. The target was fabricated from a 2 : 1 mixture of SrCO<sub>3</sub> and Al<sub>2</sub>O<sub>3</sub> which was sintered in oxygen at 1400 °C for 14 h, ground, and re-sintered in the same conditions. The target's constituent materials were confirmed by means of powder XRD analysis [Fig. 4.4].

Since the target material is transformed into a plasma during the growth by PLD, a multi-phase target can still be used successfully, so long as the cation ratio in the mixture is the same

<sup>\*1</sup> One monolayer of AlO<sub>x</sub>, or more generally speaking, compensation of the "BO<sub>2</sub>" layer is necessary.

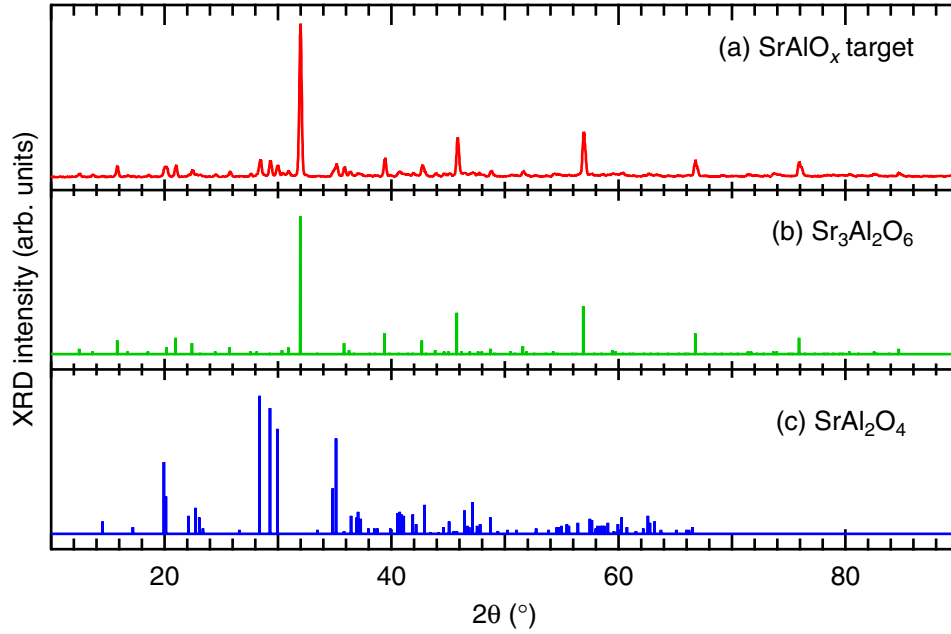


Fig. 4.4 (a) Powder XRD pattern of the SrAlO<sub>x</sub> target. (b) Reference pattern of Sr<sub>3</sub>Al<sub>2</sub>O<sub>6</sub> (JCPDS No. 24-1187). (c) That of SrAl<sub>2</sub>O<sub>4</sub> (JCPDS No. 34-0379).

as that of perovskites. Also, the non-equilibrium nature of PLD and epitaxial stabilization may enable the perovskite structure to be maintained when the SrAlO<sub>x</sub> layer is sufficiently thin. We have investigated this possibility below.

### 4.3.3 Details of film growth

Each sample was grown by PLD on a commercially-available 5×5 mm<sup>2</sup> SrTiO<sub>3</sub> (001) substrate with a TiO<sub>2</sub>-terminated surface [94, 95] (Shinkosha Co.). The substrate miscut angle was ≈ 0.1°, approximately towards the [100] direction, in plane. Before growth the substrates were preannealed at substrate temperature  $T_{\text{sub}} = 950$  °C in oxygen partial pressure  $P_{\text{O}_2} = 5 \times 10^{-6}$  Torr for 30 mins. Following this anneal,  $T_{\text{sub}}$  was reduced to 700 °C and  $P_{\text{O}_2}$  was increased to  $1 \times 10^{-5}$  Torr, the film growth conditions. The SrAlO<sub>x</sub> target mentioned and single crystal SrTiO<sub>3</sub> and LaAlO<sub>3</sub> targets were used. The laser parameters used were: laser energy  $E = 28$  mJ, spot area  $A = 1.5 \times 1.5$  mm<sup>2</sup>, and fluence  $f = E/A = 1.2$  J/cm<sup>2</sup>. The laser repetition rate was 4 Hz.

Figure 4.5(a) shows a schematic illustration of the sample structure. The thickness of each layer was monitored *in situ* using RHEED. It should be noted that the thicknesses of the SrAlO<sub>x</sub> layers were calibrated using the first peaks of the RHEED oscillations, as shown in Fig. 4.5(b). Although the first peaks were observed at different times in each experiment, ascribed to the changes in the laser fluence [74], the transition of the strain state of the LaAlO<sub>3</sub> films with the SrAlO<sub>x</sub> thickness described below was reproducible regardless of the time at which the peak was observed. In this set of experiments, a 10 uc homoepitaxial layer of SrTiO<sub>3</sub> was grown before the SrAlO<sub>x</sub> to improve the RHEED oscillations during the subsequent growth [96]. After the SrAlO<sub>x</sub> growth, a fixed thickness of LaAlO<sub>3</sub> of 100 uc was grown, and the

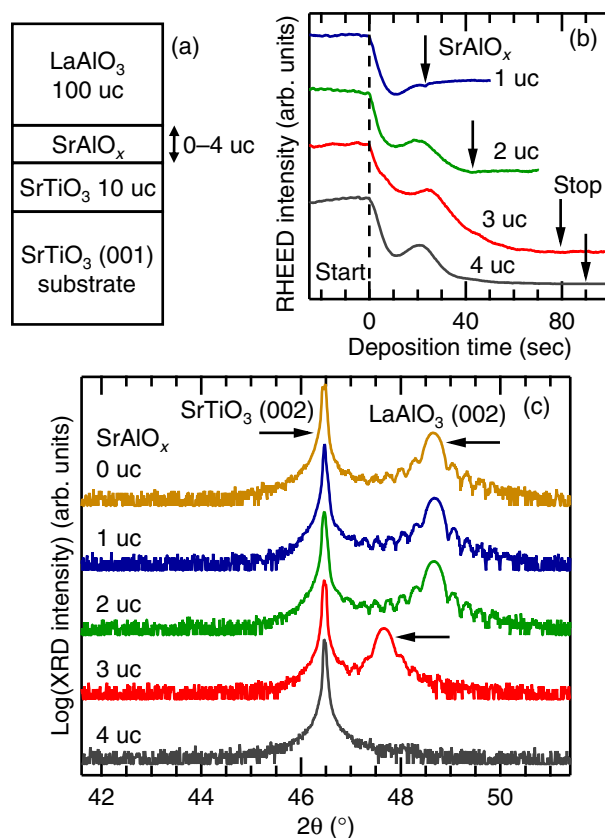


Fig. 4.5 (a) Schematic illustration of the sample structure. (b) RHEED oscillations during the growth of  $\text{SrAlO}_x$  layers. (c) XRD  $\theta$ - $2\theta$  patterns of the samples.

samples were cooled to room temperature at the deposition pressure.

#### 4.3.4 Characterization of film crystallinity by XRD and AFM

Figure 4.5(c) shows the XRD  $\theta$ - $2\theta$  patterns of the samples with various  $\text{SrAlO}_x$  thicknesses. Clear  $\text{LaAlO}_3$  (002) peaks are observed from all the samples except for the 4 uc thick  $\text{SrAlO}_x$  interlayer sample. This can be interpreted that the relatively thick  $\text{SrAlO}_x$  interlayer, which has non-perovskite crystal structures in bulk, harms the single-crystalline growth of the  $\text{LaAlO}_3$  film. In contrast, the samples with 1 and 2 uc thick  $\text{SrAlO}_x$  interlayers show essentially the same diffraction patterns as that of the sample with no  $\text{SrAlO}_x$  interlayer. The out-of-plane lattice constants of these three films are found to be 0.374 nm, significantly shorter than that of bulk  $\text{LaAlO}_3$ . This is expected, since the  $\text{LaAlO}_3$  films are subjected to a tensile strain in the plane by the  $\text{SrTiO}_3$  substrates, which reduces the out-of-plane lattice constant. The Laue fringe peaks and the FWHM of the  $\text{LaAlO}_3$  (002) peaks are in good agreement with the nominal thickness of 100 uc, suggesting that the out-of-plane lattice constant is homogeneous throughout the  $\text{LaAlO}_3$  films.

Most notably, the 3 uc  $\text{SrAlO}_x$  sample also shows a clear  $\text{LaAlO}_3$  (002) peak, but at a much smaller angle. The out-of-plane lattice constant is found to be 0.381 nm, 0.5% larger than that of bulk  $\text{LaAlO}_3$ . In this case also the Laue fringe peaks, although less clear, and the FWHM

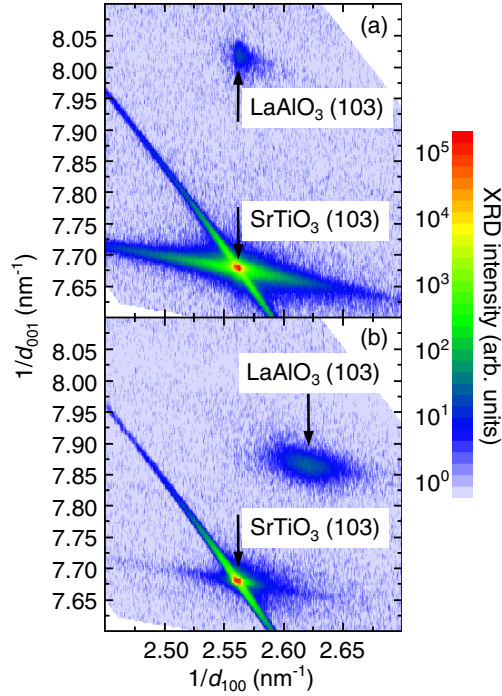


Fig. 4.6 XRD reciprocal space maps of the samples with (a) no  $\text{SrAlO}_x$  interlayer and (b) a 3 uc  $\text{SrAlO}_x$  interlayer.

suggest that the  $\text{LaAlO}_3$  film is quite homogeneous.

To further investigate the structure of these films, we measured the off-axis XRD peaks. Figure 4.6 shows the reciprocal space maps in the vicinity of the  $\text{SrTiO}_3$  (103) and the  $\text{LaAlO}_3$  (103) peaks for two of the samples. From the sample without  $\text{SrAlO}_x$  [Fig. 4.6(a)], no significant in-plane difference is observed between the substrate and film peaks, indicating that the  $\text{LaAlO}_3$  in-plane lattice constant is locked to the  $\text{SrTiO}_3$  substrate. No satellite peak associated with strain distribution is observed, indicating that the  $\text{LaAlO}_3$  film is fully strained.

In contrast, the sample with a 3 uc thick  $\text{SrAlO}_x$  interlayer [Fig. 4.6(b)] shows a significant in-plane difference between the substrate and film peaks. Both the in- and out-of-plane lattice constants of the  $\text{LaAlO}_3$  film are found to be 0.381 nm, indicating that the  $\text{LaAlO}_3$  film is free from strain in the plane, and its crystal structure is essentially that of the bulk. The small (0.5%) difference between the relaxed  $\text{LaAlO}_3$  film lattice constant and the bulk value is interpreted as due to cation non-stoichiometry in the film, as explained in Sec. 4.2.

Figures 4.7(a) and (b) show the AFM surface topography of the  $\text{LaAlO}_3$  films without  $\text{SrAlO}_x$  and with a 3 uc  $\text{SrAlO}_x$  interlayer, respectively. Both films have flat terraces with a root-mean-square roughness of  $\approx 0.1$  nm and clear 1 uc height ( $\approx 0.4$  nm) steps. Over a larger scale of  $20 \times 20 \mu\text{m}^2$  the strained  $\text{LaAlO}_3$  films ( $\text{SrAlO}_x$  thickness = 0–2 uc) show some surface features that suggest cracking associated with the local relaxation. On the other hand, no such features were observed on the relaxed  $\text{LaAlO}_3$  film ( $\text{SrAlO}_x$  thickness = 3 uc), suggesting that the lattice mismatch is relieved in the  $\text{SrAlO}_x$  interlayer.

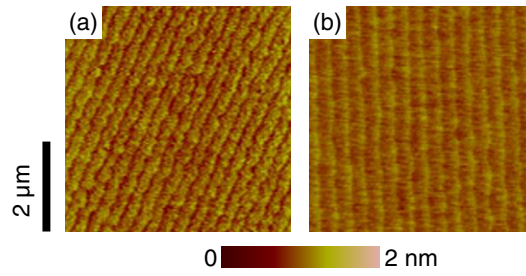


Fig. 4.7 AFM surface topography of the  $\text{LaAlO}_3$  films with (a) no  $\text{SrAlO}_x$  interlayer and (b) a 3 uc  $\text{SrAlO}_x$  interlayer.

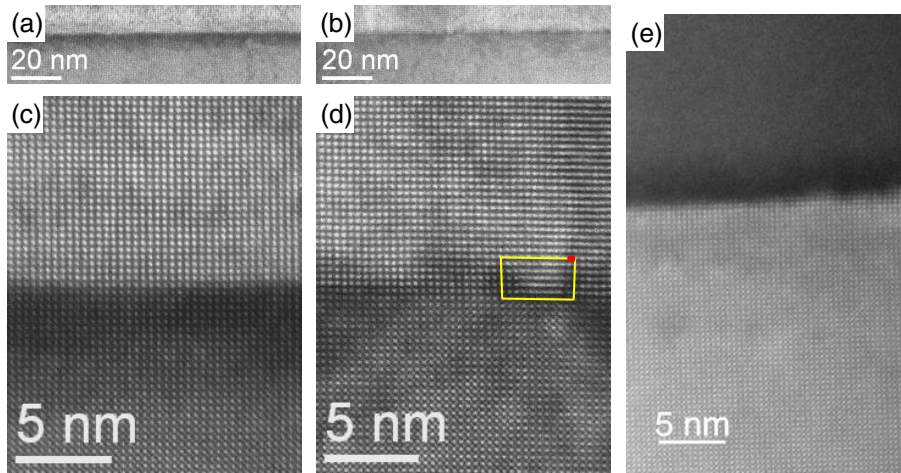


Fig. 4.8 High-angle annular dark field STEM images of the samples with (a) no  $\text{SrAlO}_x$  and (b) a 3 uc  $\text{SrAlO}_x$  interlayer. (c) and (d) are magnified images of (a) and (b), respectively. In (d), a Burgers circuit (yellow line) and the Burgers vector (red bold line) are also drawn, indicating an edge dislocation. (e) Image of the sample with a 4 uc  $\text{SrAlO}_x$  interlayer.

### 4.3.5 Microstructural details by STEM

To understand the changes on the nanoscale occurring at the 3 uc critical thickness, high-angle annular dark field scanning transmission electron microscopy (STEM) images were taken by Julia A. Mundy at Cornell University. Figures 4.8(a) and (b) show the STEM images of the samples without an interlayer and with a 3 uc  $\text{SrAlO}_x$  interlayer, respectively. Figures 4.8(c) and (d) show magnified images of the same samples. As expected from the XRD data, both of the  $\text{LaAlO}_3$  films are fully crystalline and  $c$ -axis oriented.

The  $\text{LaAlO}_3$  film with no  $\text{SrAlO}_x$  is clearly epitaxially grown on the  $\text{SrTiO}_3$  substrate, with no obvious dislocations at the interface [Figs. 4.8(a) and (c)]. On the other hand, the  $\text{LaAlO}_3$  film with a 3 uc thick  $\text{SrAlO}_x$  interlayer shows many edge dislocations around the interface [Figs. 4.8(b) and (d)], relieving the lattice mismatch between the film and the substrate. We also see multi-domain structures in the relaxed  $\text{LaAlO}_3$  film, which is consistent with the significant in-plane broadening of the XRD peak [Fig. 4.6(b)]. This multi-domain state may also have a partial contribution to the strain relaxation, and might be eliminated by employing high miscut

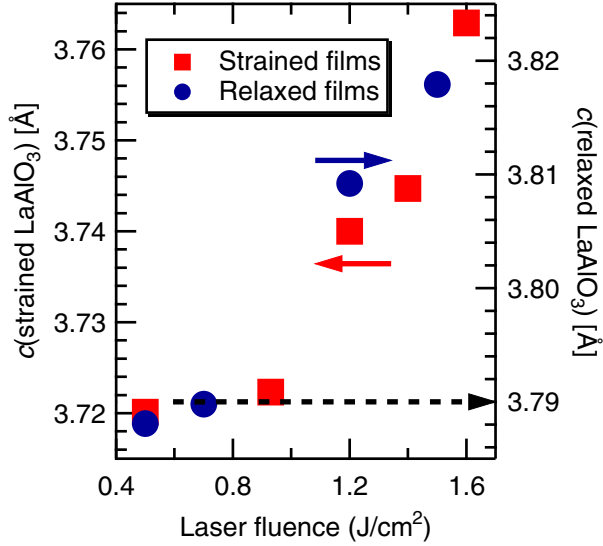


Fig. 4.9 Out-of-plane lattice constant of LaAlO<sub>3</sub> films grown at various fluences. Dashed line denotes the expected value for a stoichiometric LaAlO<sub>3</sub> bulk crystal.

substrates [92, 97]. The LaAlO<sub>3</sub> above the 4 uc thick SrAlO<sub>x</sub> layer, which showed no XRD peak, was also confirmed to be amorphous by the STEM measurement [Fig. 4.8(e)].

#### 4.4 Laser parameter dependence of the lattice expansion of LaAlO<sub>3</sub> films

Having established a fabrication method of strain-relaxed LaAlO<sub>3</sub> films on SrTiO<sub>3</sub> (001) substrates, we have utilized this method to evaluate the LaAlO<sub>3</sub> film lattice constant as a function of the laser fluence. Figure 4.9 shows the out-of-plane lattice constant of LaAlO<sub>3</sub> films grown at various fluences, with other growth parameters fixed as used above. Here “strained” denotes the LaAlO<sub>3</sub> films directly grown on the SrTiO<sub>3</sub> substrates, and “relaxed” denotes the films grown with the lattice mismatch relieved by a 3 uc SrAlO<sub>x</sub> buffer.

As seen in the figure, a significant variation of the lattice constant is found, indicating a modulation of the LaAlO<sub>3</sub> film stoichiometry by the fluence, as reported for SrTiO<sub>3</sub> [81, 82]. Both the strained and relaxed film series show a similar fluence dependence, suggesting that the strain energy has only a small, if any, effect on the film stoichiometry. The out-of-plane lattice constant of the relaxed LaAlO<sub>3</sub> film grown at a fluence of 0.7 J/cm<sup>2</sup> is found to be very close to the bulk value. The out-of-plane lattice constant of the strained LaAlO<sub>3</sub> film grown at a similar fluence is found to be  $\approx 3.72$  Å. Assuming no effect of the strain energy on the film stoichiometry, the Poisson’s ratio is calculated to be  $\approx 0.26$ , in good agreement with the reported value [85]. These results indicate that the stoichiometric transfer of LaAlO<sub>3</sub> is achieved at this fluence.

## 4.5 Summary

We developed a fabrication method of strain-relaxed  $\text{LaAlO}_3$  films on  $\text{SrTiO}_3$  (001) substrates, with which the  $\text{LaAlO}_3$  film stoichiometry was evaluated. It was shown that at the 3 uc critical thickness, the  $\text{SrAlO}_x$  interlayer acts as a sliding buffer layer. The laser condition to achieve the stoichiometric transfer of  $\text{LaAlO}_3$  was determined, and we obtained the out-of-plane lattice constant of the stoichiometric  $\text{LaAlO}_3$  film epitaxially grown on the  $\text{SrTiO}_3$  (001) substrate. Based on these data, the possible effect of the  $\text{LaAlO}_3$  film stoichiometry on the properties of the  $\text{LaAlO}_3/\text{SrTiO}_3$  interface is investigated in the next Chapter.

While not the main focus of this Thesis, we would like to note that this fabrication method may provide a novel approach for strain relaxation of perovskite films far below the thermodynamic critical thickness. In the previous reports on the buffer layers for oxide film growth, single crystal perovskite oxides are mostly used, and the buffer layer thickness is  $\sim 10\text{--}100$  nm [88–93]. By contrast, the buffer material used in this study is not a perovskite in bulk, and the buffer layer thickness is  $\sim 1$  nm. Thus this study describes a new material choice of a buffer layer to control the lattice mismatch, which has a potential advantage for growing oxide artificial heterostructures with nanoscale precision.

## Chapter 5

# Laser Parameter Dependence of the Interface Properties

### 5.1 Introduction

It has been pointed out that the cation stoichiometry of complex oxide films grown by PLD is strongly affected by the laser parameters [81, 82]. Cation non-stoichiometry can strongly modulate the film properties, as reported for cuprates [98], manganites [99], as well as for SrTiO<sub>3</sub> [82]. In Chap. 4, we found a significant variation of the lattice constant of LaAlO<sub>3</sub> films with the fluence, indicating that the LaAlO<sub>3</sub> film stoichiometry is also modulated by the laser parameters. This stoichiometry modulation may have an effect on the physical properties of the LaAlO<sub>3</sub>/SrTiO<sub>3</sub> heterointerface. However, this possibility has not been discussed in the literature, and this can be one of the origins of the variation in the reported properties of this system from different laboratories.

In this Chapter, we investigate the effect of the LaAlO<sub>3</sub> film stoichiometry on the electronic properties of the LaAlO<sub>3</sub>/SrTiO<sub>3</sub> interface. Based on the results in Chap. 4, the film stoichiometry modulation by the laser parameters is examined in more detail, as explained in Sec. 5.2. The laser parameters are found to have a strong effect on the transport properties of this system. Especially, the carrier density is modulated over a wide range, as explained in Sec. 5.3. Such dilute electron systems at the interface may have anisotropic transport properties, as explained and examined in Sec. 5.4.

### 5.2 Laser parameter dependence of LaAlO<sub>3</sub> film stoichiometry

#### 5.2.1 Evaluation methods of LaAlO<sub>3</sub> film stoichiometry

The LaAlO<sub>3</sub> film stoichiometry was evaluated using two different methods. One is the XRD measurement. As pointed out in Refs. [81, 82], cation vacancies in the insulator cause lattice expansion due to Coulomb repulsion. Thus the film lattice constant can be used as a parameter of the film stoichiometry. An advantage of XRD is that this method can evaluate the film

stoichiometry of the same  $\text{LaAlO}_3/\text{SrTiO}_3$  samples as used for the transport measurements, since from the results in Chap. 4, we have obtained the expected out-of-plane lattice constant value for the stoichiometric  $\text{LaAlO}_3$  film epitaxially grown on the  $\text{SrTiO}_3$  substrate. However, XRD is not quantitative, since both La and Al vacancies can cause lattice expansion and thus the XRD measurement alone cannot distinguish which cation is deficient.\*<sup>1</sup>

The other method used is inductively coupled plasma (ICP) spectrometry. The ICP atomic emission spectrometry measurement was done by Mayumi Misaki at Hitachi Kyowa Engineering Co., Ltd. ICP is known as an element-selective and highly quantitative chemical characterization method. However, the volume of the La and Al atoms in typical  $\text{LaAlO}_3/\text{SrTiO}_3$  samples is below the measurement limit of this technique. Thus a separate series of relatively thick  $\text{LaAlO}_3$  films are required for ICP.

### 5.2.2 Details of film growth

Each sample for the XRD and transport measurements (Sec. 5.3) was fabricated by PLD on a  $\text{TiO}_2$ -terminated  $\text{SrTiO}_3$  (001) substrate, as detailed in Secs. 3.1 and 4.3.3. The variable growth parameters were: the laser energy  $E$ , the laser spot size  $A$ , and the laser fluence  $f = E/A$ . The laser repetition rate was 2 Hz. The film growth conditions were:  $T_g = 800$  °C and  $P_{\text{O}_2} = 1 \times 10^{-5}$  Torr. The  $\text{LaAlO}_3$  film thickness was 25 uc. After growth the samples were cooled to room temperature in  $P_{\text{O}_2} = 300$  Torr, with a one hour pause at  $T_{\text{sub}} = 600$  °C. These growth details (other than the laser parameters) are the same as used previously [66].

Film lattice constants were evaluated using the (002) peak of the XRD  $\theta$ - $2\theta$  patterns. The cation stoichiometry of the  $\text{LaAlO}_3$  films was measured by ICP, using  $\sim 400$  nm thick amorphous  $\text{LaAlO}_3$  films grown on  $10 \times 10$  mm<sup>2</sup> B-doped Si substrates\*<sup>2</sup> at room temperature. For these samples, in order to obtain relatively thick films in a practical time, the repetition rate of the laser was increased to 10 Hz, while  $P_{\text{O}_2}$  and the laser conditions were the same as used for the epitaxial growth.

### 5.2.3 Comparison of XRD and ICP results

$\text{LaAlO}_3$  films were grown at nine different laser conditions, consisting from three series as follows: energy-constant series:  $A = 2.5, 3.0, 3.5,$  and  $5.6$  mm<sup>2</sup> at constant  $E = 39$  mJ; fluence-constant series:  $A = 3.0, 4.3$  and  $5.6$  mm<sup>2</sup> at constant  $f = 0.7$  J/cm<sup>2</sup>; area-constant series:  $f = 0.7, 0.9, 1.1, 1.3$  and  $1.6$  J/cm<sup>2</sup> at constant  $A = 3.0$  mm<sup>2</sup>. Note that the conditions ( $A$  [mm<sup>2</sup>],  $f$  [J/cm<sup>2</sup>]) = (3.0, 0.7), (3.0, 1.3) and (5.6, 0.7) are duplicated.

Figures 5.1(a) and (b) show the out-of-plane lattice constant of the  $\text{LaAlO}_3$  films on the  $\text{SrTiO}_3$  substrates, as a function of the laser parameters. As already seen in the previous Chapter, the film lattice constant is significantly modulated by the laser conditions, over a range of 3.725–3.765 Å. The smallest lattice constant is found at ( $A$  [mm<sup>2</sup>],  $f$  [J/cm<sup>2</sup>]) = (3.0, 0.7): at a relatively low fluence. The lattice constant becomes larger as the fluence increased [Fig. 5.1(b)], consistent with the results in Chap. 4.

\*<sup>1</sup> In principle, both sites may have vacancies, while the formation energy can be different.

\*<sup>2</sup> For a technical issue of ICP related to the chemical solubility.

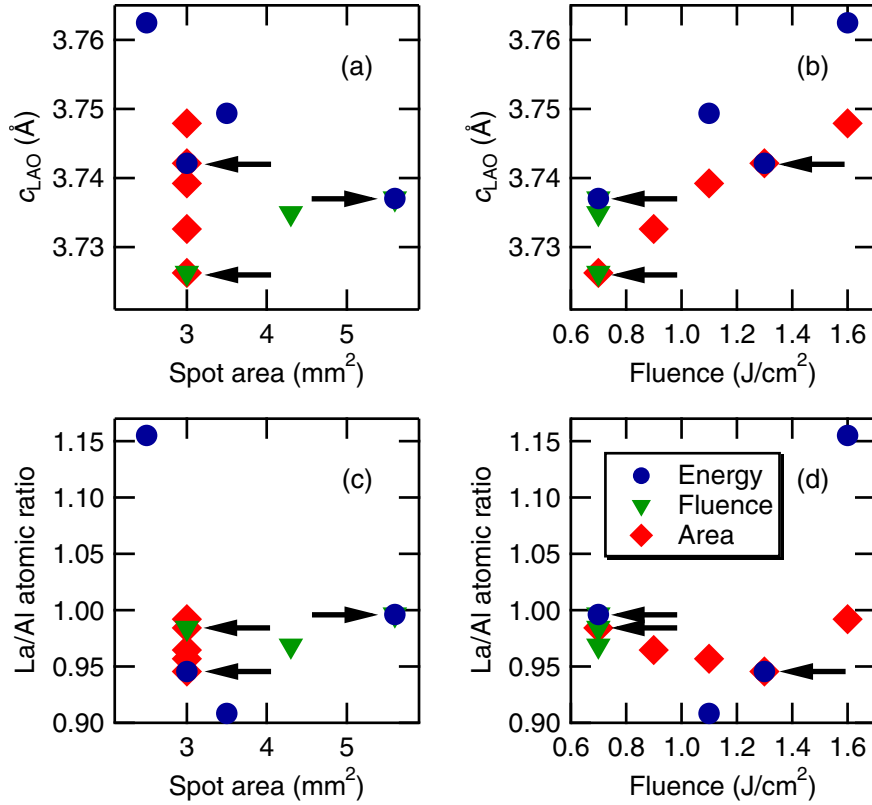


Fig. 5.1 (a), (b) Out-of-plane lattice constant of the  $\text{LaAlO}_3$  films from XRD as a function of the spot area and the fluence, respectively. (c), (d) Cation ratio of the  $\text{LaAlO}_3$  films from ICP as a function of the spot area and the fluence, respectively. Each of the energy-, fluence- and area-constant series has duplicated data points to the others, indicated by the arrows.

Figures 5.1(c) and (d) show the cation stoichiometry obtained from the ICP analysis on the amorphous films, as a function of the laser parameters. All films are La poor, except for the one grown at  $A = 2.5 \text{ mm}^2$  and  $f = 1.6 \text{ J/cm}^2$ . The atomic cation ratio  $r \equiv \text{La/Al}$  is modulated over a range of 0.91–1.16.

To directly compare the data from these two methods, the out-of-plane lattice constant of the epitaxial  $\text{LaAlO}_3$  films was plotted as a function of the cation ratio obtained from the amorphous  $\text{LaAlO}_3$  films grown at the same laser conditions, as shown in Fig. 5.2. The more off-stoichiometric films are found to have larger lattice constants. However, there are two  $\text{LaAlO}_3$  films which have nearly stoichiometric cation ratios but with relatively large lattice constants. Except for these two, the results from XRD and ICP show the trend expected from the previous reports for  $\text{SrTiO}_3$  [81, 82], namely, the more off-stoichiometric films show the larger lattice expansion due to Coulomb repulsion near the cation vacancies. The existence of the two exceptions from this trend is discussed below.

Assuming a linear relation between the out-of-plane lattice constant  $c_{\text{LAO}}$  and the atomic cation ratio  $r$ , a least-squares fitting of the data gives

$$\text{La poor: } c_{\text{LAO}}/\text{\AA} = 3.724 + 0.296(1 - r). \quad (5.1)$$

Here the Al poor data point and the two exceptional data points mentioned are neglected. This

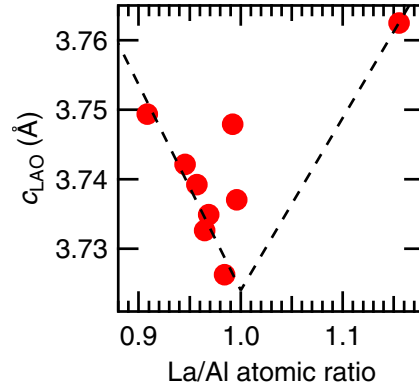


Fig. 5.2 Out-of-plane lattice constant of the epitaxial  $\text{LaAlO}_3$  films, as a function of the cation ratio obtained from the amorphous  $\text{LaAlO}_3$  films grown at the same laser conditions. Dashed lines are guides to the eye.

equation gives the out-of-plane lattice constant of the stoichiometric  $\text{LaAlO}_3$  film of 3.724 Å, in good agreement with the results in Chap. 4.\*<sup>3</sup>

## 5.2.4 Discussion

These results confirm that the  $\text{LaAlO}_3$  film stoichiometry is also modulated by the laser parameters, as reported for other complex oxides [81, 82, 98, 99]. A significant relationship is also found between the film lattice constant and the stoichiometry, consistent with the previous reports for  $\text{SrTiO}_3$  [81, 82]. However, it is also found that at two laser conditions, the results from XRD and ICP show nontrivial disagreement, namely, the cation ratio from ICP is nearly stoichiometric but the film lattice constant from XRD is relatively large.

One possible explanation for the exceptions is that both types of the cation vacancies are induced at these conditions, i.e., the  $\text{LaAlO}_3$  films grown at these conditions have *both* La and Al vacancies. If the films have nearly the same number of La and Al vacancies, they can show an apparently stoichiometric cation ratio *and* lattice expansion. This possibility can be examined by measuring the film mass density, by x-ray reflectivity measurement, for example.

## 5.3 Laser parameter dependence of the electronic properties

### 5.3.1 Laser parameter dependence of the resistance

The effect of the  $\text{LaAlO}_3$  film stoichiometry on the electronic properties of the  $\text{LaAlO}_3/\text{SrTiO}_3$  interface was examined using the same 25 uc  $\text{LaAlO}_3/\text{SrTiO}_3$  samples as in Sec. 5.2. Another three 5 uc  $\text{LaAlO}_3/\text{SrTiO}_3$  samples were also grown at (a)  $A = 3.0 \text{ mm}^2$ ,  $f = 0.7 \text{ J/cm}^2$ , (b)  $A = 5.6 \text{ mm}^2$ ,  $f = 0.7 \text{ J/cm}^2$  and (c)  $A = 3.0 \text{ mm}^2$ ,  $f = 1.6 \text{ J/cm}^2$ .

Figure 5.3 shows the temperature dependence of the sheet resistance of the 5 uc and 25 uc

\*<sup>3</sup> The small ( $\approx 0.004 \text{ \AA}$ ) difference can be explained by the finite effect of the interference between the film and the substrate in XRD, which shifts the film peak towards the substrate peak and gives an apparently larger lattice constant. Note that the films in Chap. 4 are much thicker. See App. A for details.

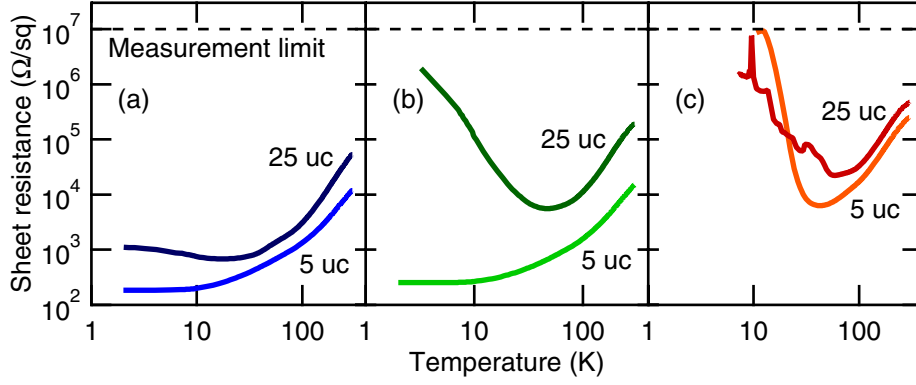


Fig. 5.3 Temperature dependence of the sheet resistance of the 5 and 25 uc  $\text{LaAlO}_3/\text{SrTiO}_3$  samples grown at (a)  $A = 3.0 \text{ mm}^2$ ,  $f = 0.7 \text{ J/cm}^2$ , (b)  $A = 5.6 \text{ mm}^2$ ,  $f = 0.7 \text{ J/cm}^2$ , and (c)  $A = 3.0 \text{ mm}^2$ ,  $f = 1.6 \text{ J/cm}^2$ .

samples grown at these conditions. At all conditions the thicker samples are found to be more resistive, qualitatively consistent with the previous report [66]. However, there are notable differences as follows.

First, the thickness dependence of the resistance of the samples grown at condition (b) is much more distinct compared to the other two conditions. While the sheet resistances of the 5 uc samples grown at conditions (a) and (b) are identical within the experimental error, those of the 25 uc samples are qualitatively and quantitatively different: the sample grown at condition (b) is more resistive at all temperatures and shows more distinct upturn in the resistance at low temperature.

Second, the 5 uc sample grown at condition (c) is highly resistive and shows even more distinct upturn in the resistance at low temperature, contrary to the 5 uc samples grown at conditions (a) and (b). The 25 uc sample is also highly resistive, but the thickness dependence is relatively weak. The electronic contact to these samples is poor at low temperatures (discussed in more detail below).

The Hall effect measurements of the 5 uc and 25 uc samples grown at condition (b) reveal that the carrier density decreases in the thicker sample [Fig. 5.4(a)]. The Hall mobility also decreases [Fig. 5.4(b)], but the magnitude is smaller compared to that of the carrier density. Especially at 100 K, the difference of the Hall mobility of these samples is only a factor of less than 2, whereas the carrier density difference is an order of magnitude.

### 5.3.2 Carrier density scaling

To further investigate the carrier density modulation by the laser parameters, the Hall effect was measured for all of the 25 uc  $\text{LaAlO}_3/\text{SrTiO}_3$  samples. All samples were found to be conducting enough at 100 K to obtain a clear data set. The Hall mobilities of these samples showed only a small variation at 100 K, within a factor of 2, consistent with the previous report for bulk  $\text{SrTiO}_3$  over a range of three-dimensional carrier densities of  $1.4 \times 10^{17}$ – $2.8 \times 10^{19} \text{ cm}^{-3}$  [34].

Figures 5.5(a) and (b) show the sheet carrier density of the 25 uc  $\text{LaAlO}_3/\text{SrTiO}_3$  samples at 100 K as a function of the cation ratio from ICP and the out-of-plane lattice constant of the

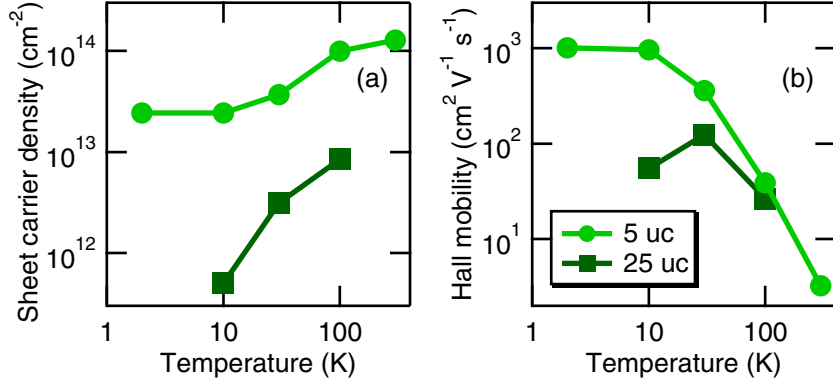


Fig. 5.4 Temperature dependence of (a) the sheet carrier density and (b) the Hall mobility of the 5 uc and 25 uc LaAlO<sub>3</sub>/SrTiO<sub>3</sub> samples grown at  $A = 5.6 \text{ mm}^2$ ,  $f = 0.7 \text{ J/cm}^2$ . Lines are guides to the eye.

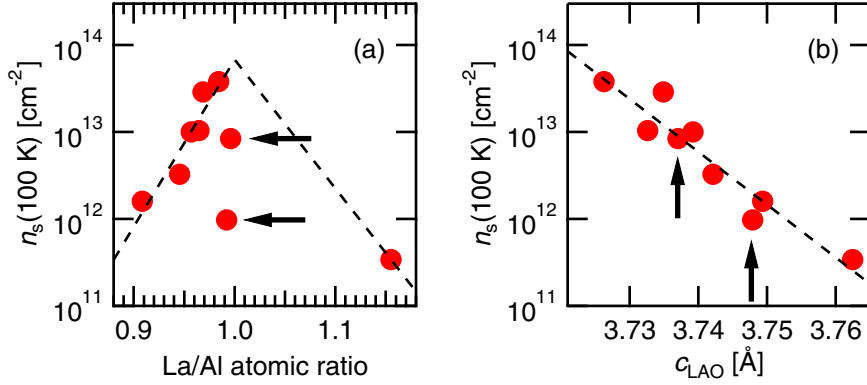


Fig. 5.5 Sheet carrier density of the 25 uc LaAlO<sub>3</sub>/SrTiO<sub>3</sub> samples at 100 K as a function of (a) the cation ratio from ICP and (b) the out-of-plane lattice constant of the LaAlO<sub>3</sub> film. Dashed lines are guides to the eye. Arrows indicate the stoichiometric samples but with relatively large lattice constants (see text for details).

LaAlO<sub>3</sub> film, respectively. There is a clear and significant relationship between the film stoichiometry, the lattice constant and the carrier density. The samples with more off-stoichiometric films are found to have smaller carrier densities [Fig. 5.5(a)]. However, there are two distinct exceptions, as mentioned above: the two LaAlO<sub>3</sub> films which have nearly stoichiometric cation ratios but relatively larger lattice constants. By contrast, all the carrier densities seem to be scaled with the film lattice constant, including the two “exceptional” samples [Fig. 5.5(b)], implying that the film lattice constant is a more relevant parameter.

It should be noted that the measurement error of the data in Fig. 5.5 has been estimated to be small, as detailed below. Figure 5.6(a) shows the two-point current–voltage ( $I$ – $V$ ) characteristics at 2 K of the sample with the second lowest carrier density. The contact is found to be clearly non-Ohmic. The  $I$ – $V$  curves are noisy and nonlinear, indicating poor contact. By contrast, the  $I$ – $V$  curves are linear at 100 K, as shown in Fig. 5.6(b). The Hall resistance is also linear with the magnetic field with little noise, as shown in Fig. 5.6(c), and consequently the error in  $n_s(100 \text{ K})$  is estimated to be less than 1%. The error bar is much smaller than the point size in Fig. 5.5.

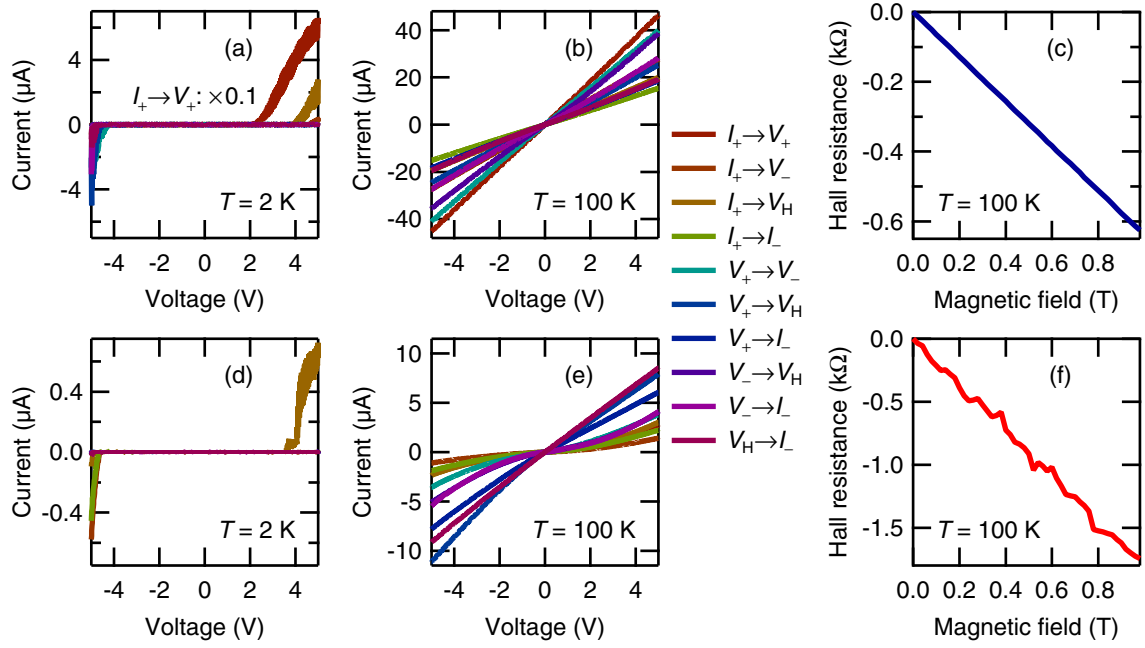


Fig. 5.6 (a) Two-point current–voltage characteristics at 2 K of the sample grown at  $A = 3.0 \text{ mm}^2$ ,  $f = 1.6 \text{ J/cm}^2$ . (b) Same data for 100 K. (c) Antisymmetrized Hall resistance of the same sample at 100 K ( $n_s(100 \text{ K}) = 9.76 \times 10^{11} \text{ cm}^{-2}$ ). (d) Two-point current–voltage characteristics at 2 K of the sample grown at  $A = 2.5 \text{ mm}^2$ ,  $f = 1.6 \text{ J/cm}^2$ . (e) Same data for 100 K. (f) Antisymmetrized Hall resistance of the same sample at 100 K ( $n_s(100 \text{ K}) = 3.41 \times 10^{11} \text{ cm}^{-2}$ ).

Figures 5.6(d) and (e) show the two-point  $I$ – $V$  characteristics of the sample with the lowest carrier density at 2 K and at 100 K, respectively. The contact is found to be clearly non-Ohmic at the lowest temperature [Fig. 5.6(d)]. Contrary to the previous sample, the  $I$ – $V$  curves are significantly nonlinear even at 100 K [Fig. 5.6(e)], although the nonlinearity is much smaller than at low temperatures. Consequently the Hall voltage measurement shows a considerable noise, as shown in Fig. 5.6(f). However, the slope of the Hall resistance is still reasonably well-defined. The error in  $n_s(100 \text{ K})$  is estimated to be  $\lesssim 10\%$ : the error bar is still smaller than the point size in Fig. 5.5.

### 5.3.3 Discussion

The laser parameters are found to modulate the carrier density over a wide range. The lowest carrier density realized is  $n_s(100 \text{ K}) = 3.4 \times 10^{11} \text{ cm}^{-2}$ . However, as seen in Figs. 5.3(b) and (c), these 25  $\mu\text{c}$  samples are often highly resistive at low temperatures, and correspondingly the mobility at the lowest temperature is low, often unmeasurable. This suggests that the electrons are strongly localized especially at low temperatures, and the strength of the localization can be effectively modulated by the laser parameters.

One possible explanation is that the high kinetic energy of the ablated species in PLD induces defects near the  $\text{SrTiO}_3$  substrate surface. It is reported that the irradiation of high-energy ions on  $\text{SrTiO}_3$  creates an amorphous layer on the surface [100]. Of course no amorphous layer

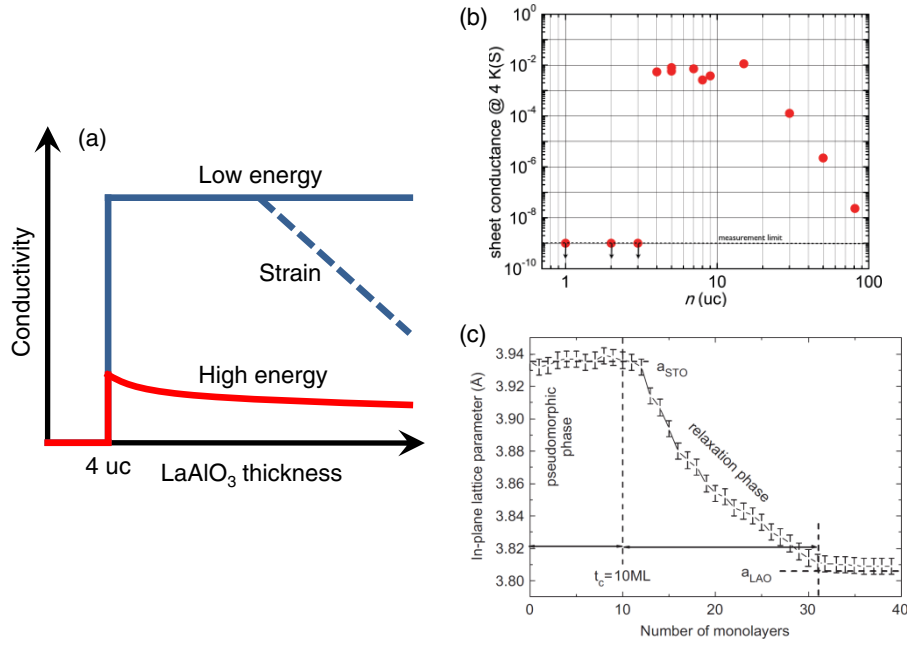


Fig. 5.7 (a) Schematic illustration of the expected film thickness dependence of the conductivity at the LaAlO<sub>3</sub>/SrTiO<sub>3</sub> interface, assuming the effect of the kinetic energy of the incoming species in PLD (solid lines) or the strain energy in the film (dashed line). The critical thickness of 4 uc required for the conductivity [22] is assumed to be universal. (b) Conductance at the LaAlO<sub>3</sub>/SrTiO<sub>3</sub> interface at 4 K as a function of the LaAlO<sub>3</sub> film thickness, from Caviglia [103]. (c) In-plane lattice constant of LaAlO<sub>3</sub> films on SrTiO<sub>3</sub> (001), grown by molecular beam epitaxy, as a function of the film thickness, from Merckling *et al.* [104].

should be created in this study (otherwise the LaAlO<sub>3</sub> film cannot be epitaxial), but still this report indicates that if the kinetic energy of the ablated species is high enough, it may induce defects which localize the electrons. The irradiated ions in Ref. [100] are 300 eV Ar<sup>+</sup>. On the other hand, the maximum kinetic energy of the ablated species in PLD is reported to be ~ 50 eV in high vacuum [101], but can be even higher when the laser fluence increases [102].

This possibility can explain the high resistivity in the samples grown at relatively high fluences [Fig. 5.3(c)]. Since the deposition of the first few layers is expected to be the most relevant for this possible introduction of defects, it can also explain the relatively weak thickness dependence. The expected thickness dependence within this picture is schematically shown in Fig. 5.7(a).

On the other hand, at a relatively low fluence, high resistivity is observed *only* in the thicker sample [Fig. 5.3(b)]. This qualitatively different thickness dependence of the conductivity suggests that there is another origin of the defects. More detailed studies on the thickness dependence of the conductivity show that the decrease of the conductivity becomes apparent only above 10–20 uc [66, 103], as shown in Fig. 5.7(b). This trend is reminiscent of the critical thickness for the strain relaxation [104], as shown in Fig. 5.7(c).

If the strain energy and/or the strain relaxation of the LaAlO<sub>3</sub> film has something to do with the conductivity, it may explain this type of thickness dependence, as also schematically shown

in Fig. 5.7(a). Also, since the lattice expansion of the  $\text{LaAlO}_3$  films caused by cation non-stoichiometry would change the strain energy, this possibility could explain the importance of the film stoichiometry and the lattice constant [Figs. 5.5(a) and (b)]. The remaining question is why the strain energy and/or the strain relaxation of the robust insulator film is relevant for the conductivity in the substrate. One possibility is the introduction of dislocations near the interface [105]. Another possibility might be the tiny, but non-zero compressible strain near the substrate surface by the  $\text{LaAlO}_3$  film, which could induce a polarization in  $\text{SrTiO}_3$  [42]. It is not obvious whether these factors can localize the electrons even at relatively high temperatures, and further investigation is needed to clarify this issue.

While the microscopic origin of the carrier density modulation remains an open question, phenomenologically it is clear that we can tune the carrier density by controlling the laser parameters. As mentioned, the mobility of these samples are often low especially at low temperatures, and in the next Chapter we investigate another growth parameter to enhance the mobility.

## 5.4 Possibility of step anisotropy

### 5.4.1 Step and terrace structure at the interface

The *exact* (001) surface is a perfect plane [Fig. 5.8(a)]. However, practically (001) substrate surfaces have an inevitable miscut from the exact (001) plane, and the surface (often called the *vicinal* surface) has a step-and-terrace structure resulting from the miscut [Fig. 5.8(a)].\*<sup>4</sup> Therefore, the  $\text{LaAlO}_3/\text{SrTiO}_3$  heterointerface fabricated on a vicinal surface in the layer-by-layer growth regime also has this structure.

If the electrons are confined very near to the interface, they may be scattered by the step edges. This scattering effect will induce an in-plane anisotropy of the conductivity in this system. This is the concept of the “step anisotropy.” A system with a strong step anisotropy will no longer be two-dimensional, but rather be well described as weakly coupled pseudo one-dimensional wires.

Huijben [106] has reported a possible step anisotropy at the  $\text{LaAlO}_3/\text{SrTiO}_3$  interface, but concluded that this was not an intrinsic property. Previous studies in our group have shown no obvious evidence for the step anisotropy in this system [107, 108]. These results could be

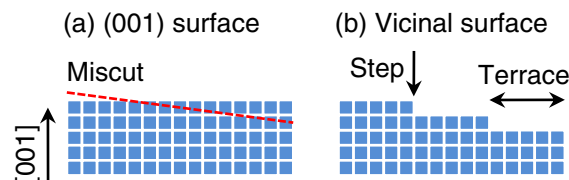


Fig. 5.8 Schematic illustration of (a) the ideal (001) surface and (b) the vicinal surface and the step-and-terrace structure resulting from the inevitable miscut.

\*<sup>4</sup> Typical miscut angle is of the order of  $0.1^\circ$ , which corresponds to an average terrace width of  $\approx 200$  nm.

interpreted that the thickness of the electron gas, reported to be  $\sim 10$  nm in the literature [62–65],<sup>\*5</sup> is much larger than the typical height of the step edges of  $\approx 0.4$  nm, and thus most (or all) of the electrons do not feel the scattering potential.

In this study, however, we have found a strong carrier density modulation by the laser parameters over a wide range. The lowest carrier density realized is  $n_s(100\text{ K}) = 3.4 \times 10^{11}\text{ cm}^{-2}$ , much smaller than the typical value in the literature ( $\gtrsim 10^{13}\text{ cm}^{-2}$ ; see the supplementary material of Ref. [109] for a review). If the carrier density decreases by an order or two, the subband occupation and the self-consistent potential of the electrons at the interface can be quite different. Thus the thickness of the electron gas, and the scattering effect of the step edges, can also be different in such a low carrier density regime. In this Section we examine this possibility.

### 5.4.2 Details of patterning process

The possibility of the step anisotropy was examined using a “star-patterned” sample. Figure 5.9 shows schematically the fabrication process. The star pattern was defined by photolithography using amorphous  $\text{AlO}_x$  as a hard mask, and the electrodes were made by  $\text{Ar}^+$  ion etching and metal deposition. Details of the fabrication process were as follows.

The star-patterned sample was fabricated on a  $5 \times 5\text{ mm}^2$   $\text{SrTiO}_3$  (001) substrate with a  $\text{TiO}_2$ -terminated surface [94, 95]. The as-received substrate was coated by a photoresist [Fig. 5.9(a)], and ultraviolet light was irradiated on the substrate surface through a positive mask to define the star pattern [Fig. 5.9(b)]. The photoresist on the irradiated area was removed by a developer [Fig. 5.9(c)]. The substrate was transferred into the PLD chamber, and the  $\text{AlO}_x$  hard mask was deposited by PLD at room temperature in  $P_{\text{O}_2} = 1 \times 10^{-4}$  Torr [Fig. 5.9(d)]. The remaining photoresist and the  $\text{AlO}_x$  on it were removed by acetone *ex situ* [Fig. 5.9(e)]. The substrate was transferred into the PLD chamber again, and preannealed at  $T_{\text{sub}} = 950\text{ }^\circ\text{C}$  in  $P_{\text{O}_2} = 5 \times 10^{-6}$  Torr for 30 mins [Fig. 5.9(f)]. Following this anneal,  $T_g$  was reduced to  $800\text{ }^\circ\text{C}$  and  $P_{\text{O}_2}$  was increased to  $1 \times 10^{-5}$  Torr, the film growth conditions [Fig. 5.9(g)]. The  $\text{LaAlO}_3$  film was grown at  $A = 2.5\text{ mm}^2$  and  $f = 1.6\text{ J/cm}^2$ . The laser repetition rate was 2 Hz. The  $\text{LaAlO}_3$  thickness was 5 uc, as monitored using RHEED. After growth the sample was cooled to room temperature in  $P_{\text{O}_2} = 300$  Torr, with a one hour pause at  $T_{\text{sub}} = 600\text{ }^\circ\text{C}$ .

The sample was taken out from the chamber, and the electrode area was defined with a photoresist by the same process as shown in Figs. (a)–(c) [Fig. 5.9(h)]. The sample was then transferred into a high-vacuum chamber, and an  $\text{Ar}^+$  beam accelerated at 500 V was irradiated on the sample surface for 3 mins [Fig. 5.9(i)]. This process was confirmed to etch  $\approx 10$  nm deep holes at the unmasked area, and introduce oxygen vacancies on the surface of the etched holes. The sample was then transferred into another high-vacuum chamber, and Al was deposited on the sample surface, followed by Au [Fig. 5.9(j)]. The sample was taken out from the chamber, and the remaining photoresist and the Au/Al on it were removed by acetone [Fig. 5.9(k)]. After the whole process, the sample was kept at  $150\text{ }^\circ\text{C}$  in dark in air for 24 h [Fig. 5.9(l)].

The laser parameters used have been found to decrease the carrier density most (Sec. 5.3). The thin  $\text{LaAlO}_3$  thickness of 5 uc is employed to avoid the possible effect of the strain energy

---

<sup>\*5</sup> This thickness is still controversial, and presumably temperature dependent, because of the temperature dependent permittivity of  $\text{SrTiO}_3$  [36, 37]. See the supplementary material of Ref. [109] for a review.

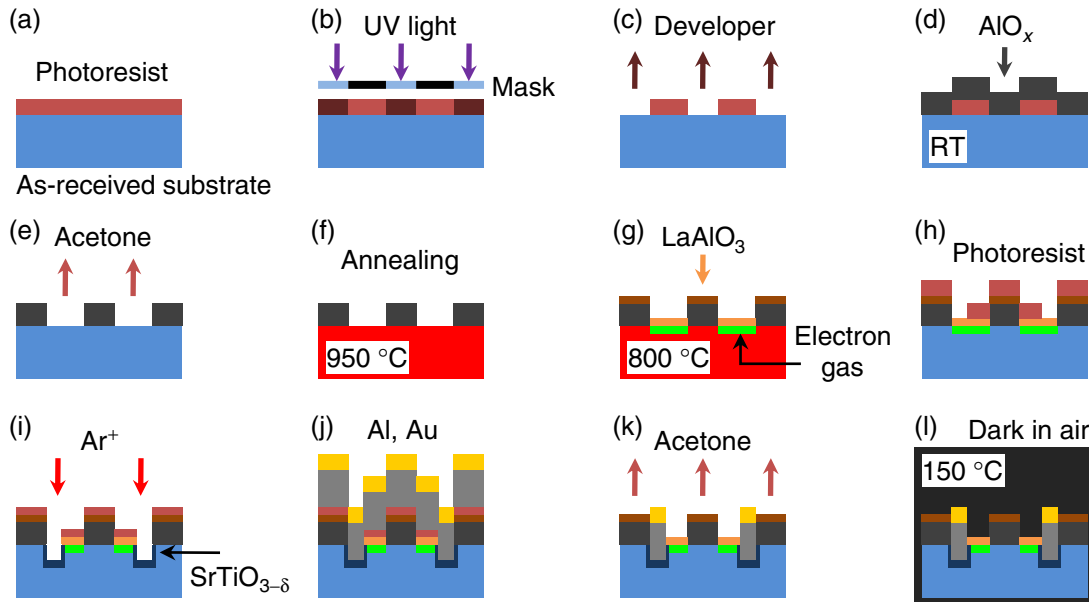


Fig. 5.9 Fabrication process of the star-patterned sample. (a) The as-received  $\text{SrTiO}_3$  substrate is coated by a photoresist. (b) Ultraviolet (UV) light is irradiated through a positive mask to define the star pattern. (c) The photoresist on the irradiated area is removed by a developer. (d)  $\text{AlO}_x$  is deposited by PLD at room temperature (RT). (e) The remaining photoresist and the  $\text{AlO}_x$  on it are removed by acetone. (f) The patterned substrate is preannealed in the PLD chamber. (g)  $\text{LaAlO}_3$  is deposited *in situ*. The electron gas is formed in the unmasked area. (h) The electrode area is defined with photoresist by the same process as shown in (a)–(c). (i) The unmasked area is etched by  $\text{Ar}^+$  ions. The oxygen-deficient  $\text{SrTiO}_{3-\delta}$  is also induced on the surface of the etched holes. (j) Al and Au is deposited *ex situ*. (k) The remaining photoresist and the Au/Al on it are removed by acetone. (l) The sample is kept at  $150^\circ\text{C}$  in dark in air for 24 h.

in the film, which might induce dislocations near the interface, smearing the step-and-terrace structure. The high laser fluence has been found to make the thin sample (as well as the thick sample) highly resistive [Fig. 5.3(c)].

The direct patterning on the  $\text{SrTiO}_3$  substrate might cause some side effect due to the residual contamination on the  $\text{TiO}_2$ -terminated surface, as cautioned in Ref. [110]. In this study, the substrate was preannealed at high temperature in high vacuum *after* defined the star pattern [Fig. 5.9(f)], which would remove the surface contamination. The last process [Fig. 5.9(l)] was performed to reduce the possible side effects of the ultraviolet light irradiation (photodoping and persistent photoconductivity) and the adsorption on the  $\text{LaAlO}_3$  film surface during cleaning by chemicals. Quite recently, a strong effect of the surface charge on the conductivity at the  $\text{LaAlO}_3/\text{SrTiO}_3$  interface has been reported [111], and the surface charge might originates from surface adsorption [112].

Figure 5.10(a) shows the shape of the star-patterned sample. The pattern consists of 12 branches, aligned between  $\phi = 15^\circ$ – $345^\circ$  with  $30^\circ$  spacing ( $\phi$  denotes the angle between the step edges and the branch). Each branch has electrodes to measure the resistance along its direction. The branches at  $\phi = 255^\circ$  and  $315^\circ$  have another electrode for the Hall effect mea-

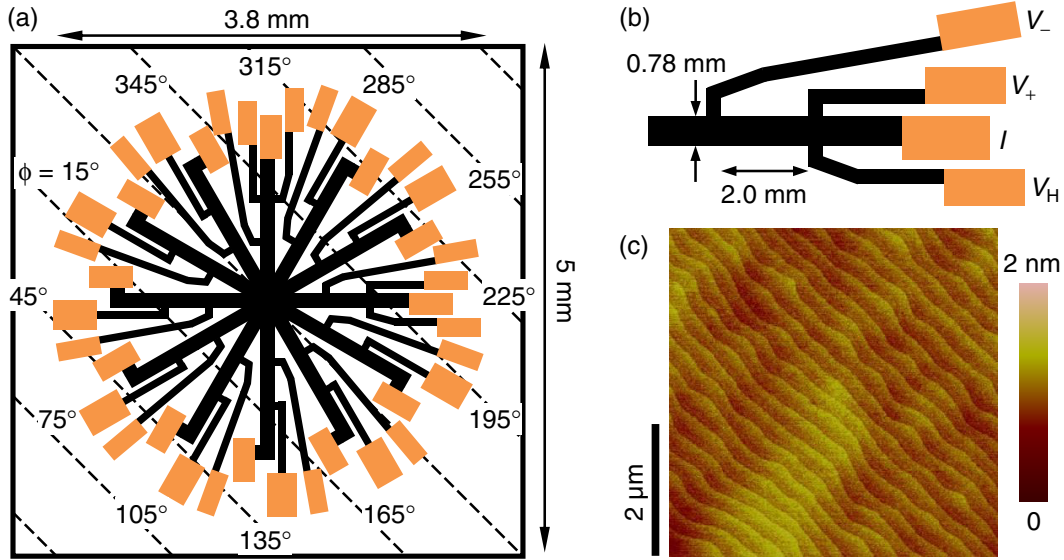


Fig. 5.10 (a) Schematic illustration of the top view of the star-patterned sample (not to scale). The outer solid line indicates the edge of the substrate. Dashed lines indicate the direction of the step edges.  $\phi$  denotes the angle between the step edges and the branch. (b) Detailed geometry of the branch of the star pattern (not to scale). (c) AFM surface topography of the  $\text{LaAlO}_3$  film measured after the whole process.

surement [Fig. 5.10(b)]. The direction of the step edges was determined by the AFM surface topography of the  $\text{LaAlO}_3$  film. As shown in Fig. 5.10(c), clear step-and-terrace structure is observed on the film surface, suggesting that the underlying interface also has this structure.

### 5.4.3 Angular dependence of the resistance

Figure 5.11(a) shows the temperature dependence of the sheet resistance of the star-patterned sample measured at various  $\phi$ . The resistance could not be measured at  $\phi = 255^\circ$  since the branch was damaged during the fabrication. No angular dependence of the resistance can be seen above 50 K. At lower temperatures some difference is observed, but it does not seem to be systematic with  $\phi$  [Fig. 5.11(b)]. The two-point  $I$ - $V$  characteristics measured at the lowest temperature reveal that the contact is strongly non-Ohmic [Fig. 5.11(c)]. The measurement errors due to this poor contact may rather be the origin of the apparent variation of the resistance with  $\phi$  at low temperatures.

The two-point  $I$ - $V$  curves measured at 100 K are linear [Fig. 5.11(d)], indicating that no angular dependence at relatively high temperatures is significant. The sheet carrier densities at 100 K measured at  $\phi = 225^\circ$  and  $315^\circ$  are  $n_s(100 \text{ K}) = 6.23 \times 10^{12} \text{ cm}^{-2}$  and  $6.04 \times 10^{12} \text{ cm}^{-2}$ , respectively. These are very close, indicating that the sample is homogeneous, and significantly lower than the typical value in the literature.

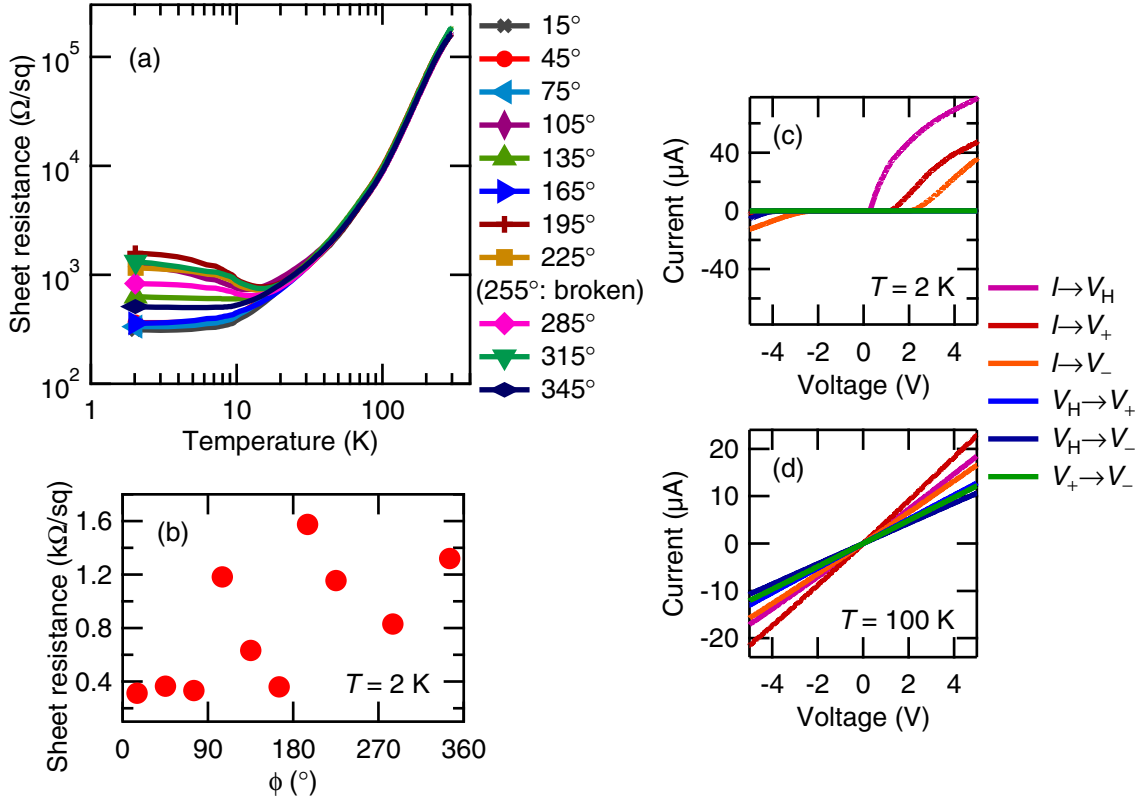


Fig. 5.11 (a) Temperature dependence of the sheet resistance measured at various  $\phi$ . (b) Sheet resistance at 2 K as a function of  $\phi$ . (c) Two-point  $I-V$  characteristics at 2 K measured at 225°. (d)  $I-V$  data for the same branch at 100 K.

#### 5.4.4 Discussion

No obvious evidence for step anisotropy was found in this study, consistent with the previous studies [106–108]. However, it would be worth further investigating the possibility of step anisotropy at the interface, since if the step anisotropy can be induced in this system by carefully tuning the growth parameters, it may also provide a novel low-dimensional electronic system. Let us discuss this issue in a bit more detail.

One possible approach is growing at other laser conditions. As discussed in Sec. 5.3.3, there are two qualitatively different types of thickness dependence of the conductivity. One is that the conductivity of the relatively thin sample is already suppressed and the variation above that thickness is relatively weak. Another is that the suppression of the conductivity becomes apparent only above 10–20  $\mu\text{c}$ . The sample examined was fabricated at the condition at which the former thickness dependence was more relevant. In the latter case, however, the underlying mechanism of the carrier density modulation can be different, and thus the highly resistive thick sample of the latter series may have a different electron distribution.

Another possible approach is to further decrease the carrier density. The carrier density of the sample examined was, although significantly lower than the typical value in the literature, still higher than the lowest one in this study by about an order of magnitude. The carrier density

can further be reduced by growing the film thicker, while the strain energy might be a trade-off, as mentioned above.

For both approaches, it is important to improve the electrical contact at low temperatures. The contact improvement is also important for further investigating the carrier density scaling (Sec. 5.3.2). Transport measurements at low temperatures are currently limited because of the poor contact to the highly resistive samples [Fig. 5.6], while the detailed temperature dependence of the carrier density and the mobility would give more insight into the carrier density modulation by the laser parameters.

## 5.5 Summary

We investigated the effects of the laser parameters on the  $\text{LaAlO}_3$  film stoichiometry and the electronic properties of the  $\text{LaAlO}_3/\text{SrTiO}_3$  interface. A significant modulation of the film stoichiometry and the lattice constant was found. The electronic properties of the  $\text{LaAlO}_3/\text{SrTiO}_3$  interface was also strongly modulated by the laser parameters. Especially, the carrier density was controlled over a wide range. While the microscopic origin of the carrier density control remains an open question, the film lattice constant was found to be a relevant parameter.

Since the mobility is low at low temperatures, an obvious next step is investigating how to enhance it. The  $\text{LaAlO}_3$  film thickness is one parameter: as reported previously [66] and confirmed in Sec. 5.3, with the thinner samples show higher mobilities. To control the carrier density and the mobility of the thinner samples, the effect of another growth parameter is investigated in the next Chapter.

## Chapter 6

# Growth Temperature Dependence of the Interface Properties

### 6.1 Introduction

Growth temperature is highly influential over the film crystallinity. For example, the crystallinity of the films grown at very low temperatures is generally poor. Low temperature growth has been utilized for buffer layers to relieve the lattice mismatch between the film and the substrate, since the dislocations required can be concentrated in the low temperature grown, lower crystalline layer [91, 113].

In Chap. 5, we demonstrated a strong impact of the laser parameters on the electronic properties of the  $\text{LaAlO}_3/\text{SrTiO}_3$  heterointerface. On the other hand, it has quite recently been reported that another growth parameter, namely the growth temperature, is also highly influential over the electronic properties of this system [114]. Motivated by this report, we have investigated the growth temperature dependence of the structural and electronic properties of the  $\text{LaAlO}_3/\text{SrTiO}_3$  heterostructure. A series of  $\text{LaAlO}_3/\text{SrTiO}_3$  heterostructures were grown at various temperatures, and the film crystallinity was characterized by XRD and AFM, as explained in Sec. 6.2. While the film crystallinity is not strongly affected, the transport properties are strongly modulated by the growth temperature. Especially, a reduced growth temperature enhances the mobility at low temperatures, which enables the observation of quantum oscillations in this system, as explained in Sec. 6.3. This may give access to two dimensional electron physics in an entirely unexplored regime.

### 6.2 Growth temperature dependence of the film crystallinity

#### 6.2.1 Details of film growth

Each sample was fabricated by PLD on a  $\text{TiO}_2$ -terminated  $\text{SrTiO}_3$  (001) substrate, as detailed in Secs. 3.1 and 4.3.3. The laser parameters used were:  $E = 39$  mJ,  $A = 3.5 \times 1.6$  mm<sup>2</sup>, and  $f = E/A = 0.7$  J/cm<sup>2</sup>. The laser repetition rate was 1 Hz. Films were grown at various growth temperatures ( $T_g$ ) in  $P_{\text{O}_2} = 1 \times 10^{-5}$  Torr. The  $\text{LaAlO}_3$  film thickness was 10 uc. Clear RHEED intensity oscillations were observed for all samples except for the one grown at  $T_g = 900$  °C.

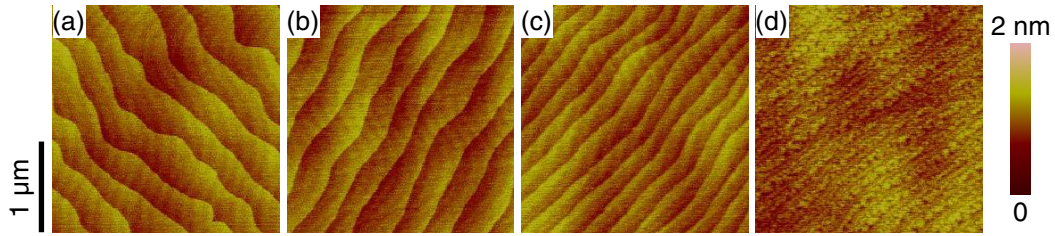


Fig. 6.1 AFM surface topography of the  $\text{LaAlO}_3$  films grown at (a)  $T_g = 600^\circ\text{C}$ , (b)  $700^\circ\text{C}$ , (c)  $800^\circ\text{C}$  and (d)  $900^\circ\text{C}$ .

The film thickness of this sample was thus calibrated assuming the same growth rate as obtained from the other film growth ( $\approx 20$  laser pulses per uc). After growth the samples were cooled to room temperature in  $P_{\text{O}_2} = 300$  Torr, with a one hour pause at  $T_{\text{sub}} = 500^\circ\text{C}$ .

## 6.2.2 AFM and XRD analysis

Figure 6.1 shows the AFM surface topography of the  $\text{LaAlO}_3$  films grown at various  $T_g$ . Except for the film grown at  $T_g = 900^\circ\text{C}$ , all samples show flat terraces with a root-mean-square roughness of  $\approx 0.1$  nm and clear 1 uc height ( $\approx 0.4$  nm) steps on the film surface. As shown in Fig. 6.1(d), the step-and-terrace structure is less clear on the film surface grown at  $T_g = 900^\circ\text{C}$ , and the terrace roughness could not be correctly measured due to the ill-defined structure. This is contrary to the general temperature dependence of the surface structure, since the higher temperature growth enhances the surface migration of the adatoms and correspondingly the surface roughness is usually reduced. These results suggest that some other factors, an enhancement of the interdiffusion due to the effective high temperature annealing [115], for example, are more relevant over the temperature range investigated.

Figure 6.2(a) shows the XRD  $\theta$ - $2\theta$  patterns of the same samples. As expected from the small film thickness of 10 uc, the diffraction from the films is weak. Still, the  $\text{LaAlO}_3$  film (002) reflections are clearly observed from all samples. The film grown at  $T_g = 900^\circ\text{C}$  shows a considerably weaker peak compared to the others. The diffraction patterns of the other samples are roughly consistent with the nominal thickness of 10 uc, although the accuracy is limited due to the weak intensity as well as the approximation used in the model.\*<sup>1</sup>

To further characterize the structure of these films, the film rocking curves were measured, as shown in Fig. 6.2(b). Some differences are observed, but they do not seem to have a strong relation with  $T_g$ , as indicated by the FWHM of the film rocking curves [Fig. 6.2(c)]. The variation of the FWHM is small (within  $\pm 0.01^\circ$ ) and not systematic with  $T_g$ . Notably, the  $\text{SrTiO}_3$  substrates show a limited, but clear variation of the crystallinity, as also shown in Fig. 6.2(c), and this correlates significantly with the variation of the  $\text{LaAlO}_3$  film FWHM.

\*<sup>1</sup> Simulation in App. A was used; see the Appendix for details.

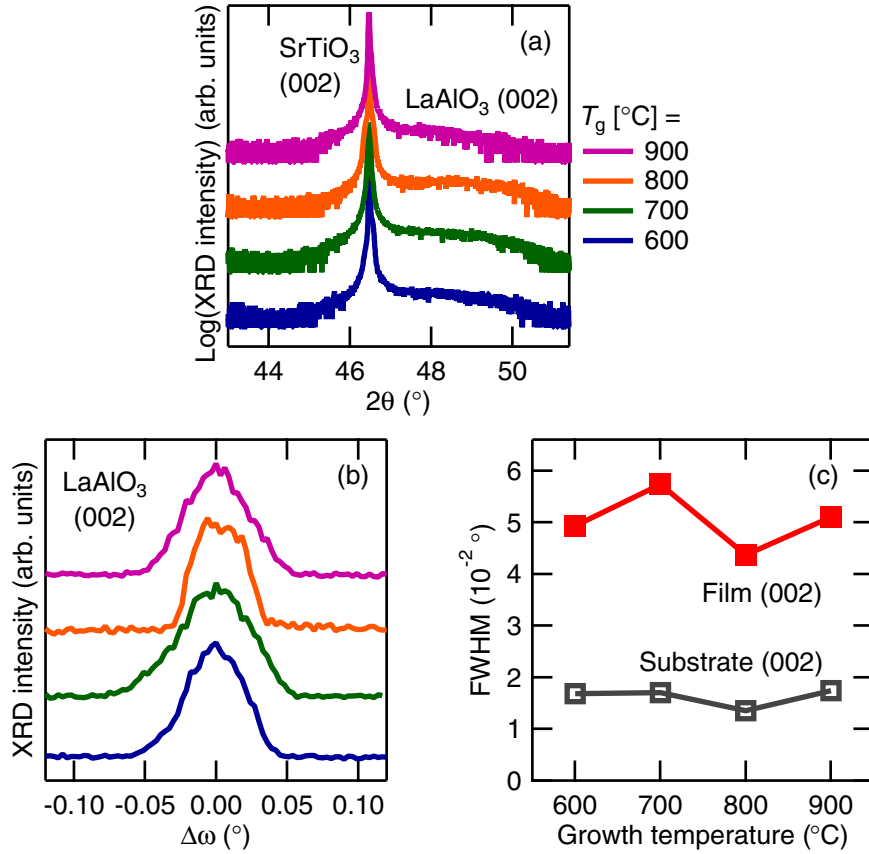


Fig. 6.2 (a) XRD  $\theta$ - $2\theta$  patterns of the LaAlO<sub>3</sub>/SrTiO<sub>3</sub> samples grown at various  $T_g$ . (b) Rocking curves of the films. (c) FWHM of the rocking curves of the LaAlO<sub>3</sub> films and the SrTiO<sub>3</sub> substrates. Lines in (c) are guides to the eye.

### 6.2.3 Discussion

These results show no obvious effect of the growth temperature on the film crystallinity over the range investigated, except at the highest temperature. This is contrary to the previous report by Caviglia *et al.* [114], who argue that the reduced growth temperature significantly improves the crystalline quality of the films. One important difference between their report and this study is the LaAlO<sub>3</sub> film thickness. Caviglia *et al.* characterized the crystalline quality of the films by analyzing relatively thick films ( $\geq 50$  uc) by RHEED and XRD (see the supplementary material of Ref. [114]). This thickness is above the reported critical thickness for the strain relaxation of 20–25 uc [103, 116], and therefore the crystalline quality can strongly depend on the details of the relaxation mechanisms.

On the other hand, the electronic properties of relatively thin LaAlO<sub>3</sub>/SrTiO<sub>3</sub> samples have been attracting more interest because of the higher mobility [66, 114], and this study has characterized the crystalline quality of such thin LaAlO<sub>3</sub> films. The thickness is below the critical thickness for the strain relaxation, and this may explain why there is no obvious variation of the film crystallinity observed in this study.

However, these results cannot fully exclude the possible effects of the growth temperature on

the film crystallinity, especially near the interface. AFM only characterizes the film surface, and the accuracy of the XRD analysis is limited due to the weak intensity as well as the variation of the substrate crystallinity. The crystallinity near the interface can be more relevant to the electronic properties of this system, since the conducting channel is not in the  $\text{LaAlO}_3$  film, but in the  $\text{SrTiO}_3$  substrate. Other experimental methods which can characterize the structural properties near the interface, for example, surface XRD, x-ray reflectivity, or STEM, would help to further investigate this issue.

## 6.3 Growth temperature dependence of the transport properties

### 6.3.1 Hall carrier density and mobility

The effect of the growth temperature on the electronic properties were also investigated using the same 10 uc  $\text{LaAlO}_3/\text{SrTiO}_3$  samples. Figure 6.3(a) shows the temperature dependence of the sheet resistance of the samples. All samples show metallic behavior down to 2 K, consistent with the previous report [66] and the results in Chap. 5, since the  $\text{LaAlO}_3$  films are thin and the laser fluence is low.

Figures 6.3(b) and (c) show the temperature dependence of the sheet carrier density and the

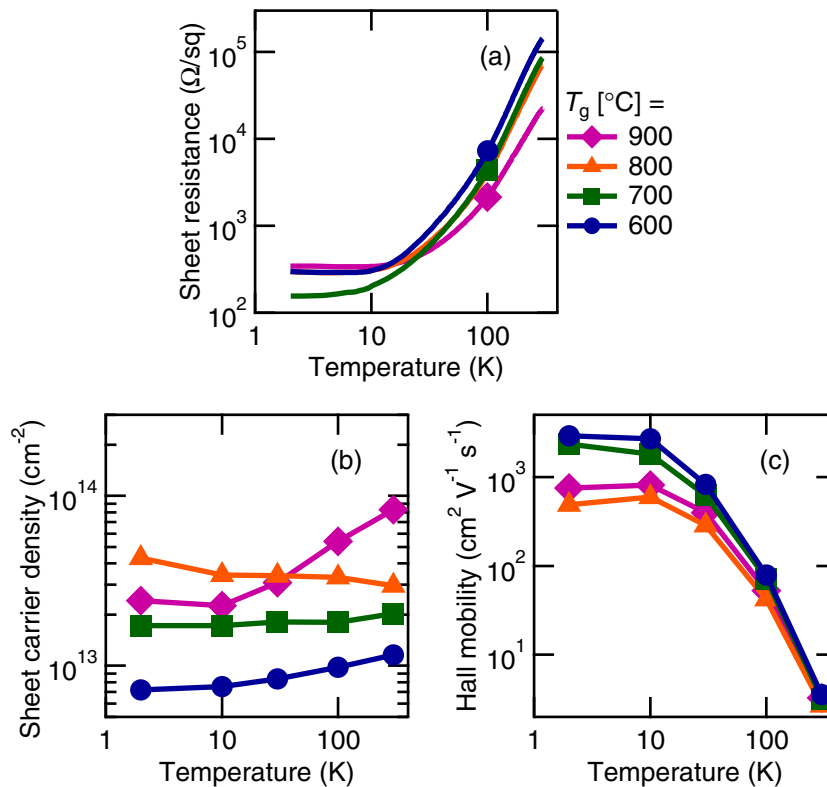


Fig. 6.3 Temperature dependence of (a) the sheet resistance, (b) the sheet carrier density and (c) the Hall mobility of the  $\text{LaAlO}_3/\text{SrTiO}_3$  samples grown at various  $T_g$ . Lines in (b) and (c) are guides to the eye.

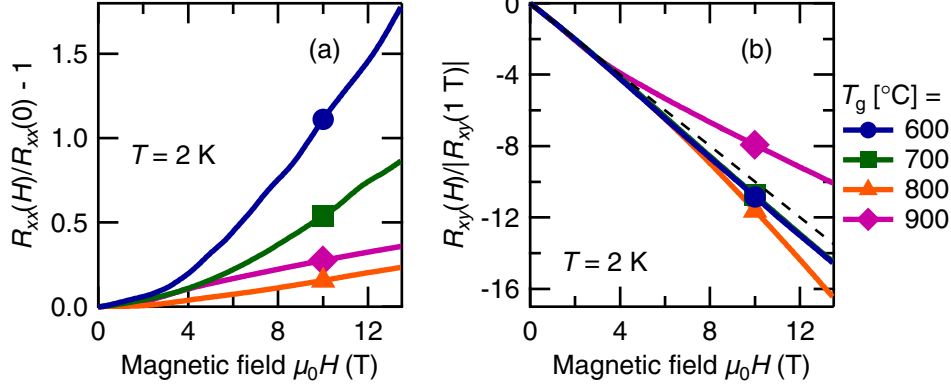


Fig. 6.4 (a) Symmetrized magnetoresistance and (b) the antisymmetrized Hall resistance of the LaAlO<sub>3</sub>/SrTiO<sub>3</sub> samples grown at various  $T_g$ . Measured at 2 K with magnetic field applied parallel to the substrate normal.

Hall mobility of the samples, respectively. The reduced growth temperature is found to decrease the carrier density and increase the mobility at low temperatures. However, the data for the sample grown at  $T_g = 800$  °C suggests a non-monotonic growth temperature dependence, since it shows a qualitatively different temperature dependence of the carrier density, that increases with decreasing temperature. While the order of the carrier density is quite different, qualitatively the same temperature dependence is reported for a highly reduced LaAlO<sub>3</sub>/SrTiO<sub>3</sub> sample (see the supplementary material of Ref. [59]).

The enhancement of the mobility at low temperatures may enable to observe quantum transport. Indeed, the mobility of the sample grown at  $T_g = 600$  °C is found to be high enough to observe the Shubnikov-de Haas oscillations at the lowest temperature. Figures 6.4(a) and (b) show the magnetoresistance and the Hall resistance of the sample at 2 K. As seen in Fig. 6.4(a), oscillatory components are observed for  $\mu_0 H > 3$  T in the magnetoresistance of the sample grown at  $T_g = 600$  °C, superimposed on a positive background. Although less visible, the sample grown at  $T_g = 700$  °C also shows oscillations of the magnetoresistance at high magnetic field. Details of the oscillations are discussed in the next Section.

As seen in Fig. 6.4(b), no indication of quantum oscillations can be found in the Hall resistance of these samples. Instead, significant nonlinearity of  $R_{xy}(H)$  is found.<sup>\*2</sup>  $|R_H(H)|$  of the sample grown at  $T_g = 900$  °C decreases with increasing  $H$ , while  $|R_H(H)|$  of the other samples increases. Assuming only electrons exist, the nonlinearity of the  $T_g = 900$  °C sample can be explained by the parallel conduction model [117], while the nonlinearity of the other samples can be explained by magnetic freeze-out [118]. This qualitative difference might originate from the enhanced interdiffusion at the highest temperature, as suggested by AFM [Fig. 6.1(d)], and consequently the different electron distribution.

<sup>\*2</sup> As explained in App. B, the carrier density and the mobility are evaluated using the low-field slope of  $R_{xy}$ .

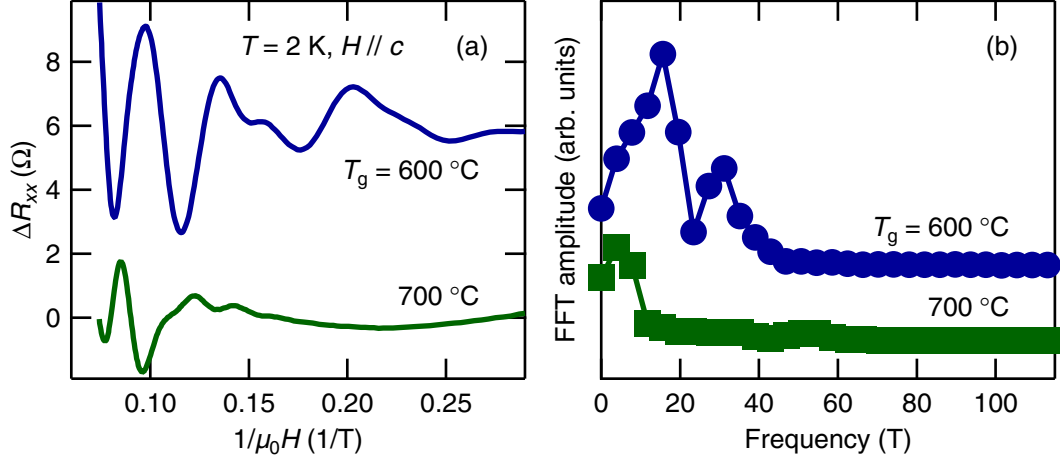


Fig. 6.5 (a) Magnetoresistance of the samples grown at  $T_g = 600\text{ °C}$  and  $700\text{ °C}$ , after background subtraction, versus reciprocal magnetic field. Measured at 2 K with magnetic field applied parallel to the substrate normal. (b) Fast Fourier transform of the data in (a).

### 6.3.2 Analysis of the Shubnikov-de Haas oscillations

The Shubnikov-de Haas oscillations of the samples grown at  $T_g = 600\text{ °C}$  and  $700\text{ °C}$  were analyzed in more detail.<sup>\*3</sup> Figure 6.5(a) shows the oscillatory components of the magnetoresistance of the samples, obtained by background subtraction using polynomial fitting, as a function of the reciprocal magnetic field. The oscillations of the  $T_g = 600\text{ °C}$  sample are confirmed to be periodic in reciprocal magnetic field, while the periodicity of the oscillations of the  $T_g = 700\text{ °C}$  sample is not clear due to the smaller amplitude and the faster damping.

The frequency of the oscillations was evaluated by the fast Fourier transform (FFT) of the data in the range  $3\text{ T} < \mu_0 H < 13.5\text{ T}$ , as shown in Fig. 6.5(b). Hanning window was used for the FFT analysis; FFT with several window functions were analyzed to examine their effect, and it was confirmed that all window function gave essentially the same frequency components.

The main components of the oscillations of the  $T_g = 600\text{ °C}$  sample are found to be  $\approx 16\text{ T}$  and  $\approx 31\text{ T}$ . These correspond to carrier densities,  $n_{\text{SDH}}$ , of  $7.7 \times 10^{11}\text{ cm}^{-2}$  and  $1.5 \times 10^{12}\text{ cm}^{-2}$ , respectively, calculated using the free carrier approximation assuming spin degeneracy. These values show significant disagreement with  $n_s(2\text{ K}) = 7.2 \times 10^{12}\text{ cm}^{-2}$  derived from the Hall measurement, by factors of  $n_s/n_{\text{SDH}} \approx 9$  (16 T) and  $\approx 5$  (31 T), respectively. Such disagreement is reported previously for a delta-doped SrTiO<sub>3</sub> heterostructure [19], as well as for the LaAlO<sub>3</sub>/SrTiO<sub>3</sub> interface [114].

In Ref. [114], a sample with  $n_s = 1.05 \times 10^{13}\text{ cm}^{-2}$  shows a main component of the oscillations of 35 T with a shoulder at 50 T, which correspond to  $n_{\text{SDH}} = 1.7 \times 10^{12}\text{ cm}^{-2}$  and  $2.4 \times 10^{12}\text{ cm}^{-2}$ , respectively. The factors  $n_s/n_{\text{SDH}} \approx 6$  (35 T) and  $\approx 4$  (50 T) are not in good agreement with this study, perhaps originating from the difference in  $n_s$ , and consequently the subband occupation. The presence of multiple valleys, and several other possible origins of

<sup>\*3</sup> The raw  $R_{xx}$  data were used for the analysis to avoid the smoothing effect in the symmetrizing process.

the disagreement between  $n_s$  and  $n_{\text{sdH}}$ , are discussed in Ref. [114]. Additional studies are necessary to elucidate this issue, including detailed band structure calculations, as pointed out in Ref. [19].

The frequency of the oscillations of the  $T_g = 700$  °C sample is not clear due to the fast damping, but is clearly much lower than  $\approx 350$  T, the expected value from  $n_s(2\text{ K}) = 1.7 \times 10^{13} \text{ cm}^{-2}$  derived from the Hall measurement. Thus this sample also shows the same order of disagreement.

### 6.3.3 Discussion

While the  $\text{LaAlO}_3$  film crystallinity was found to have no obvious relation with the growth temperature over the range investigated (except at the highest temperature; Sec. 6.2), the electronic properties of the  $\text{LaAlO}_3/\text{SrTiO}_3$  interface were strongly modulated by the growth temperature. These results are not necessarily inconsistent, since the  $\text{LaAlO}_3$  film itself is a robust insulator and therefore its crystallinity does not necessarily have an obvious direct influence on the electronic properties in the  $\text{SrTiO}_3$  substrate. However, for the same reason, it is also not clear what mechanisms control the influence of the growth temperature effects.

In Chap. 5 we discussed the importance of the laser parameters. It should be noted that the laser parameters decrease the carrier density and the mobility at the same time, while the reduced growth temperature increases the mobility with decreasing the carrier density. This suggests that the underlying mechanisms of the conductivity modulation are different. Especially, an increase of the numbers of traps, the possibility of which was discussed in Chap. 5, cannot easily explain the enhancement of the mobility by the reduced growth temperature, since the increased number of traps is likely to scatter the electrons more. It may rather be reasonable to assume that the reduced growth temperature suppresses the doping mechanism itself.

One possibility is that the reduced growth temperature suppresses the introduction of oxygen vacancies during growth. This may be thermodynamically reasonable, since the reduced growth temperature can make the thermodynamic condition more oxidizing for  $\text{SrTiO}_3$  [119]. Although the samples were postannealed, there is a possibility that the postannealing does not fully oxidize the  $\text{SrTiO}_3$  substrates, as suggested by the sample grown at  $T_g = 800$  °C. This possibility may also explain the smaller amplitude and the faster damping of the Shubnikov-de Haas oscillations of the sample grown at  $T_g = 700$  °C. If the postannealing treatment is incomplete, the carrier distribution can be inhomogeneous in plane, since the  $\text{LaAlO}_3$  film can act as a barrier for the oxygen ions and thus the center of the sample is less easily oxidized compared to the sample edges. The inhomogeneous carrier distribution would result in many frequency components in the oscillations, smearing each other.

Intermixing at the interface might also be suppressed by the reduced growth temperature. The sample grown at  $T_g = 900$  °C suggests an enhancement of the interdiffusion due to the effective high temperature annealing [115]. While no obvious dependence was found below this temperature, the interdiffusion length might still be modulated on a nanoscale near the interface. These possible chemical doping mechanisms can naturally explain the enhancement of the mobility, since there are less scattering by ionized impurities, as observed in bulk  $\text{SrTiO}_3$  [33–35].

These chemical doping pictures, however, also have problems. For example, one important parameter ignored in the discussion above is the high kinetic energy of the ablated species in PLD. The maximum kinetic energy is of the order of 10 eV or higher in high vacuum [101], much larger than the thermal energy ( $k_B T = 86$  meV at  $T = 1000$  K, where  $k_B$  is Boltzmann's constant). It should also be noted that these chemical doping pictures do not answer how the polar problem is resolved; since it is based on the very fundamental physics of this system, it must be resolved by some reconstruction, if not electronic.

Further investigation is needed to answer these open questions. One important experiment would be the examination of postannealing treatments to clarify the possible presence of residual oxygen vacancies. More detailed structural studies especially near the interface, by other methods than the XRD measured in this Chapter, should also give more insight, as mentioned in Sec. 6.2.3. Comparison with the delta-doped SrTiO<sub>3</sub> heterostructure [19] is another possibility: the delta-doped structure has no obvious interface, or broken inversion symmetry, whereas the LaAlO<sub>3</sub>/SrTiO<sub>3</sub> interface does. Thus this comparison can also be useful to answer a very fundamental question: "Is there anything unique at the interface?"

## 6.4 Summary

We investigated the effect of the growth temperature on the structural and electronic properties of the LaAlO<sub>3</sub>/SrTiO<sub>3</sub> heterostructure. While no obvious dependence of the film crystallinity was found, the carrier density was suppressed and the mobility was enhanced by reducing the growth temperature. The enhancement of the mobility enabled to observe quantum oscillations in this system. This ability to fabricate a high mobility electron gas at the LaAlO<sub>3</sub>/SrTiO<sub>3</sub> interface gives an opportunity to compare this system to the delta-doped SrTiO<sub>3</sub> heterostructure [19]. This comparison may give much insight into the electronic structure of the LaAlO<sub>3</sub>/SrTiO<sub>3</sub> interface.

At present, no indication of quantum oscillations has been found in the Hall resistance. This is presumably because the carrier density is still too high: typical carrier densities with which the quantum Hall effect is observed is  $\lesssim 10^{12}$  cm<sup>-2</sup>, often close to  $10^{11}$  cm<sup>-2</sup> [4, 18]. More careful optimization of the growth temperature (this Chapter) and the laser parameters (Chap. 5) may enable to reach such a regime. It would give access to two dimensional electron physics in an entirely unexplored regime, since this system has many characteristics that are absent in conventional semiconductors, especially notable being low carrier density superconductivity [21, 32].

# Chapter 7

## Conclusions

Complex oxide heterostructures have been attracting increasing interest because of the rich variety of physical properties displayed by them. As a natural analogue of conventional semiconductor heterostructures, high-mobility, low-density electron systems in reduced dimensions in oxide heterostructures are opening platforms for studying novel electron physics in an entirely unexplored regime. Systematic growth studies are thus becoming more and more important, since growth optimization is crucial for the film quality improvement, which directly leads to an enhancement of the mobility and therefore the possibility of novel physics.

In this Thesis, a detailed and systematic growth study of the  $\text{LaAlO}_3/\text{SrTiO}_3$  heterostructure was presented. In Chap. 4, we developed a fabrication technique of this heterostructure by engineering the interface on a nanoscale. The lattice mismatch between the  $\text{LaAlO}_3$  film and the  $\text{SrTiO}_3$  substrate was relieved by a nanometer order “ $\text{SrAlO}_x$ ” buffer layer, which enabled the evaluation of the  $\text{LaAlO}_3$  film stoichiometry using the lattice expansion. Based on this finding, in Chap. 5 we investigated the effect of the laser parameters, which is known to be highly influential over the film stoichiometry but has not been discussed in the literature for the  $\text{LaAlO}_3/\text{SrTiO}_3$  heterostructure. By controlling the laser parameters, the  $\text{LaAlO}_3$  film stoichiometry and the electronic properties of the  $\text{LaAlO}_3/\text{SrTiO}_3$  interface was strongly modulated. Especially, the carrier density was controlled over a wide range, and the film lattice constant was found to be the relevant parameter. Combined with the optimization of the growth temperature, as detailed in Chap. 6, we realized a high-mobility, low-density electron system at the interface, which showed quantum oscillations at low temperatures.

For further enhancing the mobility and reducing the carrier density, more careful optimization of the growth parameters are required, based on a better understanding on the origin of the conductivity at the  $\text{LaAlO}_3/\text{SrTiO}_3$  heterointerface. While this study cannot give a full and direct answer for the doping mechanism, an important basis was presented to further investigate this issue. As briefly reviewed in Chap. 2, a central difficulty in achieving consensus about this system is the variation in growth parameters used by various groups, leading to a wide range of reported properties. It is thus often misleading to generalize a particular property of a particular sample, or to compare results from different laboratories. A systematic understanding on the effects of growth parameters is essential to overcome this difficulty, to which this study made a significant contribution.

As mentioned in Chap 6, we are approaching two dimensional electron physics in an entirely unexplored regime. Since this system shows low carrier density superconductivity, it may be

possible to observe the quantum Hall effect *and* superconductivity, and to study the interplay between them. This would be a representative example of novel electron physics that are not accessible in conventional semiconductor heterostructures. We hope the results obtained in this study will play an important role as a basis for the study of complex oxide heterostructures.

## Appendix A

# Simulation of XRD $\theta$ – $2\theta$ Patterns

In this Appendix, the validity of the approximation implicitly used in Sec. 3.2 is examined: namely, that the film and the substrate can be treated as independent single crystals. Mathematically, this approximation is reflected as follows. We described the XRD intensity as

$$\begin{aligned} I(\mathbf{k}) &= I_e \left| \int_{\text{matter}} \rho(\mathbf{r}) e^{i(\mathbf{k}-\mathbf{k}_0)\cdot\mathbf{r}} d^3\mathbf{r} \right|^2 \\ &= I_e \left| \sum_{l,m,n} e^{i\Delta\mathbf{k}\cdot(l\mathbf{a}+m\mathbf{b}+n\mathbf{c})} \int_{\text{unit cell}} \rho(\mathbf{r}') e^{i\Delta\mathbf{k}\cdot\mathbf{r}'} d^3\mathbf{r}' \right|^2 = I_e |G(\mathbf{k})|^2 |F(\mathbf{k})|^2, \end{aligned} \quad (\text{A.1})$$

which is valid only when the *whole* structure has the same periodicity of  $\rho(\mathbf{r})$ . However, this is not the case of the  $\text{LaAlO}_3/\text{SrTiO}_3$  heterostructure.

For simplicity, let us consider the one-dimensional XRD pattern normal to the sample surface, namely, the  $\theta$ – $2\theta$  measurement. Since the film and the substrate *locally* has a periodicity of  $\rho(\mathbf{r})$ , the XRD intensity can be described as

$$\begin{aligned} I(2\theta) &= I_e \left| F_f \sum_{n=0}^{N-1} e^{i\phi_f n} + F_s e^{i\phi_f(N-1)} \sum_{m=0}^{M-1} e^{i\phi_s m} \right|^2 \\ &= I_e \left| F_f G_f + F_s e^{i\phi_f(N-1)} G_s \right|^2, \end{aligned} \quad (\text{A.2})$$

where  $F_f$  is the crystal structure factor of the film,  $F_s$  that of the substrate,  $N$  is the number of unit cells of the film,  $M$  that of the substrate,

$$\phi_f \equiv c_f \cdot \Delta k = c_f \cdot 2 \frac{2\pi}{\lambda} \sin \theta, \quad \phi_s \equiv c_s \cdot \Delta k = c_s \cdot 2 \frac{2\pi}{\lambda} \sin \theta, \quad (\text{A.3})$$

( $c_f$ ,  $c_s$  are the out-of-plane lattice constants of the film and the substrate, respectively) and

$$G_f \equiv \sum_{n=0}^{N-1} e^{i\phi_f n}, \quad G_s \equiv \sum_{m=0}^{M-1} e^{i\phi_s m}. \quad (\text{A.4})$$

Let us consider the simplest model of the crystal structure factors:  $F_f = F_s \equiv F$ . This would not be a very good approximation,<sup>\*1</sup> but should not change the qualitative conclusions. Then

---

<sup>\*1</sup> Because the atomic numbers (electron densities) of Sr and La, Ti and Al atoms are quite different; see the definition of the crystal structure factor (Eq. 3.3).

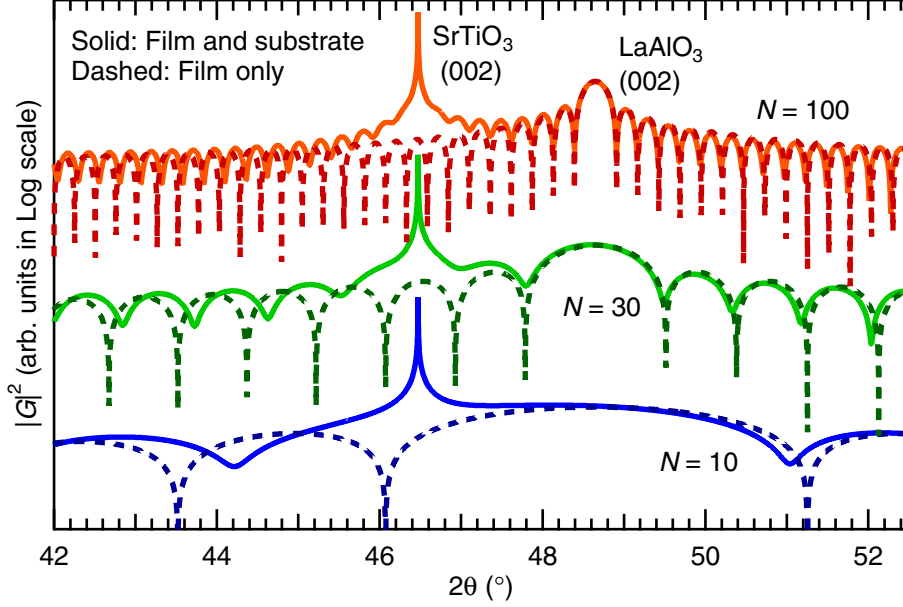


Fig. A.1 Numerical calculation results of  $|G|^2$ .

the approximation used in Sec. 3.2 can be described as

$$I = I_e |F|^2 |G_f + e^{i\phi_f(N-1)} G_s|^2 \approx I_e |F|^2 |G_f|^2 + I_e |F|^2 |G_s|^2. \quad (\text{A.5})$$

Figure A.1 shows the numerical calculation results of

$$|G_f + e^{i\phi_f(N-1)} G_s|^2 = \left| \frac{1 - e^{i\phi_f N}}{1 - e^{i\phi_f}} + \frac{e^{i\phi_f(N-1)} (1 - e^{i\phi_s M})}{1 - e^{i\phi_s}} \right|^2 \approx \left| \frac{1 - e^{i\phi_f N}}{1 - e^{i\phi_f}} + \frac{e^{i\phi_f(N-1)}}{1 - e^{i\phi_s}} \right|^2, \quad (\text{A.6})$$

and

$$|G_f|^2 = \frac{\sin^2(\phi_f N/2)}{\sin^2(\phi_f/2)}, \quad (\text{A.7})$$

with  $c_f = 3.74 \text{ \AA}$ ,  $c_s = 3.905 \text{ \AA}$ ,  $\lambda = 1.54056 \text{ \AA}$ , and various  $N$  values. Here  $e^{i\phi_s M}$  is neglected since  $M$  is large.\*<sup>2</sup> For the same reason  $|G_s|^2$  is treated as a delta function.

As seen in the figure, when  $N = 100$ , Eqs. A.6 and A.7 give very similar patterns to each other, especially near the film (002) peak. This means that the interference between the film and the substrate is negligible when the film is thick. By contrast, when  $N = 10$ , Eqs. A.6 and A.7 show nontrivial disagreement. Most notable is that the film (002) peak is not well-defined when simulated by Eq. A.6. Thus the interference between the film and the substrate should not be neglected when the film is thin.

At the intermediate thickness of  $N = 30$ , Eqs. A.6 and A.7 show small, but significant differences with each other. The film (002) peaks are very clear in the both patterns and nearly identical, while the difference of the fringe peaks is not so trivial. Therefore, the interference

\*<sup>2</sup> Mathematically this is not valid since the exponent is a pure imaginary number. Physically this term can hardly be observed since it oscillates too fast with  $\theta$ .

between the film and the substrate should be taken into account for the detailed analysis of the diffraction pattern; for thickness calibrations (Eqs. 3.11 and 3.12), for example. However, as for the calibration of the out-of-plane lattice constant (Eq. 3.9), where only the main peak position is relevant, the approximation used in Sec. 3.2 is still reasonable.

## Appendix B

# Data Treatment for Hall Effect and Magnetoresistance Measurements

As explained in Sec. 3.3, a standard Hall bar geometry was used throughout this thesis. However, there was a practical problem that  $R_{xx}$  and  $R_{xy}$  cannot be measured independently due to the inevitable misalignment of the electrodes, as schematically shown in Fig. B.1. Therefore, in order to extract  $R_{xx}$  and  $R_{xy}$  independently, the raw data of the Hall effect and the magnetoresistance measurements were treated as follows (unless otherwise indicated).

Assuming  $R_{xx}(B)$  is an even function and  $R_{xy}(B)$  is an odd function ( $B = \mu_0 H$  is the magnetic flux density), we can extract  $R_{xx}(B)$  ( $R_{xy}(B)$ ) by symmetrizing (antisymmetrizing) the raw data:

$$R_{xx}(B) = \frac{R_{xx}^{(\text{raw})}(B) + R_{xx}^{(\text{raw})}(-B)}{2}, \quad (\text{B.1})$$

$$R_{xy}(B) = \frac{R_{xy}^{(\text{raw})}(B) - R_{xy}^{(\text{raw})}(-B)}{2}. \quad (\text{B.2})$$

In this calculation, however, we have the second practical problem that the raw data are not perfectly spaced in magnetic field. For example, the raw data available are often like  $R_{xx}^{(\text{raw})}(B = 7.98 \text{ T})$  and  $R_{xx}^{(\text{raw})}(B = -8.01 \text{ T})$ , with which we cannot derive  $R_{xx}(B = 8.00 \text{ T})$ . In order to solve this problem, a set of equally-spaced data was derived by linear-interpolation of the raw data, as shown in Fig. B.2(b). It was always confirmed that the interpolated data [Fig. B.2(c)] have no significant difference from the raw data [Fig. B.2(a)], and then the interpolated data  $R_{xx}^{(\text{int})}(B)$  and  $R_{xy}^{(\text{int})}(B)$  were substituted in Eqs. B.1 and B.2 instead of the raw data to extract  $R_{xx}(B)$  and  $R_{xy}(B)$  [Fig. B.2(d)].

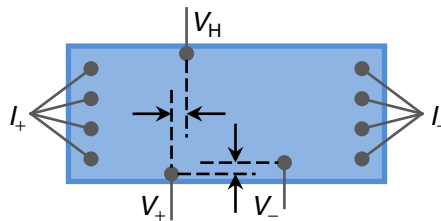


Fig. B.1 Schematic illustration of the practical geometry of electrodes.

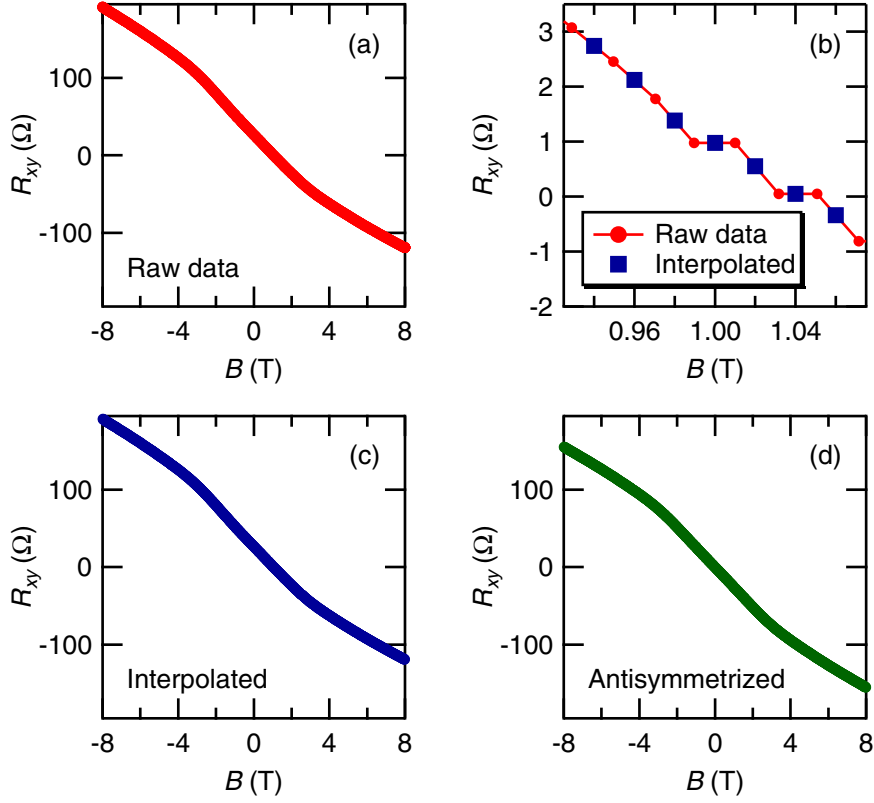


Fig. B.2 (a) A set of raw  $R_{xy}$  data. (b) The scheme of linear interpolation to derive a set of equally-spaced data. (c) Interpolated  $R_{xy}$  data. (d) Antisymmetrized  $R_{xy}$  data derived using Eq. B.2.

The sheet carrier density  $n_s$  and the Hall mobility  $\mu_H$  are derived by

$$n_s = -\frac{1}{eR_H}, \quad (\text{B.3})$$

$$\mu_H = \frac{1}{en_s\rho_s} = -\frac{R_H}{\rho_s}, \quad (\text{B.4})$$

where

$$R_H \equiv \frac{dR_{xy}(B)}{dB} \quad (\text{B.5})$$

is the Hall coefficient and  $\rho_s$  is the sheet resistance. As seen in Fig. B.2(d), the Hall resistance  $R_{xy}(B)$  is sometimes nonlinear with the magnetic field in the systems investigated, and therefore the Hall coefficient defined here is a function of magnetic field. Throughout this thesis,  $R_H$  was calculated by linear-fitting of the antisymmetrized data between 0–1 T.

## Appendix C

# Control of $\text{LaAlO}_3/\text{SrTiO}_3$ (001) Interfaces Using “ $\text{SrAlO}_x$ ”

In this Appendix the possibility of termination control of  $\text{LaAlO}_3/\text{SrTiO}_3$  (001) interfaces using “ $\text{SrAlO}_x$ ” is investigated. In Chap. 4, the growth of  $\text{SrAlO}_x$  interlayers between  $\text{SrTiO}_3$  and  $\text{LaAlO}_3$  has been demonstrated, a material that is not a perovskite, nor stable as a single phase in bulk. While it is shown that at the 3 uc critical thickness the  $\text{SrAlO}_x$  interlayer acts as a sliding buffer layer for the  $\text{LaAlO}_3$  layer, it is also of interest that 1 uc of  $\text{SrAlO}_x$  can maintain epitaxy. As explained in Sec. 4.3.1, this may enable termination control of  $\text{LaAlO}_3/\text{SrTiO}_3$  (001) interfaces in superlattices.

To investigate this possibility, cation off-stoichiometry in  $\text{SrTiO}_3$  films can be a problem, since the cation vacancies in  $n$ -doped  $\text{SrTiO}_3$  films can trap and scatter the electrons, resulting in highly resistive films [81, 82]. Therefore, to see the asymmetry of the two types of interfaces between  $\text{LaAlO}_3$  and  $\text{SrTiO}_3$  films by their transport properties [14, 48], the effect of the cation off-stoichiometry in the  $\text{SrTiO}_3$  film should be minimized.\*<sup>1</sup>

Thus we first optimized the growth conditions for  $\text{SrTiO}_3$ . The net cation off-stoichiometry

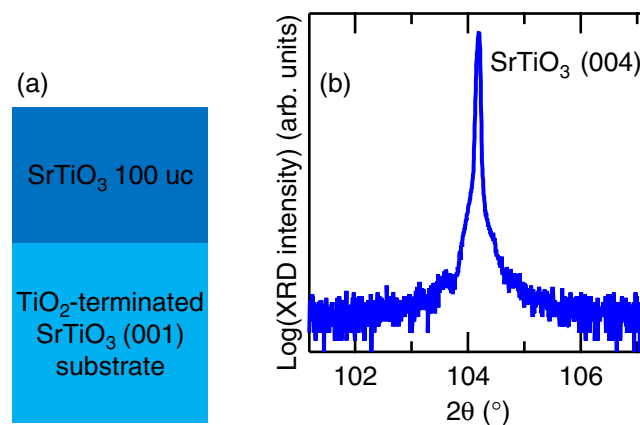


Fig. C.1 (a) Schematic illustration of the  $\text{SrTiO}_3$  homoepitaxial sample and (b) XRD  $\theta$ - $2\theta$  pattern.

\*<sup>1</sup> Another possibility might be depositing  $\text{SrAlO}_x$  and  $\text{LaAlO}_3$  directly on the  $\text{SrTiO}_3$  substrates, while it would be less useful for the future purpose of superlattice fabrication.

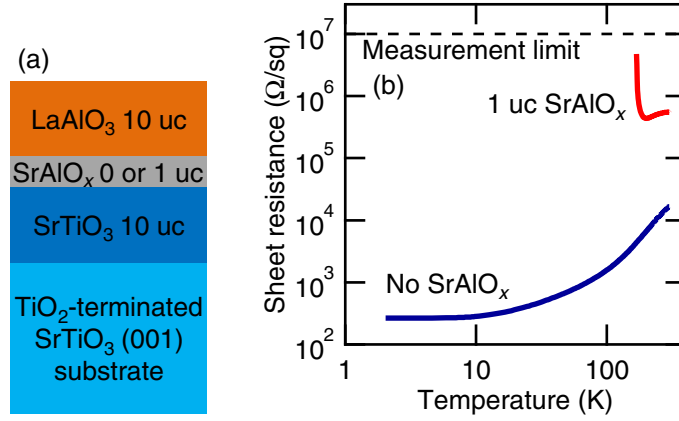


Fig. C.2 (a) Schematic illustration of the sample structure and (b) temperature dependence of the resistance of the two samples with and without an interlayer.

was evaluated by the lattice expansion of homoepitaxial films [Fig. C.1(a)], as used in Refs. [81, 82]. Figure C.1(b) shows the XRD  $\theta$ - $2\theta$  pattern of the homoepitaxial sample grown under the optimized conditions:  $T_{\text{sub}} = 800$  °C,  $P_{\text{O}_2} = 1 \times 10^{-5}$  Torr,  $A = 3.0$  mm<sup>2</sup>,  $f = 0.7$  J/cm<sup>2</sup>. The substrate and the film (004) peaks are indistinguishable, indicating that the film lattice expansion, or cation off-stoichiometry, is negligible.

Having found the optimized growth conditions for SrTiO<sub>3</sub>, we investigated the possibility of termination control of LaAlO<sub>3</sub>/SrTiO<sub>3</sub> (001) interfaces. Figure C.2(a) shows the sample structure. It should be noted that the thickness of the LaAlO<sub>3</sub> layer is relatively thin (10 uc) compared to that in Chap. 4 (100 uc). The thin LaAlO<sub>3</sub> is more useful here since the conductivity is enhanced at the *n*-type interface [66], while the thick LaAlO<sub>3</sub> was more useful for XRD measurements. Each sample was grown in the same conditions discussed previously, on a  $5 \times 5$  mm<sup>2</sup> SrTiO<sub>3</sub> (001) substrate with a TiO<sub>2</sub>-terminated surface [94, 95]. Before growth the substrates were preannealed at  $T_{\text{sub}} = 950$  °C in  $P_{\text{O}_2} = 5 \times 10^{-6}$  Torr for 30 mins. The thickness of each layer was monitored *in situ* using RHEED. After the LaAlO<sub>3</sub> growth, the samples were cooled to room temperature in  $P_{\text{O}_2} = 300$  Torr, with a one hour pause at  $T_{\text{sub}} = 600$  °C.

Figure C.2(b) shows the temperature dependence of the resistance of the samples with and without 1 uc SrAlO<sub>x</sub>. The sample without SrAlO<sub>x</sub> shows metallic behavior down to 2 K, while the sample with 1 uc SrAlO<sub>x</sub> is highly resistive and insulating at low temperatures. This asymmetry in transport properties is qualitatively the same as the previous reports using SrO [14, 48], implying the successful termination control using SrAlO<sub>x</sub>. The slight conductivity of the *p*-type sample at high temperatures may be due to the photoconductivity and/or the incomplete coverage of SrAlO<sub>x</sub>.

# References

- [1] N. W. Ashcroft and N. D. Mermin, *Solid State Physics* (Thomson Learning, Inc., 1976).
- [2] S. M. Sze, *Physics of Semiconductor Devices* (John Wiley & Sons, Inc., 1981), 2nd ed.
- [3] K. v. Klitzing, G. Dorda, and M. Pepper, New method for high-accuracy determination of the fine-structure constant based on quantized Hall resistance, *Phys. Rev. Lett.* **45**, 494 (1980).
- [4] D. C. Tsui, H. L. Stormer, and A. C. Gossard, Two-dimensional magnetotransport in the extreme quantum limit, *Phys. Rev. Lett.* **48**, 1559 (1982).
- [5] T. Ando, A. B. Fowler, and F. Stern, Electronic properties of two-dimensional systems, *Rev. Mod. Phys.* **54**, 437 (1982).
- [6] E. Abrahams, S. V. Kravchenko, and M. P. Sarachik, Metallic behavior and related phenomena in two dimensions, *Rev. Mod. Phys.* **73**, 251 (2001).
- [7] M. Imada, A. Fujimori, and Y. Tokura, Metal-insulator transitions, *Rev. Mod. Phys.* **70**, 1039 (1998).
- [8] J. G. Bednorz and K. A. Müller, Possible high  $T_c$  superconductivity in the Ba–La–Cu–O system, *Z. Phys. B* **64**, 189 (1986).
- [9] A. Urushibara, Y. Moritomo, T. Arima, A. Asamitsu, G. Kido, and Y. Tokura, Insulator-metal transition and giant magnetoresistance in  $\text{La}_{1-x}\text{Sr}_x\text{MnO}_3$ , *Phys. Rev. B* **51**, 14103 (1995).
- [10] S. Jin, T. H. Tiefel, M. McCormack, R. A. Fastnacht, R. Ramesh, and L. H. Chen, Thousandfold change in resistivity in magnetoresistive La–Ca–Mn–O films, *Science* **264**, 413 (1994).
- [11] S. Jin, T. H. Tiefel, M. McCormack, H. M. O’Bryan, L. H. Chen, R. Ramesh, and D. Schurig, Thickness dependence of magnetoresistance in La–Ca–Mn–O epitaxial films, *Appl. Phys. Lett.* **67**, 557 (1995).
- [12] A. Ohtomo, D. A. Muller, J. L. Grazul, and H. Y. Hwang, Artificial charge-modulation in atomic-scale perovskite titanate superlattices, *Nature* **419**, 378 (2002).
- [13] S. Okamoto and A. J. Millis, Electronic reconstruction at an interface between a Mott insulator and a band insulator, *Nature* **428**, 630 (2004).
- [14] A. Ohtomo and H. Y. Hwang, A high-mobility electron gas at the  $\text{LaAlO}_3/\text{SrTiO}_3$  heterointerface, *Nature* **427**, 423 (2004).
- [15] N. Nakagawa, H. Y. Hwang, and D. A. Muller, Why some interfaces cannot be sharp, *Nature Mater.* **5**, 204 (2006).
- [16] A. Tsukazaki, A. Ohtomo, and M. Kawasaki, High-mobility electronic transport in ZnO thin films, *Appl. Phys. Lett.* **88**, 152106 (2006).
- [17] Y. Kozuka, Y. Hikita, C. Bell, and H. Y. Hwang, Dramatic mobility enhancements in

- doped SrTiO<sub>3</sub> thin films by defect management, *Appl. Phys. Lett.* **97**, 012107 (2010).
- [18] A. Tsukazaki, A. Ohtomo, T. Kita, Y. Ohno, H. Ohno, and M. Kawasaki, Quantum Hall effect in polar oxide heterostructures, *Science* **315**, 1388 (2007).
- [19] Y. Kozuka, M. Kim, C. Bell, B. G. Kim, Y. Hikita, and H. Y. Hwang, Two-dimensional normal-state quantum oscillations in a superconducting heterostructure, *Nature* **462**, 487 (2009).
- [20] R. Dingle, H. L. Störmer, A. C. Gossard, and W. Wiegmann, Electron mobilities in modulation-doped semiconductor heterojunction superlattices, *Appl. Phys. Lett.* **33**, 665 (1978).
- [21] N. Reyren, S. Thiel, A. D. Caviglia, L. Fitting Kourkoutis, G. Hammerl, C. Richter, C. W. Schneider, T. Kopp, A.-S. Rüetschi, D. Jaccard, M. Gabay, D. A. Muller, J.-M. Triscone, and J. Mannhart, Superconducting interfaces between insulating oxides, *Science* **317**, 1196 (2007).
- [22] S. Thiel, G. Hammerl, A. Schmehl, C. W. Schneider, and J. Mannhart, Tunable quasi-two-dimensional electron gases in oxide heterostructures, *Science* **313**, 1942 (2006).
- [23] A. D. Caviglia, S. Gariglio, N. Reyren, D. Jaccard, T. Schneider, M. Gabay, S. Thiel, G. Hammerl, J. Mannhart, and J.-M. Triscone, Electric field control of the LaAlO<sub>3</sub>/SrTiO<sub>3</sub> interface ground state, *Nature* **456**, 624 (2008).
- [24] K. A. Müller, W. Berlinger, and F. Waldner, Characteristic structural phase transition in perovskite-type compounds, *Phys. Rev. Lett.* **21**, 814 (1968).
- [25] G. Shirane and Y. Yamada, Lattice-dynamical study of the 110°K phase transition in SrTiO<sub>3</sub>, *Phys. Rev.* **177**, 858 (1969).
- [26] J. A. Noland, Optical absorption of single-crystal strontium titanate, *Phys. Rev.* **94**, 724 (1954).
- [27] M. Capizzi and A. Frova, Optical gap of strontium titanate (deviation from Urbach tail behavior), *Phys. Rev. Lett.* **25**, 1298 (1970).
- [28] A. H. Kahn and A. J. Leyendecker, Electronic energy bands in strontium titanate, *Phys. Rev.* **135**, A1321 (1964).
- [29] J. F. Schooley, W. R. Hosler, and M. L. Cohen, Superconductivity in semiconducting SrTiO<sub>3</sub>, *Phys. Rev. Lett.* **12**, 474 (1964).
- [30] J. F. Schooley, W. R. Hosler, E. Ambler, J. H. Becker, M. L. Cohen, and C. S. Koonce, Dependence of the superconducting transition temperature on carrier concentration in semiconducting SrTiO<sub>3</sub>, *Phys. Rev. Lett.* **14**, 305 (1965).
- [31] E. Ambler, J. H. Colwell, W. R. Hosler, and J. F. Schooley, Magnetization and critical fields of superconducting SrTiO<sub>3</sub>, *Phys. Rev.* **148**, 280 (1966).
- [32] C. S. Koonce, M. L. Cohen, J. F. Schooley, W. R. Hosler, and E. R. Pfeiffer, Superconducting transition temperatures of semiconducting SrTiO<sub>3</sub>, *Phys. Rev.* **163**, 380 (1967).
- [33] H. P. R. Frederikse, W. R. Thurber, and W. R. Hosler, Electronic transport in strontium titanate, *Phys. Rev.* **134**, A442 (1964).
- [34] O. N. Tufte and P. W. Chapman, Electron mobility in semiconducting strontium titanate, *Phys. Rev.* **155**, 796 (1967).
- [35] C. Lee, J. Yahia, and J. L. Brebner, Electronic conduction in slightly reduced strontium titanate at low temperatures, *Phys. Rev. B* **3**, 2525 (1971).

- [36] T. Sakudo and H. Unoki, Dielectric properties of SrTiO<sub>3</sub> at low temperatures, *Phys. Rev. Lett.* **26**, 851 (1971).
- [37] K. A. Müller and H. Burkard, SrTiO<sub>3</sub>: An intrinsic quantum paraelectric below 4 K, *Phys. Rev. B* **19**, 3593 (1979).
- [38] H.-M. Christen, J. Mannhart, E. J. Williams, and C. Gerber, Dielectric properties of sputtered SrTiO<sub>3</sub> films, *Phys. Rev. B* **49**, 12095 (1994).
- [39] J. G. Bednorz and K. A. Müller, Sr<sub>1-x</sub>Ca<sub>x</sub>TiO<sub>3</sub>: An XY quantum ferroelectric with transition to randomness, *Phys. Rev. Lett.* **52**, 2289 (1984).
- [40] M. Itoh, R. Wang, Y. Inaguma, T. Yamaguchi, Y.-J. Shan, and T. Nakamura, Ferroelectricity induced by oxygen isotope exchange in strontium titanate perovskite, *Phys. Rev. Lett.* **82**, 3540 (1999).
- [41] H. Uwe and T. Sakudo, Stress-induced ferroelectricity and soft phonon modes in SrTiO<sub>3</sub>, *Phys. Rev. B* **13**, 271 (1976).
- [42] J. H. Haeni, P. Irvin, W. Chang, R. Uecker, P. Reiche, Y. L. Li, S. Choudhury, W. Tian, M. E. Hawley, B. Craigo, A. K. Tagantsev, X. Q. Pan, S. K. Streiffer, L. Q. Chen, S. W. Kirchoefer, J. Levy, and D. G. Schlom, Room-temperature ferroelectricity in strained SrTiO<sub>3</sub>, *Nature* **430**, 758 (2004).
- [43] S. Geller and V. B. Bala, Crystallographic studies of perovskite-like compounds. II. Rare earth aluminates, *Acta Cryst.* **9**, 1019 (1956).
- [44] S. A. Hayward, F. D. Morrison, S. A. T. Redfern, E. K. H. Salje, J. F. Scott, K. S. Knight, S. Tarantino, A. M. Glazer, V. Shuvaeva, P. Daniel, M. Zhang, and M. A. Carpenter, Transformation processes in LaAlO<sub>3</sub>: Neutron diffraction, dielectric, thermal, optical, and Raman studies, *Phys. Rev. B* **72**, 054110 (2005).
- [45] G. W. Berkstresser, A. J. Valentino, and C. D. Brandle, Growth of single crystals of lanthanum aluminate, *J. Cryst. Growth* **109**, 457 (1991).
- [46] S.-G. Lim, S. Kriventsov, T. N. Jackson, J. H. Haeni, D. G. Schlom, A. M. Balbashov, R. Uecker, P. Reiche, J. L. Freeouf, and G. Lucovsky, Dielectric functions and optical bandgaps of high-*K* dielectrics for metal-oxide-semiconductor field-effect transistors by far ultraviolet spectroscopic ellipsometry, *J. Appl. Phys.* **91**, 4500 (2002).
- [47] J. Krupka, R. G. Geyer, M. Kuhn, and J. H. Hinken, Dielectric properties of single crystals of Al<sub>2</sub>O<sub>3</sub>, LaAlO<sub>3</sub>, NdGaO<sub>3</sub>, SrTiO<sub>3</sub>, and MgO at cryogenic temperatures, *IEEE Trans. Microwave Theory Tech.* **42**, 1886 (1994).
- [48] J. Nishimura, A. Ohtomo, A. Ohkubo, Y. Murakami, and M. Kawasaki, Controlled carrier generation at a polarity-discontinued perovskite heterointerface, *Jpn. J. Appl. Phys.* **43**, L1032 (2004).
- [49] G. A. Baraff, J. A. Appelbaum, and D. R. Hamann, Self-consistent calculation of the electronic structure at an abrupt GaAs-Ge interface, *Phys. Rev. Lett.* **38**, 237 (1977).
- [50] W. A. Harrison, E. A. Kraut, J. R. Waldrop, and R. W. Grant, Polar heterojunction interfaces, *Phys. Rev. B* **18**, 4402 (1978).
- [51] A. Kalabukhov, R. Gunnarsson, J. Börjesson, E. Olsson, T. Claeson, and D. Winkler, Effect of oxygen vacancies in the SrTiO<sub>3</sub> substrate on the electrical properties of the LaAlO<sub>3</sub>/SrTiO<sub>3</sub> interface, *Phys. Rev. B* **75**, 121404 (2007).
- [52] W. Siemons, G. Koster, H. Yamamoto, W. A. Harrison, G. Lucovsky, T. H. Geballe,

- D. H. A. Blank, and M. R. Beasley, Origin of charge density at LaAlO<sub>3</sub> on SrTiO<sub>3</sub> heterointerfaces: Possibility of intrinsic doping, *Phys. Rev. Lett.* **98**, 196802 (2007).
- [53] G. Herranz, M. Basletic, M. Bibes, C. Carrétéro, E. Tafrá, E. Jacquet, K. Bouzouane, C. Deranlot, A. Hamzić, J.-M. Broto, A. Barthélémy, and A. Fert, High mobility in LaAlO<sub>3</sub>/SrTiO<sub>3</sub> heterostructures: Origin, dimensionality, and perspectives, *Phys. Rev. Lett.* **98**, 216803 (2007).
- [54] P. R. Willmott, S. A. Pauli, R. Herger, C. M. Schlepütz, D. Martoccia, B. D. Patterson, B. Delley, R. Clarke, D. Kumah, C. Cionca, and Y. Yacoby, Structural basis for the conducting interface between LaAlO<sub>3</sub> and SrTiO<sub>3</sub>, *Phys. Rev. Lett.* **99**, 155502 (2007).
- [55] A. S. Kalabukhov, Y. A. Boikov, I. T. Serenkov, V. I. Sakharov, V. N. Popok, R. Gunnarsson, J. Börjesson, N. Ljustina, E. Olsson, D. Winkler, and T. Claeson, Cationic disorder and phase segregation in LaAlO<sub>3</sub>/SrTiO<sub>3</sub> heterointerfaces evidenced by medium-energy ion spectroscopy, *Phys. Rev. Lett.* **103**, 146101 (2009).
- [56] L. Qiao, T. C. Droubay, V. Shutthanandan, Z. Zhu, P. V. Sushko, and S. A. Chambers, Thermodynamic instability at the stoichiometric LaAlO<sub>3</sub>/SrTiO<sub>3</sub>(001) interface, *J. Phys.: Condens. Matter* **22**, 312201 (2010).
- [57] S. A. Chambers, M. H. Engelhard, V. Shutthanandan, Z. Zhu, T. C. Droubay, L. Qiao, P. V. Sushko, T. Feng, H. D. Lee, T. Gustafsson, E. Garfunkel, A. B. Shah, J.-M. Zuo, and Q. M. Ramasse, Instability, intermixing and electronic structure at the epitaxial LaAlO<sub>3</sub>/SrTiO<sub>3</sub>(001) heterojunction, *Surf. Sci. Rep.* **65**, 317 (2010).
- [58] C. H. Ahn, J.-M. Triscone, and J. Mannhart, Electric field effect in correlated oxide systems, *Nature* **424**, 1015 (2003).
- [59] A. Brinkman, M. Huijben, M. van Zalk, J. Huijben, U. Zeitler, J. C. Maan, W. G. van der Wiel, G. Rijnders, D. H. A. Blank, and H. Hilgenkamp, Magnetic effects at the interface between non-magnetic oxides, *Nature Mater.* **6**, 493 (2007).
- [60] C. Cancellieri, N. Reyren, S. Gariglio, A. D. Caviglia, A. Fete, and J.-M. Triscone, Influence of the growth conditions on the LaAlO<sub>3</sub>/SrTiO<sub>3</sub> interface electronic properties, *Europhys. Lett.* **91**, 17004 (2010).
- [61] M. Basletic, J.-L. Maurice, C. Carrétéro, G. Herranz, O. Copie, M. Bibes, É. Jacquet, K. Bouzouane, S. Fusil, and A. Barthélémy, Mapping the spatial distribution of charge carriers in LaAlO<sub>3</sub>/SrTiO<sub>3</sub> heterostructures, *Nature Mater.* **7**, 621 (2008).
- [62] O. Copie, V. Garcia, C. Bödefeld, C. Carrétéro, M. Bibes, G. Herranz, E. Jacquet, J.-L. Maurice, B. Vinter, S. Fusil, K. Bouzouane, H. Jaffrès, and A. Barthélémy, Towards two-dimensional metallic behavior at LaAlO<sub>3</sub>/SrTiO<sub>3</sub> interfaces, *Phys. Rev. Lett.* **102**, 216804 (2009).
- [63] N. Reyren, S. Gariglio, A. D. Caviglia, D. Jaccard, T. Schneider, and J.-M. Triscone, Anisotropy of the superconducting transport properties of the LaAlO<sub>3</sub>/SrTiO<sub>3</sub> interface, *Appl. Phys. Lett.* **94**, 112506 (2009).
- [64] I. Pallecchi, M. Codda, E. Galleani d'Agliano, D. Marré, A. D. Caviglia, N. Reyren, S. Gariglio, and J.-M. Triscone, Seebeck effect in the conducting LaAlO<sub>3</sub>/SrTiO<sub>3</sub> interface, *Phys. Rev. B* **81**, 085414 (2010).
- [65] A. Dubroka, M. Rössle, K. W. Kim, V. K. Malik, L. Schultz, S. Thiel, C. W. Schneider, J. Mannhart, G. Herranz, O. Copie, M. Bibes, A. Barthélémy, and C. Bernhard, Dynamical

- cal response and confinement of the electrons at the LaAlO<sub>3</sub>/SrTiO<sub>3</sub> interface, *Phys. Rev. Lett.* **104**, 156807 (2010).
- [66] C. Bell, S. Harashima, Y. Hikita, and H. Y. Hwang, Thickness dependence of the mobility at the LaAlO<sub>3</sub>/SrTiO<sub>3</sub> interface, *Appl. Phys. Lett.* **94**, 222111 (2009).
- [67] C. Cen, S. Thiel, G. Hammerl, C. W. Schneider, K. E. Andersen, C. S. Hellberg, J. Mannhart, and J. Levy, Nanoscale control of an interfacial metal-insulator transition at room temperature, *Nature Mater.* **7**, 298 (2008).
- [68] C. Cen, S. Thiel, J. Mannhart, and J. Levy, Oxide nanoelectronics on demand, *Science* **323**, 1026 (2009).
- [69] M. Ben Shalom, M. Sachs, D. Rakhmievitch, A. Palevski, and Y. Dagan, Tuning spin-orbit coupling and superconductivity at the SrTiO<sub>3</sub>/LaAlO<sub>3</sub> interface: A magnetotransport study, *Phys. Rev. Lett.* **104**, 126802 (2010).
- [70] A. D. Caviglia, M. Gabay, S. Gariglio, N. Reyren, C. Cancellieri, and J.-M. Triscone, Tunable Rashba spin-orbit interaction at oxide interfaces, *Phys. Rev. Lett.* **104**, 126803 (2010).
- [71] C. Bell, S. Harashima, Y. Kozuka, M. Kim, B. G. Kim, Y. Hikita, and H. Y. Hwang, Dominant mobility modulation by the electric field effect at the LaAlO<sub>3</sub>/SrTiO<sub>3</sub> interface, *Phys. Rev. Lett.* **103**, 226802 (2009).
- [72] D. B. Chrisey and G. K. Hubler, eds., *Pulsed Laser Deposition of Thin Films* (John Wiley & Sons, Inc., 1994).
- [73] P. R. Willmott and J. R. Huber, Pulsed laser vaporization and deposition, *Rev. Mod. Phys.* **72**, 315 (2000).
- [74] T. Ohnishi, H. Koinuma, and M. Lippmaa, Pulsed laser deposition of oxide thin films, *Appl. Surf. Sci.* **252**, 2466 (2006).
- [75] W. Braun, *Applied RHEED: Reflection High-Energy Electron Diffraction During Crystal Growth* (Springer, 1999).
- [76] G. Koster, Artificially layered oxides by pulsed laser deposition, Ph.D. thesis, University of Twente (1999), available online at: <http://doc.utwente.nl/23466/>.
- [77] P. J. Dobson, B. A. Joyce, J. H. Neave, and J. Zhang, Current understanding and applications of the RHEED intensity oscillation technique, *J. Cryst. Growth* **81**, 1 (1987).
- [78] B. E. Warren, *X-Ray Diffraction* (Dover Publications, Inc., 1990).
- [79] F. J. Giessibl, Advances in atomic force microscopy, *Rev. Mod. Phys.* **75**, 949 (2003).
- [80] D. G. Schlom, L.-Q. Chen, C.-B. Eom, K. M. Rabe, S. K. Streiffer, and J.-M. Triscone, Strain tuning of ferroelectric thin films, *Annu. Rev. Mater. Res.* **37**, 589 (2007).
- [81] T. Ohnishi, M. Lippmaa, T. Yamamoto, S. Meguro, and H. Koinuma, Improved stoichiometry and misfit control in perovskite thin film formation at a critical fluence by pulsed laser deposition, *Appl. Phys. Lett.* **87**, 241919 (2005).
- [82] T. Ohnishi, K. Shibuya, T. Yamamoto, and M. Lippmaa, Defects and transport in complex oxide thin films, *J. Appl. Phys.* **103**, 103703 (2008).
- [83] S. N. Ruddlesden and P. Popper, New compounds of the K<sub>2</sub>NiF<sub>4</sub> type, *Acta Crystallogr.* **10**, 538 (1957).
- [84] H. Yamada and G. R. Miller, Point defects in reduced strontium titanate, *J. Solid State Chem.* **6**, 169 (1973).

- [85] X. Luo and B. Wang, Structural and elastic properties of  $\text{LaAlO}_3$  from first-principles calculations, *J. Appl. Phys.* **104**, 073518 (2008).
- [86] S. F. Fang, K. Adomi, S. Iyer, H. Morkoç, H. Zabel, C. Choi, and N. Otsuka, Gallium arsenide and other compound semiconductors on silicon, *J. Appl. Phys.* **68**, R31 (1990).
- [87] Y. B. Bolkhovityanov and O. P. Pchelyakov, GaAs epitaxy on Si substrates: Modern status of research and engineering, *Phys. Usp.* **51**, 437 (2008).
- [88] K. Terai, M. Lippmaa, P. Ahmet, T. Chikyow, T. Fujii, H. Koinuma, and M. Kawasaki, In-plane lattice constant tuning of an oxide substrate with  $\text{Ba}_{1-x}\text{Sr}_x\text{TiO}_3$  and  $\text{BaTiO}_3$  buffer layers, *Appl. Phys. Lett.* **80**, 4437 (2002).
- [89] K. Terai, M. Lippmaa, P. Ahmet, T. Chikyow, H. Koinuma, M. Ohtani, and M. Kawasaki, Fabrication of lattice-tunable  $\text{Ba}_{1-x}\text{Sr}_x\text{TiO}_3$  buffers on a  $\text{SrTiO}_3$  substrate, *Appl. Surf. Sci.* **223**, 183 (2004).
- [90] B. H. Park, E. J. Peterson, Q. X. Jia, J. Lee, X. Zeng, W. Si, and X. X. Xi, Effects of very thin strain layers on dielectric properties of epitaxial  $\text{Ba}_{0.6}\text{Sr}_{0.4}\text{TiO}_3$  films, *Appl. Phys. Lett.* **78**, 533 (2001).
- [91] T. Yamada, K. F. Astafiev, V. O. Sherman, A. K. Tagantsev, P. Mural, and N. Setter, Strain relaxation of epitaxial  $\text{SrTiO}_3$  thin films on  $\text{LaAlO}_3$  by two-step growth technique, *Appl. Phys. Lett.* **86**, 142904 (2005).
- [92] C. M. Folkman, R. R. Das, C. B. Eom, Y. B. Chen, and X. Q. Pan, Single domain strain relaxed  $\text{PrScO}_3$  template on miscut substrates, *Appl. Phys. Lett.* **89**, 221904 (2006).
- [93] B. W. Lee, C. U. Jung, M. Kawasaki, and Y. Tokura, Tuning of magnetism in  $\text{SrRuO}_3$  thin films on  $\text{SrTiO}_3$  (001) substrate by control of the twin and strain amount in the buffer layer, *J. Appl. Phys.* **104**, 103909 (2008).
- [94] M. Kawasaki, K. Takahashi, T. Maeda, R. Tsuchiya, M. Shinohara, O. Ishiyama, T. Yonezawa, M. Yoshimoto, and H. Koinuma, Atomic control of the  $\text{SrTiO}_3$  crystal surface, *Science* **266**, 1540 (1994).
- [95] G. Koster, B. L. Kropman, G. J. H. M. Rijnders, D. H. A. Blank, and H. Rogalla, Quasi-ideal strontium titanate crystal surfaces through formation of strontium hydroxide, *Appl. Phys. Lett.* **73**, 2920 (1998).
- [96] J. Zhang, J. H. Neave, P. J. Dobson, and B. A. Joyce, Effects of diffraction conditions and processes on reed intensity oscillations during the MBE growth of GaAs, *Appl. Phys. A* **42**, 317 (1987).
- [97] Y. B. Chen, M. B. Katz, X. Q. Pan, C. M. Folkman, R. R. Das, and C. B. Eom, Microstructure and strain relaxation of epitaxial  $\text{PrScO}_3$  thin films grown on (001)  $\text{SrTiO}_3$  substrates, *Appl. Phys. Lett.* **91**, 031902 (2007).
- [98] J. M. Huijbregtse, B. Dam, J. H. Rector, and R. Griessen, High-quality off-stoichiometric  $\text{YBa}_2\text{Cu}_3\text{O}_{7-\delta}$  films produced by diffusion-assisted preferential laser ablation, *J. Appl. Phys.* **86**, 6528 (1999).
- [99] J. H. Song, T. Susaki, and H. Y. Hwang, Enhanced thermodynamic stability of epitaxial oxide thin films, *Adv. Mater.* **20**, 2528 (2008).
- [100] D. Kan, T. Terashima, R. Kanda, A. Masuno, K. Tanaka, S. Chu, H. Kan, A. Ishizumi, Y. Kanemitsu, Y. Shimakawa, and M. Takano, Blue-light emission at room temperature from  $\text{Ar}^+$ -irradiated  $\text{SrTiO}_3$ , *Nature Mater.* **4**, 816 (2005).

- [101] C. Aruta, S. Amoruso, R. Bruzzese, X. Wang, D. Maccariello, F. Miletto Granozio, and U. Scotti di Uccio, Pulsed laser deposition of SrTiO<sub>3</sub>/LaGaO<sub>3</sub> and SrTiO<sub>3</sub>/LaAlO<sub>3</sub>: Plasma plume effects, *Appl. Phys. Lett.* **97**, 252105 (2010).
- [102] S. Fähler and H.-U. Krebs, Calculations and experiments of material removal and kinetic energy during pulsed laser ablation of metals, *Appl. Surf. Sci.* **96**, 61 (1996).
- [103] A. D. Caviglia, Two-dimensional electron gas in functional oxide interfaces, Ph.D. thesis, Université de Genève (2010), available online at: <http://archive-ouverte.unige.ch/unige:12581>.
- [104] C. Merckling, M. El-Kazzi, G. Delhaye, V. Favre-Nicolin, Y. Robach, M. Gendry, G. Grenet, G. Saint-Girons, and G. Hollinger, Strain relaxation and critical thickness for epitaxial LaAlO<sub>3</sub> thin films grown on SrTiO<sub>3</sub>(0 0 1) substrates by molecular beam epitaxy, *J. Cryst. Growth* **306**, 47 (2007).
- [105] S. Thiel, C. W. Schneider, L. Fitting Kourkoutis, D. A. Muller, N. Reyren, A. D. Caviglia, S. Gariglio, J.-M. Triscone, and J. Mannhart, Electron scattering at dislocations in LaAlO<sub>3</sub>/SrTiO<sub>3</sub> interfaces, *Phys. Rev. Lett.* **102**, 046809 (2009).
- [106] M. Huijben, Interface engineering for oxide electronics: Tuning electronic properties by atomically controlled growth, Ph.D. thesis, University of Twente (2006), available online at: <http://doc.utwente.nl/55832/>.
- [107] S. Harashima, Control of the metallicity at the LaAlO<sub>3</sub>/SrTiO<sub>3</sub> interface, Bachelor's thesis, The University of Tokyo (2009).
- [108] T. Wakamura, Electric field control of the in-plane anisotropic transport properties at the LaAlO<sub>3</sub>/SrTiO<sub>3</sub> interface, Bachelor's thesis, The University of Tokyo (2010).
- [109] J. Mannhart and D. G. Schlom, Oxide interfaces—an opportunity for electronics, *Science* **327**, 1607 (2010).
- [110] C. W. Schneider, S. Thiel, G. Hammerl, C. Richter, and J. Mannhart, Microlithography of electron gases formed at interfaces in oxide heterostructures, *Appl. Phys. Lett.* **89**, 122101 (2006).
- [111] Y. W. Xie, C. Bell, T. Yajima, Y. Hikita, and H. Y. Hwang, Charge writing at the LaAlO<sub>3</sub>/SrTiO<sub>3</sub> surface, *Nano Lett.* **10**, 2588 (2010).
- [112] F. Bi, D. F. Bogorin, C. Cen, C. W. Bark, J.-W. Park, C.-B. Eom, and J. Levy, “Water-cycle” mechanism for writing and erasing nanostructures at the LaAlO<sub>3</sub>/SrTiO<sub>3</sub> interface, *Appl. Phys. Lett.* **97**, 173110 (2010).
- [113] H. Amano, N. Sawaki, I. Akasaki, and Y. Toyoda, Metalorganic vapor phase epitaxial growth of a high quality GaN film using an AlN buffer layer, *Appl. Phys. Lett.* **48**, 353 (1986).
- [114] A. D. Caviglia, S. Gariglio, C. Cancellieri, B. Sacépé, A. Fête, N. Reyren, M. Gabay, A. F. Morpurgo, and J.-M. Triscone, Two-dimensional quantum oscillations of the conductance at LaAlO<sub>3</sub>/SrTiO<sub>3</sub> interfaces, *Phys. Rev. Lett.* **105**, 236802 (2010).
- [115] H. Chou, S. G. Hsu, C. B. Lin, and C. B. Wu, Interdiffusion effect on strained La<sub>0.8</sub>Ba<sub>0.2</sub>MnO<sub>3</sub> thin films by off-axis sputtering on SrTiO<sub>3</sub> (100) substrates, *Appl. Phys. Lett.* **90**, 062501 (2007).
- [116] S. Thiel, Study of interface properties in LaAlO<sub>3</sub>/SrTiO<sub>3</sub> heterostructures, Ph.D. thesis, University of Augsburg (2009).

- [117] M. J. Kane, N. Apsley, D. A. Anderson, L. L. Taylor, and T. Kerr, Parallel conduction in GaAs/Al<sub>x</sub>Ga<sub>1-x</sub>As modulation doped heterojunctions, *J. Phys. C: Solid State Phys.* **18**, 5629 (1985).
- [118] H. Miyazawa and H. Ikoma, Non-Ohmic properties in *n*-type InSb, *J. Phys. Soc. Jpn.* **23**, 290 (1967).
- [119] K. Szot and W. Speier, Surfaces of reduced and oxidized SrTiO<sub>3</sub> from atomic force microscopy, *Phys. Rev. B* **60**, 5909 (1999).

# Acknowledgments

First of all, I would like to express my heartfelt thanks to Prof. Harold Y. Hwang, for his continuous support and education. Without his advice, suggestions, patience and courtesy, it would definitely be impossible to write this Thesis. His firm belief, both as a researcher and as an educator, has been motivating and encouraging me. I learned from him what a scientist is, how a scientist should be.

I would also like to add sincere thanks to every member of Hwang laboratory: Dr. Yasuyuki Hikita, Dr. Christopher Bell, Dr. Yanwu Xie, Dr. Makoto Minohara, Mr. Takeaki Yajima, Mr. Minu Kim, Mr. Masayuki Hosoda, Mr. Yasuo Nakanishi, Mr. Satoshi Harashima, Mr. Hisashi Inoue, Mr. Takashi Tachikawa. I cannot neglect the former members I worked with: Dr. Yusuke Kozuka, Mr. Takuya Higuchi, Mr. Yuichi Ota, Mr. Motohide Kawamura, Mr. Kotaro Takeyasu, Mr. Takeaki Hidaka, Mr. Moyuru Kurita, Mr. Taro Wakamura. Through daily discussions, I learned from them a lot of things; background knowledge, experimental methods, presentation skills, for example. My enjoyable life in the laboratory is also greatly supported by them. Particularly, let me add special appreciations to Dr. Hikita and Dr. Bell for their critical readings and discussions. The quality of this Thesis was markedly improved by them.

I would equally like to emphasize that my work has been indirectly, but greatly supported by our secretary, Ms. Makiko Tanaka. Without her office work, as well as her cheerful words and smile, I would not be able to pursue my research.

I am also grateful to the visiting members: Prof. Bog G. Kim, Dr. Daeyoung Kwon, Mr. Bongju Kim, and Mr. Youngsoo Wu (Pusan National University, Korea), Prof. Arthur F. Hebard and Dr. Guneeta Singh-Bhalla (University of Florida, USA), Dr. James M. Rondinelli (University of California, Santa Barbara, USA), Mr. Hans Boschker (University of Twente, the Netherlands), Mr. Mitchell Rutkowski (The Ohio State University, USA). I really enjoyed having a close relationship with such talented and sincere people.

Let me also express my appreciations to my collaborators outside the laboratory. I thank Prof. Scott A. Chambers and his colleagues (Pacific Northwest National Laboratory, USA) for characterizing some of my samples by several spectroscopy techniques, particularly for their detailed study by x-ray photoelectron spectroscopy. While the results are not presented in this Thesis, their extensive researches and discussions significantly deepened my understanding. I am also thankful to Prof. David A. Muller and Ms. Julia A. Mundy (Cornell University, USA) for their STEM measurements presented in Chap. 4 and helpful discussions. I appreciate the kindness of Prof. Hidenori Takagi (The University of Tokyo) for letting me use their equipment, with which the SrAlO<sub>x</sub> target in Chap. 4 was fabricated and analyzed. I am grateful to Prof. Mikk Lippmaa and the members of his laboratory (The University of Tokyo) for the permission and the assistance to use their clean room facilities and ion milling machine, with which the star-

patterned sample in Chap. 5 was fabricated. I also thank Ms. Mayumi Misaki at Hitachi Kyowa Engineering Co., Ltd. for the ICP measurements presented in Chap. 5 and related discussions. Last of all, I give my thanks to my family for their endless support.

From the bottom of my heart,

January 2011

A handwritten signature in black ink, consisting of the Japanese characters '佐藤 弘樹' (Sato Hiroki) written in a cursive style.

Hiroki SATO



2010 Master's thesis: Growth Control of the Electronic Properties of the  $\text{LaAlO}_3/\text{SrTiO}_3$  Heterointerface  
平成二十二年/修士論文：  $\text{LaAlO}_3/\text{SrTiO}_3$  へテロ界面の電子物性の作製条件による制御

Hiroki SATO  
佐藤 弘樹